STUDY OF CHAOTIC FLOWS IN NON-NEWTONIAN FLUIDS AT LOW REYNOLDS NUMBERS

A Dissertation

by

KRISHNA TEJASVI KHAMBHAMPATI

Submitted to the Office of Graduate and Professional Studies of
Texas A&M University
in partial fulfillment of the requirements for the degree of

DOCTOR OF PHILOSOPHY

Chair of Committee,	Kumbakonam Rajagopal
Committee Members,	Alan Freed
	Shivakumar Rathinam
	Jay R. Walton
Head of Department,	Andreas Polycarpou

May 2020

Major Subject: Mechanical Engineering

ABSTRACT

With the advent of technologies related to the miniaturization of devices, the ability to predict the fluid motion in and around these devices assumes importance for their design and optimization. Because of the small dimensions and very low speeds that are involved, the flows within these components are generally laminar. Such laminar flows are a consequence of the limitations imposed by viscous stresses and the devices associated with them are important for a range of applications in areas such as pharmaceutics, medicine, heat transfer, biomedical engineering, and electronics cooling. In every case, the devices associated with these application areas would generally benefit by augmented transport of a scalar and/or heat to facilitate the processes which are underway.

Polymer additives, such as polyacrylamide, have unique characteristics in liquids, including highly non-linear, viscoelastic behavior. The extensibility of the polymer and the resulting polymer deformation leads to a sharp growth in the local elastic stress. This gives rise to an instability that develops into turbulence in a sequence of events referred to as the elastic turbulence. Such changes also increase the mixing of scalars and enhance heat transfer in the fluid flow.

The afore-mentioned chaotic flow at vanishingly low Reynolds number called elastic turbulence is a strongly fluctuating regime of fluid flow. This phenomenon, observed in viscoelastic polymer solutions is driven by the strong coupling between the fluid velocity and its elasticity. Current research is an attempt to numerically capture the phenomenon by developing a generalized 3D module to solve hyperbolic viscoelastic partial differential equations in ANSYS-FLUENT and thereby provide some insight into the phenomenon.

ACKNOWLEDGEMENTS

I would like to thank my committee chair, Dr. Rajagopal, for being an inspiration, and Dr. Robert Handler for infusing me with enthusiasm to pursue my research at regular intervals.

Special thanks to Prof. Michael Golla of the Department of Engineering Technology and Industrial Distribution for entrusting me with a recurring teaching assistant position and providing me with much needed financial stability to pursue my research.

I especially need to thank all of my lab mates, Bhaskar, Manoj, Pavitra, Alagappan, Choi, & Juan, for making the workplace a lot of fun. I also recognize the role played by several brainstorm sessions with Manoj and Bhaskar in forwarding my research. I am pleased to acknowledge my roommates, Srikanth and Vamsi, and to all my friends over the years, which made my experience in College Station a very memorable one. I acknowledge my mentors Jay Pandiyan and Vineet Rakesh of WL Gore for helping me find a path to transition from academia to the industry.

I am indebted to my parents, my sister, my aunt (Dr. Seshu Latha), and my uncle (Dr. Vishwanatha Sharma) for believing in me when the going was steep and also for providing me with financial support at the beginning of my Ph.D. I must mention the role of the inspiration that I draw from my grandparents Ms. K. Sarada, Ms. K. Sundari, and Dr. K. Krishna Murthy. I also thank my cousin Madhavi Singaraju (& family) for being my ever-dependable guardian in the USA.

I would finally like to thank my wife, Akshaya Ravichandran, for being a positive influence in more ways than one.

CONTRIBUTORS AND FUNDING SOURCES

Contributors

This work was supported by a dissertation committee consisting of Dr. Kumbakonam Rajagopal, Dr. Alan Freed and Dr. Shivakumar Rathinam of the Department of Mechanical Engineering and Dr. Jay Walton of the Department of Mathematics. The analyses depicted in Chapter 6 were conducted in part by Bhaskar Vajipeyajula of the Department of Mechanical Engineering and Dr. Robert Handler from George Mason University and were published in (2017) in an article listed in the journal named Physics of Fluids [48]. All other work conducted for the dissertation was completed by the student independently.

Funding sources

Graduate study was supported through Teaching Assistanship provided by Professor Michael Golla of the Department of Engineering Technology and Industrial Distribution.

TABLE OF CONTENTS

Page

LIST OF FIGURES

FIGURE Page

LIST OF TABLES

TABLE Page

1. INTRODUCTION

In recent years, much attention has been devoted to technological advances related to miniaturization, with particular attention to technologies at milli-scales and micro-scales. For example, improvements in manufacturing technology and microfabrication have led to the miniaturization of devices and sensors such as heat exchangers, micro-sensors, micro-pumps, biological reactors, selective membranes, and other devices. The ability to predict the fluid motion in and around these devices is essential for their design and optimization. As the length scales of these devices decrease for the liquid flow, effects such as near-wall slip flow, altered surface roughness effects, non-Newtonian fluid behavior, and variations of fluid properties become significant. Because of the small dimensions and very low speeds that are involved, the flows within these components are generally laminar. Corresponding Reynolds numbers are very low, even significantly less than 1, along with the concomitant thermal transport.

Such small length scale flows are dominated by viscous stresses, and this impedes molecular transport and consequently, mixing in the fluid. Such flows are ubiquitous in a wide range of applications in areas such as pharmaceutics, medicine, heat transfer, biomedical engineering, and electronics cooling. In every case, the devices associated with these application areas would generally benefit by augmented transport of a scalar and/or heat to facilitate the processes which are underway. In many cases, enhanced mixing of items advected within different fluid components or streams is required. Such mixing is important for a variety of situations within the mentioned application areas, including the use of liquids to cool electronic components, mixing of different chemical components to manufacture pharmaceuticals, lab-on-a-chip

devices which involve the interaction and mixing of different fluid streams, and of course, miniature heat exchangers for use in devices ranging from automobiles to appliances, to components within space systems, including satellites.

Non-Newtonian fluids like polymer solutions and colloidal suspensions are prevalent in a wide range of engineering and industrial applications. Typical examples include applications in the chemical industry, food industry, and biomedical industry, to name a few. In a broad sense, non-Newtonian behavior can be characterized by the non-linear relation between the stress endured by a macroscopic fluid element and the shear rate. The atypical characteristics of viscoelastic fluids give rise to phenomena that can significantly affect the dynamics of momentum, heat transport, and mixing of other scalars. Comprehending these phenomena could offer new avenues in thermal and scalar transport.

1.1 Present investigation and overall objectives

The use of polymer additives, such as polyacrylamide, to enhance mixing, is the prime motivation of the present study. This is because of the unique characteristics of polymers in liquids, which are generally associated with highly non-linear, non-Newtonian behavior. With λ as the characteristic relaxation time of the polymer flow, the Weissenberg number is given by $\frac{\lambda V}{L}$, where V and L are characteristic velocity and length scale, respectively. It is important to note that such polymer flows are also characterized by other multiple time scales, including ones related to the elastic deformation, in addition to λ. When the polymers are stretched by the strain induced by the velocity gradients in the flow, the extensibility of the polymer and resulting polymer deformation leads to a sharp growth in the local elastic stress. This causes a chain of events referred to as the Weissenberg instability, which occurs when the Weissenberg number is greater than a critical value. The focus of the

present study is to capture such changes numerically.

Past investigations have reported turbulence that results from elastic polymer distortion using flow fluctuation measurements, measurements of Reynolds stress tensor components, and measurements of spectra of unsteady velocity motions. The fluid dynamical phenomenon is sometimes referred to as elastic turbulence. This was initially discovered by Groisman and Steinberg [21].

Their initial experiments were performed in a swirling flow, also known as the Von Karman swirling flow, in which a rotating disk imparts shear to a fluid composed of a high molecular weight polymer (polyacrylamide with a molecular weight of 18×10^6) dissolved in a water-sugar solvent to form a dilute (80ppm) polymer solution. They found that when the strain rate imparted to the fluid exceeded a certain limit, the torque needed to maintain a given rotation rate increased to nearly 20 times that of laminar Newtonian flow with the same shear rate. In a more familiar Newtonian, turbulent pipe flow, a similar increase in drag, would require a Reynolds number of 10^5. The increase in torque was found to be accompanied by a chaotic velocity field, even though the Reynolds number $\frac{VL}{\nu}$, where V and L are characteristic velocities and dimensions of the flow and ν is the kinematic viscosity of the solution, remained less than one. A chaotic flow was observed at Reynolds numbers as low as 10^{-3}.

It was found that the Weissenberg number, defined as the ratio of the polymer relaxation time, λ, to a characteristic flow time scale, L/V, or as the product of the relaxation time to a characteristic flow strain rate, $\dot{\gamma}$, $Wi = \frac{\lambda V}{L} = \lambda\dot{\gamma}$, was the key non-dimensional number in determining the nature of the flow. Chaotic fluid motions were observed only when Wi exceeded one, and in these particular experiments, chaos was first observed for $Wi = 3.5$. Fluid dynamical instabilities in non-Newtonian fluids exhibiting elasticity have been reported earlier [30] [43], but not the development of chaotic flows.

The initial discovery of elastic turbulence [21] was followed by a number of other experimental investigations in which elastic turbulence was found not only in swirling flow [11] [12], but also in Taylor-Coutte flow [23] and Dean flow [22] [23] [10] [28]. Most commonly reported properties of elastic turbulence are as follows:

- It has been found experimentally only in flows with curved streamlines, although some recent numerical studies [4] [3] have hinted that elastic turbulence may appear in flows with rectilinear mean streamlines.
- A wide range of length scales are excited. The flows appear spatially smooth but temporally chaotic.
- Significant increases in mass and momentum transport are observed, comparable to those found in inertial turbulence.

Note that the term 'inertial turbulence' is used here to refer to the turbulent flows in Newtonian fluids such as in pipe, channel, and boundary layer flows at higher Reynolds number [45], where the sources of nonlinearity are inertial forces, as distinguished from elastic turbulence, where the dominant source of nonlinearity is derived from elastic stresses.

In all these elastic turbulent flows, the energy spectrum of the velocity fluctuations behaves typically as $E(k) \approx k^{-n}$, where E is the spectral energy density of the velocity fluctuations, k is the wavenumber, and n is typically found to be about 3.5. This very steep drop off in the energy spectrum, when compared to the much smaller $n = 5/3$ found in classical inertial turbulence, leads one to think of a possible close analogy between elastic turbulence and inertial turbulence. Despite some differences between elastic turbulence and standard high-Reynolds-number-inertial turbulence, elastic turbulence gives rise to significant increases in transport well above the laminar state and for this reason remains intriguing as a possible means of increasing

the flux of mass, momentum, and heat in flow devices that are not large enough to develop ordinary inertial turbulence.

With that note in mind, the overall objectives of the present investigation are as follows:

- Develop numerical and analytic models to describe and represent the related physical phenomena. These goals represent only a first step in understanding this complex phenomenon.

- Develop a reliable viscoelastic solver for the purpose of capturing the physical phenomena numerically.

- Enhance the fundamental understanding of the effects of polymers in liquids and the physical processes associated with elastic turbulence.

The success in achieving these objectives may lead not only to a fundamental physical understanding of the processes involved but also to the development of a means to control elastic turbulence in liquids.

1.2 Mechanism of elastic turbulence

The chaotic state referred to as elastic turbulence arises at nearly vanishing Re but for Wi greater than a critical value, and it is therefore tempting to compare the properties and mechanism of formation of elastic turbulence with those of the more familiar inertial turbulence, which occurs in Newtonian flows ($Wi = 0$) at high Re. Superficially, elastic turbulence appears to have some similar characteristics with inertial turbulence, such as (1) a full Fourier-wave number spectra for the velocity field, indicating the existence of a broad range of spatial scales, (2) chaotic in both space and time, and (3) large increases in mass, and momentum transport. Despite

these similarities, there are fundamental differences involved in the basic physical processes leading to both the forms of turbulence.

In Newtonian fluids, the occurrence of turbulence is attributed to the dominance of inertial forces over viscous forces, where inertial forces are represented by the non-linear advective term in the momentum equation given by $u_i \partial_i u_j$, where u_i is the fluid velocity. This is embodied in the requirement that the Reynolds number be large. On the other hand, elastic turbulence occurs at low Reynolds numbers, indicating that inertial nonlinearities are entirely negligible. Instead, elastic turbulence is due to the growth and dominance of elastic stresses over viscous dissipation. Moreover, elastic stresses are nonlinearly dependent on the rate of deformation of the flow as represented in standard constitutive models (e.g., FENE-P, Oldroyd, Geiskus, etc.) for dilute polymer solutions. As a result of the inertial nonlinearity in standard Newtonian turbulence, increases in flow resistance are due to the existence of the so-called Reynolds stresses $\tau_{ij} = \rho u'_i u'_j$ where ρ is the density and u'_i are the fluctuating components of fluid velocity. In elastic turbulence, however, these Reynolds stresses are typically orders of magnitude lower than elastic stresses, τ^p_{ij}, which is a function of the conformation tensor, represented by $< r_i r_j >$, where r_i is the component of the end-to-end vector associated with a given polymer molecule, and averaged over all possible molecular configurations. This significant increase in the elastic stress, which may lead to elastic turbulence, is responsible for the increased transport in these flows. In effect, the high Reynolds stresses associated with inertial turbulence are replaced in elastic turbulence by polymer stresses. Elastic turbulence should then lead not only to increased momentum transport but also to increases in heat and mass transport.

Polymer additive effects are important, both from microscopic and macroscopic perspectives. The subsequent abrupt increase in non-linear elastic polymer stresses

is attributed to the instability caused by the elongation of the polymer molecules. These then give rise to local fluid distortion, local increases in mixing, and the development of secondary and oscillatory vortex flows, all of which lead to increased transport at extremely low Reynolds number. According to Groisman and Steinberg [23], such fluctuations are excited over broad ranges of frequency and wavenumbers, as indicated by the experimentally determined spectra of the velocity fluctuations in these flows. The transport then generally exhibits characteristics of traditional inertial turbulence, including three-dimensionality, vertical motions, unsteadiness, random mixing, and organized flow structures [30] [43]. The changes induced by the polymers thus have an essential relationship to transport and turbulence, especially to increased transport of passive scalars, and increased transport of thermal energy. The shear rate and viscosity changes which result from the polymer distortion are expected to lead also to important changes to the effective eddy diffusivity for heat and momentum. The primary motivation of the research is to be able to capture such changes.

As mentioned, a key component in characterizing the development of elastic turbulence is the Weissenberg number Wi given by $\frac{\lambda V}{L}$, where $\frac{V}{L}$ can be thought of as the characteristic rate of deformation. When the Weissenberg number is greater than a critical value, an instability appears and involves a sharp growth in local elastic stress as a result of the extensibility of the polymers and the resulting polymer deformation. This occurs as the relaxation time scale becomes of the order of the rate of deformation. The sharp growth in elastic stress is accompanied by emergence of velocity fluctuations in the flow. Overall consequences include increased polymer viscosity, increases in polymer thermal diffusivity, and augmentation of thermal transport. Here, the characteristic relaxation time λ is related to the flow history, and is determined as the time interval over which fluid stress decays, starting at the

point when fluid motion stops. This means that the stress does not become zero at the moment the fluid stops moving [21], and the relationship between the stress τ^p and the local rate of flow deformation is nonlinear, with significant hysteresis. Longer characteristic relaxation times generally mean larger stresses that linger on over longer time intervals.

To summarize, the scenario by which elastic turbulence is generated [11] [12] [23] [23] [10] and [28], is complex and needs to be considered from both microscopic and macroscopic viewpoints. From a microscopic perspective, in the absence of flow gradients, polymer molecules in solution are thought to be coiled in spheres with radii much smaller than the total length of the molecule. In the presence of velocity gradients, the polymer shapes become more ellipsoidal but are not elongated enough to have a great macroscopic effect on the flow. However, when a match occurs between the time scales of the strain field and the polymer realization time, the polymers can be stretched to nearly their maximal length. This abrupt change in polymer conformation is referred to as the coil-transition [32] [14], and can be thought of as the transition point between Newtonian and non-Newtonian behavior. The coil-stretch transition has important macroscopic effects on the flow, such as inducing a dramatic growth in elastic stresses that in turn start affecting the flow, causing flow instabilities, usually termed as the Weissenberg effect [30] [43]. At sufficiently high Wi, the growth rate of the elastic energy exceeds that of viscous dissipation, leading to the evolution of a chaotic state called elastic turbulence. This state becomes saturated or quasi-statistically stationary when elastic forces come into balance with viscous forces.

1.3 Other properties

Once elastic turbulence appears, the heat transfer rate is expected to increase, with a corresponding many-fold increase in the effective thermal diffusivity. This should be expected since, with the appearance of elastic turbulence, momentum transport is strongly enhanced, as mixing between fluid layers with differing temperatures and velocities increases. Similarly, elastic instabilities arising due to the Weissenberg instability should increase mixing between fluid layers of differing temperatures, thereby increasing thermal transport.

Up to now, elastic turbulence has been observed only in geometries with curved, rather than rectilinear, mean streamlines. To achieve elastic turbulence in flows such as ordinary channel flow, very high elastic nonlinearities may be required.

1.4 Modeling of non-Newtonian fluids

This section is dedicated to the introduction of models that are used for the numerical simulation of the flow of dilute viscoelastic fluids. The idea is to focus on the differential formulation of these equations, as this is well suited for solving flow problems with inlets and outlets in a Eulerian description. Though integral versions of such equations also exist, these are better suited for a Lagrangian description and transient problems with free interfaces. Maxwell is credited with some of the earliest work in developing a differential constitutive model for a viscoelastic fluid. He combined the properties of a Newtonian fluid with those of elastic solids in a simple way. It is also sometimes referred to as the Maxwell "spring - dashpot" model. These mechanical analogs use a "Hookean" spring and a linear dashpot connected in series and are used to model the viscoelasticity of the fluid. The entropic uncoiling process is fluid like in nature and can be modeled by a linear dashpot in which the stress produces a strain rate. The following are the equations of a Hookean spring and

linear dashpot, respectively.

$$\boldsymbol{\sigma} = E\boldsymbol{\epsilon}, \tag{1.1}$$

$$\boldsymbol{\sigma} = \mu\dot{\boldsymbol{\epsilon}}. \tag{1.2}$$

where $\boldsymbol{\sigma}$ and $\boldsymbol{\epsilon}$ and $\dot{\boldsymbol{\epsilon}}$ denote stress, strain and strain rate respectively.

In summary, the "Maxwell" solid is a mechanical model in which a Hookean spring and a linear dashpot are connected in series. The spring can be visualized as representing the elastic or energetic component of the response, while the dashpot represents the dissipative component due to viscosity. In a series connection such as the Maxwell model, the stress on each element is the same and equal to the imposed stress, while the total strain is the sum of the strain in each element. $\boldsymbol{\sigma} = \boldsymbol{\sigma}_s = \boldsymbol{\sigma}_d$ and $\boldsymbol{\epsilon} = \boldsymbol{\epsilon}_s + \boldsymbol{\epsilon}_d$. The subscripts s and d represent the spring and dashpot, respectively. In order to arrive at a single equation relation of the stress to the strain, the strain equation can be differentiated, and the spring and dashpot strain rates can be rewritten in terms of the stress as follows:

$$\frac{\partial \boldsymbol{\epsilon}}{\partial t} = \frac{\partial \boldsymbol{\epsilon}_s}{\partial t} + \frac{\partial \boldsymbol{\epsilon}_s}{\partial t} = \frac{1}{E}\frac{\partial \boldsymbol{\sigma}}{\partial t} + \frac{\boldsymbol{\sigma}}{\mu}. \tag{1.3}$$

It is convenient to introduce the ratio of viscosity to elastic modulus as $\lambda = \frac{\mu}{E}$. The unit of λ is time and it is useful in measuring the time of the material's viscoelastic response. It is often referred to as the time constant. Multiplying equation (1.3) by E and using the definition of λ we have,

$$E\frac{\partial \boldsymbol{\epsilon}}{\partial t} = \frac{\partial \boldsymbol{\sigma}}{\partial t} + \frac{\boldsymbol{\sigma}}{\lambda}. \tag{1.4}$$

This Maxwell model can be generalized to arbitrary deformations by taking its ten-

sor equivalent, however, the Eulerian time derivative equation (1.4) is not frame-invariant. The solution is to adopt a special frame-invariant time derivative denoted by $\overset{\nabla}{\boldsymbol{\tau}}$ and give by equation (1.5). From this point on, $\boldsymbol{\tau}$ and $\dot{\boldsymbol{\gamma}}$ are used as the stress tensor and shear rate tensor, respectively.

$$\overset{\nabla}{\boldsymbol{\tau}} = \frac{D\boldsymbol{\tau}}{Dt} - \boldsymbol{\tau}\boldsymbol{L} - \boldsymbol{L}^T\boldsymbol{\tau}, \tag{1.5}$$

$$\frac{\boldsymbol{\tau}}{\lambda} + \overset{\nabla}{\boldsymbol{\tau}} = \mu_p\dot{\boldsymbol{\gamma}}. \tag{1.6}$$

When excluding a solvent contribution ($\mu_s = 0$), one can arrive at the Upper Convected Maxwell Model (UCM), while the Oldroyd-B model can be obtained otherwise. $\boldsymbol{L}$ is the velocity gradient of the flow. Oldroyd [37] named his models: Oldroyd - A and Oldroyd - B. He solved the problem of invariance with respect to the rotation of the coordinate system by inventing the upper and lower convected derivatives. The Oldroyd -A model is largely unused today, because agreement with experiment tends to be superior for the Oldroyd-B model. In contrast to the generalized Newtonian models, both the Oldroyd - B and UCM model have a constant shear viscosity and give rise to large normal stresses.

The derivation of the Maxwell and Oldroyd - B models takes a phenomenological approach with the upper convected derivative introduced as a fix, but it is also possible to start by considering the micro-structure of a viscoelastic fluid and arrive at the same result. The idea is the that two point masses connected with a spring can describe the elastic components in what is called a dumbbell model. The conformation tensor is the statistical average of the dyadic product between the end-to-end vector $\boldsymbol{r}$ and itself normalized with the maximum extension l_0 of the polymer molecules

(Refer to Fig. 1.1).

$$\boldsymbol{C} = \langle \frac{\boldsymbol{r} \otimes \boldsymbol{r}}{l_0^2} \rangle. \tag{1.7}$$

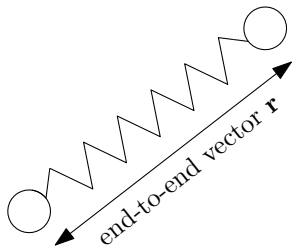

Fig. 1.1: Two point masses connected with a spring denoting the end-to-end vector of the dumbbell

For this approach, it becomes substantially easier to write and understand, when expressed in terms of the conformation tensor, in particular the FENE-P (Finitely Extensible Non-Linearly Elastic - Peterlin) model discussed in the following. Another point is that it makes the model compatible with the log-conformation formulation that will be detailed later. Finally, the derivation of the constitutive equations from the starting point relates the relaxation and polymer viscosity to properties of the micro-structure, namely

$$\lambda = \frac{\zeta}{4H} \quad \text{and} \quad \mu_p = \frac{n\kappa_B T\zeta}{4H}. \tag{1.8}$$

where ζ is a friction coefficient between the fluid and the dumbbells, H is the spring constant, n is the dumbbell concentration, T is the temperature and κ_B is the Boltzmann constant. Bird et al. [8] showed that the Oldroyd-B model can rewritten as

the following equations, if one assumes a Hookean spring force for the dumbbell.

$$\frac{D\boldsymbol{C}}{Dt} = \underbrace{\left(\frac{\partial \boldsymbol{u}}{\partial \boldsymbol{x}}\right)^T \boldsymbol{C} + \boldsymbol{C}\left(\frac{\partial \boldsymbol{u}}{\partial \boldsymbol{x}}\right)}_{stretching/orientation} - \underbrace{\frac{1}{\lambda}[\boldsymbol{C} - \boldsymbol{I}]}_{relaxation} \tag{1.9}$$

$$\boldsymbol{\tau}^p = \frac{\mu_p}{\lambda}[\boldsymbol{C} - \boldsymbol{I}] \tag{1.10}$$

The Hookean spring force of the Oldroyd-B and UCM models can give rise to exponential growth in time for the conformation tensor in the case of an extensional flow. This is unphysical, because the ratio of extension to equilibrium length quickly exceeds that of the elastic micro component. This behavior can also prevent convergence of numerical algorithms. The remedy is to introduce a varying spring constant, such that the relaxation term balances the stretching term, when the dumbbells become very extended. The evolution equation for the conformation tensor for the FENE-P model is as follows,

$$\frac{D\boldsymbol{C}}{Dt} = \left(\frac{\partial \boldsymbol{u}}{\partial \boldsymbol{x}}\right)^T \boldsymbol{C} + \boldsymbol{C}\left(\frac{\partial \boldsymbol{u}}{\partial \boldsymbol{x}}\right) - \frac{1}{\lambda}[f(R)\boldsymbol{C} - \boldsymbol{I}]. \tag{1.11}$$

Also the polymeric stress $\boldsymbol{\tau}^P$ is given by the following equation:

$$\boldsymbol{\tau}^p = \frac{\mu_p}{\lambda}[f(R)\boldsymbol{C} - \boldsymbol{I}] \tag{1.12}$$

$f(R)$, called the Peterlin function, is introduced to take into account the non-linear spring-like behavior of the polymer molecules. $f(R) = \frac{L_0^2 - 3}{L_0^2 - R^2}$, where R^2 is the trace of $\boldsymbol{C}$.

1.5 Dissertation overview

This dissertation, broadly speaking, targets to explore and understand the complex phenomenon of elastic turbulence numerically. To this cause, the dissertation is divided into five main parts, each presented as a chapter.

Chapter 2 focuses on developing the FENE-P model within a thermodynamic framework and establishing an analogy between the conformation tensor, which is a microscopic definition, and the left Cauchy-Green elastic stretch, which is a macroscopic definition.

Chapter 3 shows the work of code verification against exact solutions for the fully developed viscoelastic problem that has been derived by Cruz et al. [13]. This exact solution allowed us to directly compare the code for validity. For the sake of clarity, a detailed description of the analytical solution of the FENE-P model in a pipe has been developed. Also, the details of how the FENE-P model and its constitutive equations are incorporated into ANSYS-FLUENT via UDF interface, have been provided.

Chapter 4 discusses the infamous High Weissenberg number Numerical Problem (HWNP) and how it inhibits the ability to numerically simulate viscoelastic flows beyond a low to moderate value of Weissenberg number. This chapter delineates the log-conformation reformulation introduced by Fattal and Kupferman [17] [18] as a remedy to the HWNP and its implementation in ANSYS-FLUENT.

Chapter 5 details the original experiment performed by Groisman and Steinberg [21] and then proceeds to recreate the experiment on ANSYS-FLUENT numerically and presents the comparison of the results with the original experiment. This numerical experiment involves swirling flow simulation in a confined cylinder of a viscoelastic solution modeled using the FENE-P model. The torque required to ro-

tate the viscoelastic fluid for varying shear rates has been calculated and compared against an equivalent Newtonian case.

Chapter 6 presents an alternate technique to tackle the problem of the flow of viscoelastic fluids at low Reynolds numbers, namely, the 'pseudo-spectral' method. Dynamics of a single buoyant plume in a FENE-P fluid have been investigated by performing a series of direct numerical simulations using the 'pseudo-spectral' method.

2. THE DERIVATION OF THE FENE-P MODEL WITHIN A CONTEXT OF A THERMODYNAMIC PERSPECTIVE

2.1 Introduction

Ever since the seminal work of Maxwell [34] for describing the viscoelastic response of air, there have been a plethora of models that have been proposed to describe the response of a variety of viscoelastic fluids spanning the gamut from materials such as asphalt, numerous polymeric liquids, and biological fluids. Contrary to popular belief, Maxwell [34] did not develop his model by appealing to analogs based on springs and dashpots; rather, he based his work on the viscoelastic body possessing a means for storing energy and a means for dissipating energy. Using these two ideas, Maxwell developed a rate type viscoelastic model. Maxwell's model was meant to describe the one-dimensional response of viscoelastic fluids, and hence, questions such as whether the model satisfied invariance requirements such as frame-indifference were not germane. It was Oldroyd [37], using a phenomenological approach, who developed a systematic framework for generating models that were properly frame-indifferent and could be used to describe the three-dimensional response of rate type viscoelastic fluids. Oldroyd [37], however, did not concern himself with questions concerning the restrictions imposed by thermodynamics on the development of such fluid models.

Another stream of studies arrives at models for viscoelastic fluids based on appealing to ideas that stem from the kinetic theory of gases, interestingly once again an area that was initiated by Maxwell [34]. Warner Jr [50], appealing to spring-dashpot-dumbbell analogs developed by Bird and Warner Jr [6], introduced a model that is referred to as the FENE model. The FENE-P model uses the work of Peterlin

[7] to provide closure to the FENE model and is a popular model in Non-Newtonian fluid mechanics. Much has been written concerning the restrictions placed by thermodynamics on these models. In this chapter, the approach used by Rajagopal and Srinivasa [40] shall be adopted. This approach leads to models that bear a striking similarity to the FENE-P model and show that these models can be obtained from a totally different perspective, which is closer in spirit to the original work of Maxwell in terms of the choices made for the energy storage and energy dissipation mechanisms. Proper identifications are also made between the conformation tensor and the Cauchy-Green tensor from the evolving natural configuration.

The main idea behind the development of models by Rajagopal and Srinivasa [40] is based on appealing to the following two notions, the first that as a body is subject to a thermodynamic process, the bodies underlying natural configuration evolves (a notion first propounded by Eckart [16]; see also Rajagopal [38] for a detailed discussion of the notion of natural configuration), and second the manner in which the natural configuration evolves is such that the entropy production is maximized. The response of a viscoelastic body can then be viewed as a one-parameter family of response from an evolving natural configuration (see Fig. 2.1). Associating different energy storage and energy dissipation mechanisms (by picking appropriate Helmholtz potentials and rate of dissipation functions), one can derive different viscoelastic fluid models and Rajagopal and Srinivasa [40] showed how models due to Maxwell, Oldroyd, and Burgers as well as their generalizations could be derived using such an approach. This approach, however, does not deliver the models that are a consequence of adopting a kinetic theory approach, such as the FENE-P model that is popular amongst some rheologists. Later Rajagopal and Srinivasa [39] showed how models such as the FENE-P and other models that stem from the kinetic theory approach could be generated by choosing an appropriate Gibbs potential that depends

on the stress and a rate of the entropy production function.

An advantage of the approach adopted by Rajagopal and Srinivasa in [40] and [39] is that one can enforce the requirement of incompressibility in the normal fashion, one cannot do the same within the context of the approach that appeals to the conformation tensor. As most viscoelastic fluids are incompressible, Rajagopal and Srinivasa [40] required that the viscoelastic fluid be constrained to undergo only isochoric motion, and thus both the elastic response from the natural configuration as well as the evolution of the natural configuration be isochoric. Málek et al. [33] used a different constraint in order to obtain the models, while they required that the total response of the fluid be isochoric, namely $\det \boldsymbol{F}_{\kappa_R} = 0$ (see Fig 2.1), they did not enforce the constraint on the individual responses; namely, the elastic response, and the dissipative response. In order to obtain models, such as Maxwell and Oldroyd, in the approach used by Rajagopal and Srinivasa [40], the energy storage mechanism has to be assumed as neo-Hookean. The resulting nonlinear constitutive relation, when linearized, gives rise to the Maxwell model. On the other hand, the approach adopted by Málek et al. [33] delivers the Maxwell model without requiring any linearization; however, the model is incapable of an instantaneous isochoric elastic response as it is assumed apriori to be not necessarily isochoric. Note that the instantaneous response is a mathematical idealization, no real response can be instantaneous. The model that is developed is capable of instantaneous elastic response, however such a response cannot be isochoric.

In this chapter, the approach used by Málek et al. [33] shall be adopted to show how models that are exactly the same as the FENE-P model but with the conformation tensor now being identified with the left Cauchy-Green tensor, can be generated. In order to obtain the FENE-P constitutive relation, one has to assume that the body stores energy like the model developed by Gent [20] and dissipates energy like a vis-

cous fluid. Then, on requiring that the rate of entropy production be maximized during the process, one can obtain an evolution equation for the left Cauchy-Green strain from the evolving natural configuration that is exactly the same as that for the conformation tensor in the FENE-P model.

The organization of the chapter is as follows:

- The necessary kinematic relations are introduced.
- The appropriate choices for the stored energy and the rate of dissipation are made.
- The maximization procedure is carried out to arrive at the FENE-P model.

2.2 Kinematic relations

This section provides preliminary kinematics required to describe the model. A detailed discussion of the kinematics of continua can be found in Truesdell and Noll [46]. Let placer κ_R denote the reference configuration and κ_t denote the current configuration of the fluid of interest, as shown in Fig. 2.1. The motion χ_{κ_R} of the fluid is a mapping that at a time t assigns to each position in the reference configuration, a corresponding position in the current configuration, i.e.,

$$\mathbf{x} := \boldsymbol{\chi}_{\kappa_R}(\mathbf{X}, t) \tag{2.1}$$

. The deformation gradient associated with the motion given by equation (2.1) is defined through

$$\boldsymbol{F}_{\kappa_R} = \frac{\partial \boldsymbol{\chi}_{\kappa_R}}{\partial \mathbf{X}}. \tag{2.2}$$

The left and right Cauchy-Green tensors $\boldsymbol{B}_{\kappa_R}$ and $\boldsymbol{C}_{\kappa_R}$ are defined through

$$\boldsymbol{B}_{\kappa_R} := \boldsymbol{F}_{\kappa_R}\boldsymbol{F}_{\kappa_R}^T, \tag{2.3}$$

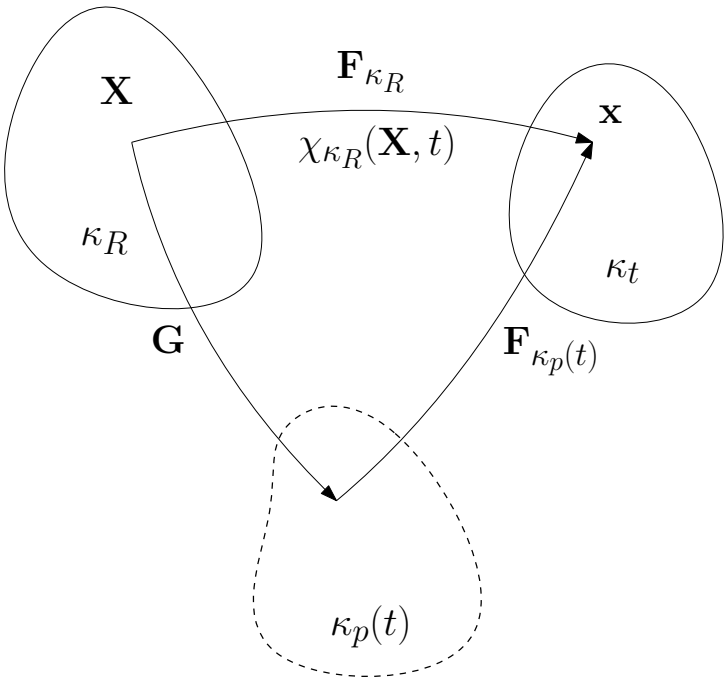

Fig. 2.1: Schematic diagram to illustrate the notion of current natural configuration of the material

$$\boldsymbol{C}_{\kappa_R} := \boldsymbol{F}^T_{\kappa_R}\boldsymbol{F}_{\kappa_R}, \tag{2.4}$$

where the superscript T denotes the transpose operation. Let $\kappa_p(t)$ denote the "natural configuration" corresponding to the current configuration κ_t. The "natural configuration" is the configuration the body in the current configuration attains when all the external stimuli are removed. There could be more than one natural configuration corresponding to the current configuration κ_t and it depends on how the external stimuli are removed (see Rajagopal [38] for a detailed discussion of the role of natural configurations in mechanics). The gradient of the mapping from $\kappa_p(t)$ to κ_t is given by $\boldsymbol{F}_{\kappa_p(t)}$. The corresponding left and right Cauchy-Green elastic stretch tensors are given by,

$$\boldsymbol{B}_{\kappa_p(t)} := \boldsymbol{F}_{\kappa_p(t)}\boldsymbol{F}^T_{\kappa_p(t)}, \tag{2.5}$$

$$\boldsymbol{C}_{\kappa_p(t)} := \boldsymbol{F}^T_{\kappa_p(t)} \boldsymbol{F}_{\kappa_p(t)}. \tag{2.6}$$

The mapping $\boldsymbol{G}$ given in Fig. 2.1 is given by

$$\boldsymbol{G} = \boldsymbol{F}_{\kappa_R \to \kappa_p(t)} := \boldsymbol{F}^{-1}_{\kappa_p(t)} \boldsymbol{F}_{\kappa_R}. \tag{2.7}$$

The tensor $\boldsymbol{C}_{\kappa_R \to \kappa_p(t)}$ is defined through:

$$\boldsymbol{C}_{\kappa_R \to \kappa_p(t)} := \boldsymbol{G}^T \boldsymbol{G}. \tag{2.8}$$

It immediately follows that

$$\boldsymbol{B}_{\kappa_R \to \kappa_p(t)} = \boldsymbol{F}_{\kappa_R} \boldsymbol{C}^{-1}_{\kappa_R \to \kappa_p(t)} \boldsymbol{F}^T_{\kappa_R}. \tag{2.9}$$

The velocity gradient $\boldsymbol{L}$ and the tensor $\boldsymbol{L}_{\kappa_p(t)}$ can be defined through:

$$\boldsymbol{L} := \dot{\boldsymbol{F}}_{\kappa_R} \boldsymbol{F}^{-1}_{\kappa_R}, \tag{2.10a}$$

$$\boldsymbol{L}_{\kappa_p(t)} := \dot{\boldsymbol{G}} \boldsymbol{G}^{-1}. \tag{2.10b}$$

The corresponding symmetric parts are given through:

$$\boldsymbol{D} := \frac{1}{2}(\boldsymbol{L} + \boldsymbol{L}^T), \tag{2.11a}$$

$$\boldsymbol{D}_{\kappa_p(t)} := \frac{1}{2}(\boldsymbol{L}_{\kappa_p(t)} + \boldsymbol{L}^T_{\kappa_p(t)}). \tag{2.11b}$$

It follows from equations (2.9) through (2.11b),

$$\dot{\boldsymbol{B}}_{\kappa_p(t)} = \boldsymbol{L} \boldsymbol{B}_{\kappa_p(t)} + \boldsymbol{B}_{\kappa_p(t)} \boldsymbol{L}^T + \boldsymbol{F}_{\kappa_R} \dot{\boldsymbol{C}}^{-1}_{\kappa_R \to \kappa_p(t)} \boldsymbol{F}^T_{\kappa_R}. \tag{2.12}$$

The 'Oldroyd' or 'upper-covected' derivative $\overset{\nabla}{\boldsymbol{B}}_{\kappa_p(t)}$ is given by,

$$\overset{\nabla}{\boldsymbol{B}}_{\kappa_p(t)} = \dot{\boldsymbol{B}}_{\kappa_p(t)} - \boldsymbol{L}\boldsymbol{B}_{\kappa_p(t)} - \boldsymbol{B}_{\kappa_p(t)}\boldsymbol{L}^T, \tag{2.13}$$

$$\overset{\nabla}{\boldsymbol{B}}_{\kappa_p(t)} = \boldsymbol{F}_{\kappa_R}\dot{\boldsymbol{C}}^{-1}_{\kappa_R\to\kappa_p(t)}\boldsymbol{F}^T_{\kappa_R}. \tag{2.14}$$

Equations (2.8), (2.10b), (2.11a) imply that

$$\dot{\boldsymbol{C}}^{-1}_{\kappa_R\to\kappa_p(t)} = -2\boldsymbol{G}^{-1}\boldsymbol{D}_{\kappa_p(t)}\boldsymbol{G}^{-T}, \tag{2.15a}$$

$$\overset{\nabla}{\boldsymbol{B}}_{\kappa_p(t)} = -2\boldsymbol{F}_{\kappa_p(t)}\boldsymbol{D}_{\kappa_p(t)}\boldsymbol{F}^T_{\kappa_p(t)}. \tag{2.15b}$$

2.3 Derivation of FENE-P type models

As mentioned in the introduction, the approach for developing models to describe viscoelastic behavior involves taking into consideration two constitutive relations, one for describing the elastic response, namely the stored energy W, and the other for describing the dissipative response, namely ξ. Here, the elastic energy proposed on a phenomenological basis by Gent [20] is picked. This model takes into account the property of limiting chain extensibility in rubber-like materials. It is important to note that the constitutive model proposed by Gent [20] assumes that the material is incompressible. An alternate compressible form of the Gent model shall be considered in the next section. The relation for the stored energy introduced by Gent [20] is as follows:

$$W = -\frac{\mu J_m}{2} ln\left(1 - \frac{I_1 - 3}{J_m}\right), \tag{2.16}$$

where $I_1 = tr\boldsymbol{B}_{\kappa_p(t)}$ and J_m is the stretch limit. The assumption for the rate of dissipation is of the form $\xi = \tilde{\xi}(\boldsymbol{D}, \boldsymbol{D}_{\kappa_p(t)}, \boldsymbol{C}_{\kappa_p(t)})$ as given in equation (2.25). Upon

differentiating equation (2.16) with respect to time we obtain,

$$\dot{W} = \frac{\mu}{2}\left(\frac{J_m}{J_m - (I_1 - 3)}\right)\frac{dI_1}{dt}. \tag{2.17}$$

Let $f(I_1) = \frac{J_m}{J_m-(I_1-3)}$. Note that this $f(I_1)$ is similar to the Peterlin function of the FENE-P model. Equation (2.17) can be re-written as follows:

$$\dot{W} = \frac{\mu}{2} f(I_1)\frac{dI_1}{dt}. \tag{2.18}$$

The time derivative of the first invariant of $\boldsymbol{B}_{\kappa_p(t)}$ is given by,

$$\frac{dI_1}{dt} = \mathbf{1} \cdot \dot{\boldsymbol{B}}_{\kappa_p(t)}. \tag{2.19}$$

It can be shown that the time derivative of $\boldsymbol{B}_{\kappa_p(t)}$ is:

$$\dot{\boldsymbol{B}}_{\kappa_p(t)} = \boldsymbol{L}\boldsymbol{B}_{\kappa_p(t)} + \boldsymbol{B}_{\kappa_p(t)}\boldsymbol{L}^T - 2\boldsymbol{F}_{\kappa_p(t)}\boldsymbol{D}_{\kappa_p(t)}\boldsymbol{F}^T_{\kappa_p(t)}. \tag{2.20}$$

From equation (2.20) one can obtain,

$$\begin{aligned}
\mathbf{1} \cdot \dot{\boldsymbol{B}}_{\kappa_p(t)} &= tr(\boldsymbol{L}\boldsymbol{B}_{\kappa_p(t)}) + tr(\boldsymbol{B}_{\kappa_p(t)}\boldsymbol{L}^T) - 2tr(\boldsymbol{F}_{\kappa_p(t)}\boldsymbol{D}_{\kappa_p(t)}\boldsymbol{F}^T_{\kappa_p(t)}), \\
&= \boldsymbol{L}^T \cdot \boldsymbol{B}_{\kappa_p(t)} + \boldsymbol{B}_{\kappa_p(t)} \cdot \boldsymbol{L}^T - 2\boldsymbol{C}_{\kappa_p(t)} \cdot \boldsymbol{D}_{\kappa_p(t)}, \\
&= 2\boldsymbol{B}_{\kappa_p(t)} \cdot \boldsymbol{D} - 2\boldsymbol{C}_{\kappa_p(t)} \cdot \boldsymbol{D}_{\kappa_p(t)}.
\end{aligned} \tag{2.21}$$

Combining equations (2.18), (2.19) and (2.21) one can arrive at,

$$\dot{W} = \mu f(I_1)(\boldsymbol{B}_{\kappa_p(t)} \cdot \boldsymbol{D} - \boldsymbol{C}_{\kappa_p(t)} \cdot \boldsymbol{D}_{\kappa_p(t)}). \tag{2.22}$$

Let ξ denote the rate of dissipation associated with the material. In an isothermal process, the rate of dissipation ξ is given by,

$$\xi = \boldsymbol{T} \cdot \boldsymbol{D} - \dot{W}, \tag{2.23}$$

where $\boldsymbol{T} \cdot \boldsymbol{D}$ is referred to as the stress power. Substituting equation (2.22) in equation (2.23),

$$\xi = \boldsymbol{T} \cdot \boldsymbol{D} - \mu f(I_1)(\boldsymbol{B}_{\kappa_p(t)} \cdot \boldsymbol{D} - \boldsymbol{C}_{\kappa_p(t)} \cdot \boldsymbol{D}_{\kappa_p(t)}). \tag{2.24}$$

As mentioned earlier, the assumption for the dissipation function is of the form $\xi = \tilde{\xi}(\boldsymbol{D}, \boldsymbol{D}_{\kappa_p(t)}, \boldsymbol{C}_{\kappa_p(t)})$. A specific assumption is made for the rate of dissipation as given by,

$$\xi = \eta \boldsymbol{D}_{\kappa_p(t)} \boldsymbol{C}_{\kappa_p(t)} \cdot \boldsymbol{D}_{\kappa_p(t)} + \eta_1 \boldsymbol{D} \cdot \boldsymbol{D}. \tag{2.25}$$

From equations (2.24) and (2.25) one can obtain,

$$\Big(\boldsymbol{T} - \mu f(I_1) \boldsymbol{B}_{\kappa_p(t)} - \eta_1 \boldsymbol{D}\Big) \cdot \boldsymbol{D} + \Big(\mu f(I_1) \boldsymbol{C}_{\kappa_p(t)} - \eta \boldsymbol{D}_{\kappa_p(t)} \boldsymbol{C}_{\kappa_p(t)}\Big) \cdot \boldsymbol{D}_{\kappa_p(t)} = 0. \tag{2.26}$$

A sufficient condition for equation (2.26) to hold is,

$$\boldsymbol{T} = -p\mathbf{1} + \mu f(I_1) \boldsymbol{B}_{\kappa_p(t)} + \eta_1 \boldsymbol{D}, \tag{2.27a}$$

$$\mu f(I_1) \boldsymbol{C}_{\kappa_p(t)} \cdot \boldsymbol{D}_{\kappa_p(t)} - \eta \boldsymbol{D}_{\kappa_p(t)} \boldsymbol{C}_{\kappa_p(t)} \cdot \boldsymbol{D}_{\kappa_p(t)} = 0, \tag{2.27b}$$

where, $p = \hat{p} + \mu f(I_1)\lambda$. The rate of dissipation ξ is maximized subject to the elastic response from the natural configuration being isochoric (which is $\mathbf{1} \cdot \boldsymbol{D}_{\kappa_p(t)} = 0$) and equation (2.27b). The constrained maximization of the dissipation function is carried

out as follows:

$$L(\boldsymbol{D}, \boldsymbol{D}_{\kappa_p(t)}) = \xi + \lambda_1\Big(\mu f(I_1)\boldsymbol{C}_{\kappa_p(t)} - \eta \boldsymbol{D}_{\kappa_p(t)}\boldsymbol{C}_{\kappa_p(t)}\Big) \cdot \boldsymbol{D}_{\kappa_p(t)} + \lambda_2 \mathbf{1} \cdot \boldsymbol{D}_{\kappa_p(t)}. \quad (2.28)$$

Taking the derivative of equation (2.28) with respect to $\boldsymbol{D}_{\kappa_p(t)}$ and equating $\frac{\partial L}{\partial \boldsymbol{D}_{\kappa_p(t)}} = 0$ and rearranging the terms it can be shown that,

$$2\eta \boldsymbol{D}_{\kappa_p(t)}\boldsymbol{C}_{\kappa_p(t)}\frac{(1-\lambda_1)}{\lambda_1} + \mu f(I_1)\boldsymbol{C}_{\kappa_p(t)} + \frac{\lambda_2}{\lambda_1}\mathbf{1} = 0. \quad (2.29)$$

Taking the dot product of equation (2.29) with $\boldsymbol{D}_{\kappa_p(t)}$ leads to,

$$\eta\frac{(1-\lambda_1)}{\lambda_1}\boldsymbol{D}_{\kappa_p(t)}\boldsymbol{C}_{\kappa_p(t)} \cdot \boldsymbol{D}_{\kappa_p(t)} + \mu f(I_1)\boldsymbol{C}_{\kappa_p(t)} \cdot \boldsymbol{D}_{\kappa_p(t)} = 0. \quad (2.30)$$

Comparing equation (2.30) with equation (2.27b) one can see that $\lambda_1 = -1$. Equation (2.29) can be now rewritten as,

$$\mu f(I_1)\boldsymbol{C}_{\kappa_p(t)} - 2\eta \boldsymbol{D}_{\kappa_p(t)}\boldsymbol{C}_{\kappa_p(t)} - \frac{\lambda_2}{2}\mathbf{1} = 0. \quad (2.31)$$

The deformation gradient $\boldsymbol{F}_{\kappa_p(t)}$ can be split as follows,

$$\boldsymbol{F}_{\kappa_p(t)} = \boldsymbol{R}\boldsymbol{U}_{\kappa_p(t)}, \quad \forall \boldsymbol{R} \in \boldsymbol{Q} \ni \boldsymbol{Q}\boldsymbol{Q}^T = \mathbf{1}. \quad (2.32)$$

It follows from equation (2.32) that,

$$\boldsymbol{C}_{\kappa_p(t)} = \boldsymbol{U}^2_{\kappa_p(t)}, \quad (2.33)$$

where, $\boldsymbol{U}_{\kappa_p(t)}$ is the right stretch tensor in the polar decomposition. Substituting equation (2.33) in equation (2.31) and replacing λ_2 by 2λ,

$$\mu f(I_1)\boldsymbol{U}^2_{\kappa_p(t)} - 2\eta \boldsymbol{D}_{\kappa_p(t)}\boldsymbol{U}^2_{\kappa_p(t)} - \lambda \mathbf{1} = 0. \tag{2.34}$$

Pre and post multiplying equation (2.34) with $\boldsymbol{U}_{\kappa_p(t)}$ and $\boldsymbol{U}^{-1}_{\kappa_p(t)}$ and rearranging the terms as shown in equations (2.35a), (2.35b), (2.35c) and taking trace of the resultant equation one can arrive at equation (2.35c) as shown below,

$$\mu f(I_1)\boldsymbol{U}^2_{\kappa_p(t)} - 2\eta \boldsymbol{U}_{\kappa_p(t)}\boldsymbol{D}_{\kappa_p(t)}\boldsymbol{U}_{\kappa_p(t)} - \lambda \mathbf{1} = 0, \tag{2.35a}$$

$$\mu f(I_1)\mathbf{1} - 2\eta \boldsymbol{D}_{\kappa_p(t)} - \lambda \boldsymbol{U}^{-2}_{\kappa_p(t)} = 0, \tag{2.35b}$$

$$3\mu f(I_1) - \lambda tr(\boldsymbol{B}^{-1}_{\kappa_p(t)}) = 0. \tag{2.35c}$$

Note that $tr(\boldsymbol{D}_{\kappa_p(t)}) = 0$ due to the incompressibilty condition that has been imposed on the elastic response. Also, $tr(\boldsymbol{U}^{-2}_{\kappa_p(t)}) = tr(\boldsymbol{C}^{-1}_{\kappa_p(t)}) = tr(\boldsymbol{B}^{-1}_{\kappa_p(t)})$ implies $\lambda = \frac{3\mu f(I_1)}{tr(\boldsymbol{B}^{-1}_{\kappa_p(t)})}$. Rewriting equation (2.31) in terms of $\boldsymbol{F}_{\kappa_p(t)}$ and pre and post multiplying by $\boldsymbol{F}_{\kappa_p(t)}$ and $\boldsymbol{F}^{-1}_{\kappa_p(t)}$,

$$\mu f(I_1)\boldsymbol{F}^T_{\kappa_p(t)}\boldsymbol{F}_{\kappa_p(t)} - 2\eta \boldsymbol{D}_{\kappa_p(t)}\boldsymbol{F}^T_{\kappa_p(t)}\boldsymbol{F}_{\kappa_p(t)} - \frac{3\mu f(I_1)}{tr(\boldsymbol{B}^{-1}_{\kappa_p(t)})}\mathbf{1} = 0, \tag{2.36a}$$

$$\mu f(I_1)\boldsymbol{F}_{\kappa_p(t)}\boldsymbol{F}^T_{\kappa_p(t)} - 2\eta \boldsymbol{F}_{\kappa_p(t)}\boldsymbol{D}_{\kappa_p(t)}\boldsymbol{F}^T_{\kappa_p(t)} - \frac{3\mu f(I_1)}{tr(\boldsymbol{B}^{-1}_{\kappa_p(t)})}\mathbf{1} = 0, \tag{2.36b}$$

$$\mu f(I_1)\boldsymbol{B}_{\kappa_p(t)} - 2\eta \boldsymbol{F}_{\kappa_p(t)}\boldsymbol{D}_{\kappa_p(t)}\boldsymbol{F}^T_{\kappa_p(t)} - \frac{3\mu f(I_1)}{tr(\boldsymbol{B}^{-1}_{\kappa_p(t)})}\mathbf{1} = 0. \tag{2.36c}$$

Combining equation (2.15b) and equation (2.36c) one can arrive at,

$$-\frac{1}{2}\overset{\triangledown}{\boldsymbol{B}}_{\kappa_p(t)} = \frac{\mu f(I_1)}{\eta}\Big(\boldsymbol{B}_{\kappa_p(t)} - \frac{3}{tr(\boldsymbol{B}^{-1}_{\kappa_p(t)})}\mathbf{1}\Big). \tag{2.37}$$

2.4 The FENE-P model derivation

In the previous section, the stored elastic energy function proposed by Gent [20] was chosen, which assumed that the material is incompressible. This incompressibility assumption is a theoretical idealization. Málek et al. [33] pointed out that viscoelastic models with three-dimensional generalizations of the spring-dashpot analogs lead to models in which the individual components are compressible. In this section, the approach used by Málek et al. [33], which does not require the elastic response to be isochoric, shall be adopted. To achieve this, a modified version of the Gent model [20] proposed by Horgan and Saccomandi [27] is considered. This model takes into account the compressibility of the material. The stored energy function for such a material is given by the following,

$$W = -\frac{\mu}{2}\left(J_m \ln\left(1 - \frac{I_1 - 3}{J_m}\right) + \ln(\det \boldsymbol{B}_{\kappa_p(t)})\right), \tag{2.38}$$

where $I_1 = tr\boldsymbol{B}_{\kappa_p(t)}$ and J_m is the stretch limit. Upon differentiating equation (2.38) with respect to time one can obtain,

$$\dot{W} = \frac{\mu}{2}\left(\left(\frac{J_m}{J_m - (I_1 - 3)}\right)\frac{dI_1}{dt} - \overline{\ln(\det \boldsymbol{B}_{\kappa_p(t)})}^{\cdot}\right), \tag{2.39}$$

The result we have in equation (2.22) can be extended to the above equation as follows,

$$\dot{W} = \frac{\mu}{2}(2f(I_1)(\boldsymbol{B}_{\kappa_p(t)} \cdot \boldsymbol{D} - \boldsymbol{C}_{\kappa_p(t)} \cdot \boldsymbol{D}_{\kappa_p(t)}) - \overline{\ln(\det \boldsymbol{B}_{\kappa_p(t)})}^{\cdot}\Big). \tag{2.40}$$

where, $f(I_1) = \frac{J_m}{J_m-(I_1-3)}$. Also to evaluate $\overline{\ln(\det \dot{\boldsymbol{B}}_{\kappa_p(t)})}$ one can use the relation in equation (2.13),

$$\begin{aligned}
\overline{\ln(\det \dot{\boldsymbol{B}}_{\kappa_p(t)})} &= tr(\dot{\boldsymbol{B}}_{\kappa_p(t)}\boldsymbol{B}^{-1}_{\kappa_p(t)}), \\
&= tr((\boldsymbol{L}\boldsymbol{B}_{\kappa_p(t)} + \boldsymbol{B}_{\kappa_p(t)}\boldsymbol{L}^T - 2\boldsymbol{F}_{\kappa_p(t)}\boldsymbol{D}_{\kappa_p(t)}\boldsymbol{F}^T_{\kappa_p(t)})\boldsymbol{B}^{-1}_{\kappa_p(t)}), \\
&= tr(2\boldsymbol{D} - 2\boldsymbol{D}_{\kappa_p(t)}), \\
&= 2(\mathbf{1}\cdot\boldsymbol{D} - \mathbf{1}\cdot\boldsymbol{D}_{\kappa_p(t)}).
\end{aligned} \tag{2.41}$$

In section 2.3, the condition of incompressibility was imposed on the material for the derivation of FENE-P-type models. Recall that the total deformation gradient $\boldsymbol{F}_{\kappa_R}$ was split into a purely elastic part corresponding to $\boldsymbol{F}_{\kappa_p(t)}$ and a transformation associated with the dissipative process related to the body's changing natural configuration, referred to as $\boldsymbol{G}$. Condition of incompressibility for the total solution corresponds to $\det \boldsymbol{F}_{\kappa_R} = 1$. This upon differentiation with respect to time corresponds $tr(\boldsymbol{D}_{\kappa_R}) = 0$ or simply $tr(\boldsymbol{D}) = 0$. Unlike the previous derivation, one does not assume that the elastic response from the evolving natural configuration or the dissipative response associated with the evolution of the natural configuration is isochoric. Combining equation (2.40) and equation (2.41),

$$\dot{W} = \mu\Big(f(I_1)\boldsymbol{B}_{\kappa_p(t)}\cdot\boldsymbol{D} - (f(I_1)(\boldsymbol{C}_{\kappa_p(t)} - \mathbf{1})\cdot\boldsymbol{D}_{\kappa_p(t)}\Big). \tag{2.42}$$

Recall that in an isothermal process, the rate of dissipation is given by equation (2.23). Substituting the compressible Gent model stored energy form in equation (2.23), one can obtain the following equation for the dissipation rate ξ,

$$\xi = \boldsymbol{T}\cdot\boldsymbol{D} - \mu\Big(f(I_1)\boldsymbol{B}_{\kappa_p(t)}\cdot\boldsymbol{D} - (f(I_1)(\boldsymbol{C}_{\kappa_p(t)} - \mathbf{1})\cdot\boldsymbol{D}_{\kappa_p(t)}\Big). \tag{2.43}$$

As mentioned in the previous section, the dissipation function $\xi = \tilde{\xi}(\boldsymbol{D}, \boldsymbol{D}_{\kappa_p(t)}, \boldsymbol{C}_{\kappa_p(t)})$ is assumed to be of the form given in equation (2.26). By equating equation (2.25) and equation (2.43) one can obtain,

$$\Big(\boldsymbol{T} - \mu f(I_1)\boldsymbol{B}_{\kappa_p(t)} - \eta_1 \boldsymbol{D}\Big) \cdot \boldsymbol{D} + \Big(\mu(f(I_1)(\boldsymbol{C}_{\kappa_p(t)} - \boldsymbol{1}) - \eta \boldsymbol{D}_{\kappa_p(t)}\boldsymbol{C}_{\kappa_p(t)}\Big) \cdot \boldsymbol{D}_{\kappa_p(t)} = 0. \tag{2.44}$$

The rate of dissipation $\xi = \tilde{\xi}(\boldsymbol{D}, \boldsymbol{D}_{\kappa_p(t)}, \boldsymbol{C}_{\kappa_p(t)})$ is now maximized. This idea follows from the notion that the rate of entropy production is maximized. In order to achieve this, a Langrange function $L(\boldsymbol{D}, \boldsymbol{D}_{\kappa_p(t)})$ is introduced, subject to the constraints given by equation (2.43) and the isochoric total response of the fluid, $tr(\boldsymbol{D}) = 0$.

$$L(\boldsymbol{D}, \boldsymbol{D}_{\kappa_p(t)}) = \xi + \lambda_1\Big(\xi - \boldsymbol{T}\cdot\boldsymbol{D} - \mu\Big(f(I_1)\boldsymbol{B}_{\kappa_p(t)}\cdot\boldsymbol{D} - (f(I_1)(\boldsymbol{C}_{\kappa_p(t)} - \boldsymbol{1})\cdot\boldsymbol{D}_{\kappa_p(t)}\Big)\Big) + \lambda_2 \boldsymbol{1}\cdot\boldsymbol{D}. \tag{2.45}$$

Maximization of ξ is achieved by solving for $\frac{\partial L}{\partial \boldsymbol{D}} = \boldsymbol{0}$ and $\frac{\partial L}{\partial \boldsymbol{D}_{\kappa_p(t)}} = \boldsymbol{0}$;

$$\frac{\partial L}{\partial \boldsymbol{D}} = \boldsymbol{0} = (1 + \lambda_1)\frac{\partial \xi}{\partial \boldsymbol{D}} + \lambda_1(\boldsymbol{T} - \mu\Big(f(I_1)\boldsymbol{B}_{\kappa_p(t)}) + \lambda_2 \boldsymbol{1}, \tag{2.46}$$

$$\frac{\partial L}{\partial \boldsymbol{D}_{\kappa_p(t)}} = \boldsymbol{0} = (1 + \lambda_1)\frac{\partial \xi}{\partial \boldsymbol{D}_{\kappa_p(t)}} + \lambda_1(f(I_1)(\boldsymbol{C}_{\kappa_p(t)} - \boldsymbol{1})). \tag{2.47}$$

Upon differentiation equation (2.25), $\frac{\partial \xi}{\partial \boldsymbol{D}} = 2\eta_1 \boldsymbol{D}$ and $\frac{\partial \xi}{\partial \boldsymbol{D}_{\kappa_p(t)}} = 2\eta \boldsymbol{D}_{\kappa_p(t)}\boldsymbol{C}_{\kappa_p(t)}$. Making the appropriate substitutions and taking scalar product of equation (2.46) with $\boldsymbol{D}$ and equation (2.47) with $\boldsymbol{D}_{\kappa_p(t)}$ one can obtain the following equations,

$$2(1 + \lambda_1)\eta_1 \boldsymbol{D}\cdot\boldsymbol{D} + \lambda_1(\boldsymbol{T} - \mu\Big(f(I_1)\boldsymbol{B}_{\kappa_p(t)}) \cdot \boldsymbol{D} + \lambda_2 \boldsymbol{1}\cdot\boldsymbol{D} = 0, \tag{2.48}$$

$$2(1 + \lambda_1)\eta \boldsymbol{D}_{\kappa_p(t)}\boldsymbol{C}_{\kappa_p(t)} \cdot \boldsymbol{D}_{\kappa_p(t)} + \lambda_1(f(I_1)(\boldsymbol{C}_{\kappa_p(t)} - \boldsymbol{1})) \cdot \boldsymbol{D}_{\kappa_p(t)} = 0. \tag{2.49}$$

Using the constraint of incompressibility of the fluid, which is $\mathbf{1} \cdot \boldsymbol{D} = 0$ along with equation (2.25) and equation (2.43), one can show that the combination of equation (2.48) and equation (2.49) can be reduced to,

$$2(1 + \lambda_1)\xi - \lambda_1\xi = 0. \tag{2.50}$$

Equation (2.50) requires $\lambda_1 = -2$. One can now reduce equation (2.46) as follows

$$\boldsymbol{T} = -p\mathbf{1} + \eta_1\boldsymbol{D} + \mu(f(I_1)\boldsymbol{B}_{\kappa_p(t)} - \mathbf{1}), \tag{2.51}$$

where, $p = -\Big(\frac{\lambda_2}{2} + \mu\Big)$. Consider the equation (2.47),

$$\eta\boldsymbol{D}_{\kappa_p(t)}\boldsymbol{C}_{\kappa_p(t)} = \mu(f(I_1)\boldsymbol{C}_{\kappa_p(t)} - \mathbf{1}), \tag{2.52a}$$

$$\eta\boldsymbol{D}_{\kappa_p(t)}\boldsymbol{F}^T_{\kappa_p(t)}\boldsymbol{F}_{\kappa_p(t)} = \mu(f(I_1)\boldsymbol{F}^T_{\kappa_p(t)}\boldsymbol{F}_{\kappa_p(t)} - \mathbf{1}), \tag{2.52b}$$

$$\eta\boldsymbol{F}_{\kappa_p(t)}\boldsymbol{D}_{\kappa_p(t)}\boldsymbol{F}^T_{\kappa_p(t)} = \mu(f(I_1)\boldsymbol{F}_{\kappa_p(t)}\boldsymbol{F}^T_{\kappa_p(t)} - \mathbf{1}). \tag{2.52c}$$

Combining equation (2.15b) and equation (2.52c) one can show that,

$$-\frac{1}{2}\overset{\nabla}{\boldsymbol{B}}_{\kappa_p(t)} = \frac{\mu}{\eta}\Big(f(I_1)\boldsymbol{B}_{\kappa_p(t)} - \mathbf{1}\Big). \tag{2.53}$$

Thus, a constitutive relation that is identical in form the FENE-P model is obtained.

2.5 Comparison with the FENE-P model

Recall the evolution equation of the conformation tensor $\boldsymbol{C}$ is given by equation (1.11) and can be rewritten as follows,

$$\frac{D\boldsymbol{C}}{Dt} = \left(\frac{\partial \boldsymbol{u}}{\partial \boldsymbol{x}}\right)^T \boldsymbol{C} + \boldsymbol{C}\left(\frac{\partial \boldsymbol{u}}{\partial \boldsymbol{x}}\right) - \frac{1}{\lambda}[f(R)\boldsymbol{C} - \boldsymbol{I}] \tag{2.54a}$$

$$-\overset{\nabla}{\boldsymbol{C}} = \frac{1}{\lambda}\Big(f(R^2)\boldsymbol{C} - \mathbf{1}\Big) \tag{2.54b}$$

Where λ is the relaxation time constant of the material and $f(R) = \frac{L_0^2-3}{L_0^2-R^2}$ (R^2 is the trace of $\boldsymbol{C}$, L_0 is the maximum extension of the polymer molecules). Comparing equation (2.54b) with equation (2.53) one can identify that the role played by Peterlin function $f(R)$ is similar to that of $f(I_1)$ and the relaxation time constant $\lambda = \eta/(2\mu)$. Similarly, tensor $\boldsymbol{B}_{\kappa_p(t)}$ and the conformation tensor $\boldsymbol{C}$ play the same roles with respect to the constitutive models. Hence, it has been shown that the FENE-P model can be derived from a generalized compressible form of stored energy proposed by Horgan and Saccomandi [27].

3. ANALYTICAL SOLUTION AND CODE VERIFICATION

The primary objective of this research is to simulate and capture the onset of the viscoelastic phenomenon of elastic turbulence in dilute polymer solutions. The first step towards this purpose is to establish a reliable viscoelastic solver. As has been discussed in the previous chapters the rheology of dilute polymer solutions on a macro-scale is determined by the micro-structures of the polymer molecules involved. These elastic polymer molecules interact with the fluid flow and supplement the fluid with an additional polymeric stress component. For this work, the FENE-P model is chosen to model the flow of these viscoelastic dilute polymer solutions. This chapter focuses on two objectives.

- Obtaining the exact solutions for steady fully developed laminar pipe flow for a FENE-P fluid.
- Comparing the exact solutions with the numerical solutions that were developed using a finite volume solver.

The numerical solutions have been carried out to not only compare them with the exact solutions but also to study the effects of grid resolution, boundary conditions, and artificial diffusion.

3.1 General problem formulation

The problem of interest is governed by the momentum equation and the continuity equation for an incompressible fluid given respectively by:

$$\rho \frac{D\boldsymbol{u}}{Dt} = -\frac{\partial p}{\partial \boldsymbol{x}} + \nabla \cdot \boldsymbol{T}, \tag{3.1}$$

and

$$\nabla \cdot \boldsymbol{u} = 0, \tag{3.2}$$

where $\boldsymbol{u}$ is the fluid velocity, p is the pressure, $\boldsymbol{T}$ is the stress tensor, ρ is the density. For a dilute polymer solution, the stress is decomposed into a Newtonian component and a polymeric component via:

$$\boldsymbol{T} = \mu_0 \beta \boldsymbol{D} + \boldsymbol{\tau}^p, \tag{3.3}$$

where τ_p is the polymeric component of the stress, μ_0 is the solution viscosity, β is the ratio of the solvent viscosity to the solution viscosity, and $\boldsymbol{D}$ is the symmetric part of the velocity gradient. For a FENE-P fluid the polymeric stress is given by:

$$\boldsymbol{\tau}^p = \frac{\mu_0(1-\beta)}{\lambda}[f(R)\boldsymbol{C} - \boldsymbol{I}], \tag{3.4}$$

where λ is the polymer relaxation time, $\boldsymbol{C}$ is the conformation tensor defined as the tensor representing the average over all possible molecular configurations of the production of the end-to-end vectors associated with the polymer molecular length, $R^2 = tr(\boldsymbol{C})$, $\boldsymbol{I}$ is the unit tensor, and $f(R) = \frac{L_0^2 - 3}{L_0^2 - R^2}$ is the Peterlin function, where L_0 is the maximum allowable molecular extension. In the equations above, and in all subsequent ones, $\boldsymbol{C}$, L_0, and R are made non-dimensional by the rest length, or square of the length as appropriate, of the polymer molecule. Finally, the conformation tensor $\boldsymbol{C}$ is governed by:

$$\frac{D\boldsymbol{C}}{Dt} = \left(\frac{\partial \boldsymbol{u}}{\partial \boldsymbol{x}}\right)^T \boldsymbol{C} + \boldsymbol{C}\left(\frac{\partial \boldsymbol{u}}{\partial \boldsymbol{x}}\right) - \frac{1}{\lambda}[f(R)\boldsymbol{C} - \boldsymbol{I}] + \Gamma \nabla^2 \boldsymbol{C}, \tag{3.5}$$

where Γ is the polymer diffusivity. The inclusion of polymer diffusion, although not included in the original formulation of the FENE-P model, is included here since one of our objectives is to investigate the effects of diffusion on the solutions for pipe flow.

3.2 Exact solution for a fully developed laminar pipe flow for a FENE-P fluid

The exact solution for steady, fully developed laminar pipe flow for a FENE-P fluid has been derived, details of which are provided below. For this purpose cylindrical coordinates r, θ and z, defined as the coordinate perpendicular to the pipe axis, the azimuthal coordinate, and the coordinate parallel to the pipe axis are used. u_r, u_θ and u_z are used to define the radial, azimuthal, and streamwise velocity components respectively. Solutions are sought of the form $u_r = u_\theta = 0$ and $u_z = u_z(r)$, which makes all components of the conformation, $\boldsymbol{C}$ tensor depend only on r.

Although similar solutions were obtained by Cruz et al. [13], for reasons of clarity and completeness the derivation has been included here. With these assumptions, six equations for the unique components of the symmetric conformation tensor, C_{rr}, $C_{r\theta}$, C_{rz}, $C_{\theta\theta}$, $C_{\theta z}$, C_{zz}, are obtained from equation (3.5) with $\Gamma = 0$, and are given below:

$$0 = C_{rr}\frac{du_z}{dr} - \frac{1}{\lambda}[f(R)C_{rz}], \tag{3.6}$$

$$0 = 2C_{rz}\frac{du_z}{dr} - \frac{1}{\lambda}[f(R)C_{zz} - 1]. \tag{3.7}$$

It follows from equation (3.6), equation (3.7) that $C_{rr} = \frac{1}{f(R)}$, $C_{r\theta} = 0$, $C_{\theta\theta} = \frac{1}{f(R)}$, and $C_{\theta z} = \frac{1}{f(R)}$. From equation (3.4) and the expressions above for the conformation

tensor, the polymeric stress $\boldsymbol{\tau}_p$ are determined as follows, where the superscript p has been removed for clarity:

$$\tau_{rz} = \frac{\mu_p}{\lambda}[f(R)C_{rz}], \tag{3.8}$$

$$\tau_{zz} = \frac{\mu_p}{\lambda}[f(R)C_{zz} - 1], \tag{3.9}$$

and $\tau_{rr} = \tau_{r\theta} = \tau_{\theta\theta} = \tau_{\theta z} = 0$. Using equation (3.6), equation (3.7), equation (3.8) and equation (3.9), and $C_{rr} = \frac{1}{f(R)}$, the following relationships can be obtained:

$$0 = \mu_p \frac{du_z}{dr} - f(R)\tau_{rz}, \tag{3.10}$$

and

$$0 = 2\lambda\tau_{rz}\frac{du_z}{dr} - f(R)\tau_{zz.} \tag{3.11}$$

Using $C_{rr} = \frac{1}{f(R)}$, $C_{\theta\theta} = \frac{1}{f(R)}$, and equation (3.9), the Peterlin function can be expressed as:

$$f(R) = F(\tau_{zz}) = 1 + \frac{\lambda\tau_{zz}}{\mu_p L^2}, \tag{3.12}$$

and equation (3.10) and equation (3.11) are used to give:

$$\tau_{zz} = \frac{2\lambda}{\mu_p}(\tau_{rz})^2. \tag{3.13}$$

From equation (3.1), the momentum equation in the z-direction is:

$$0 = -p_z + \mu_s \frac{\partial}{r\partial r}\left(r\frac{\partial u_z}{\partial r}\right) + \frac{\partial(r\tau_{rz})}{r\partial r}, \tag{3.14}$$

where $p_z < 0$ is a temporally and spatially constant driving pressure gradient in the z-direction. Integration of equation (3.14) from the pipe center ($r = 0$) to an

arbitrary radial position r, using the symmetry conditions $\frac{du_r}{dr} = 0$ and consequently $\tau_{rz} = 0$, gives:

$$0 = -\frac{p_z r}{2} + \mu_s \frac{du_z}{dr} + \tau_{rz}. \tag{3.15}$$

Substitution of equation (3.10), equation (3.12), equation (3.13) into equation (3.14) gives, for τ_{rz}:

$$\tau_{rz}^3 + 3A\tau_{rz} - 2B(r) = 0, \tag{3.16}$$

where

$$A = \left(\frac{\mu_s + \mu_p}{\mu_s}\right)\left(\frac{\mu_p^2 L^2}{6\lambda^2}\right), \tag{3.17}$$

and

$$B(r) = \left(\frac{\mu_p}{\mu_s}\right)\left(\frac{\mu_p^2 L^2}{8\lambda^2}\right) p_z r. \tag{3.18}$$

It is important to note that the equation (3.16) is identical to Cruz et al. [13] with $\epsilon = L^2$, where ϵ is used in the Phan-Thien-Tanner (PTT) model to representation extensional flow properties. The exact solution to equation (3.16) for τ_{rz} is:

$$\begin{aligned} A &= \frac{\left(\frac{\mu_s+\mu_p}{\mu_s}\right)}{\frac{6\lambda^2}{\mu_p^2 L^2}}, \\ B &= \frac{\frac{\mu_p}{\mu_s}\left(\frac{p_z R}{2}\right)}{\frac{4\lambda^2}{\mu_p^2 L^2}}. \end{aligned} \tag{3.19}$$

Then τ_{zz}, C_{rz} and C_{zz} can be obtained from Eqs. (3.8)

3.3 Computational technique

The software of choice to carry out the simulations is ANSYS-FLUENT. Fig 3.1 is the flow chart of the algorithm used to solve the constitutive equations of the FENE-P model. This algorithm is a modification of the SIMPLE algorithm. SIMPLE is an

acronym for Semi-Implicit Method for Pressure-Linked Equations. In this method the governing equations are discretized in a strong-conservation form using a finite-volume approach. The non-linearities are tackled in the so called 'outer loop', which is performed several times per time step until a satisfactory convergence is reached. In each 'outer loop' the momentum conservation equation, mass conservation and the modified version of the transport equation given in equation (3.20) is assembled into a system of linear equations based on all the equation terms (time-derivatives, convection, diffusion, source terms) in the associated mesh. This process creates a relation between a sparse matrix of implicit terms (A) and a vector of explicit terms $\boldsymbol{b}$, which can be solved to find updated values for the flow field $\boldsymbol{x}$: $\boldsymbol{Ax} = \boldsymbol{b}$. Iterative solvers are used to solve for $\boldsymbol{x}$ until a specified convergence tolerance is used.

A series of simulations were performed using using ANSYS-FLUENT to determine the effects of diffusion and the boundary conditions on the solutions for laminar of a FENE-P fluid. ANSYS-FLUENT contains the capability of solving an advective-diffusion equation for a scalar ϕ as follows,

$$\frac{\partial \rho\phi}{\partial t} + \frac{\partial}{\partial x_i}\left(\rho u_i \phi - \Gamma \frac{\partial \phi}{\partial x_i}\right) = S_\phi. \tag{3.20}$$

where ρ is the density, u_i are the components of the fluid velocity, Γ is diffussion coefficient, and S_ϕ is the source term. Using this capability, the six unique components of the conformation tensor can be determined by letting ϕ be any of the six components of C_{ij} and including the stretching and rotational terms in equation (3.5) in the source term, S_ϕ. The use of this model to solve equation (3.5) was achieved by writing appropriate user-defined functions in the C-language. Once the conformation tensor is obtained, the polymeric stresses are determined from equation (3.4). The components of the divergence of the polymeric stress are then added as extra source

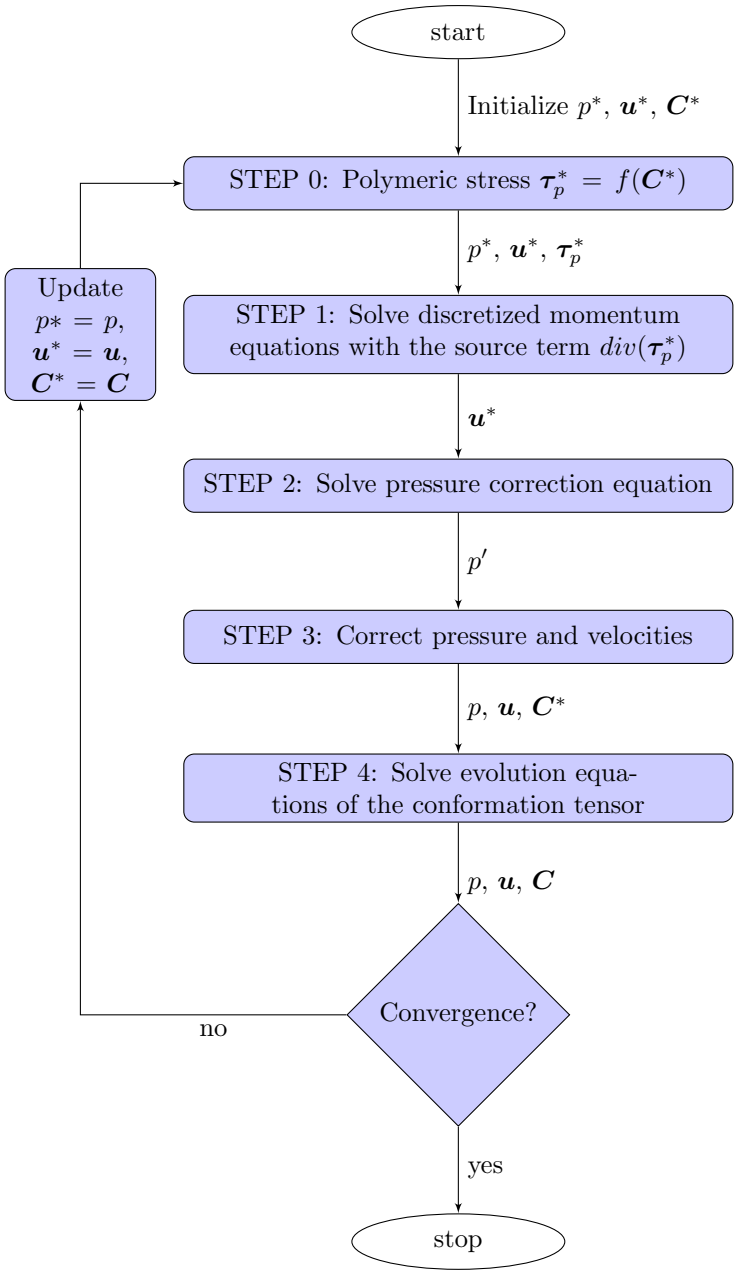

Fig. 3.1: An extension to the SIMPLE algorithm for viscoelastic fluids

terms to the momentum equation (3.1) which is then used to determine the flow velocity in a pipe flow geometry. All the parameters for the simulations performed are listed in Table 3.1.

Table 3.1: Simulation parameters

Parameter	Representation	Value
Density	ρ	$1 \times 10^3\,\mathrm{kg/m^3}$
Solvent viscosity	μ_s	$1 \times 10^{-3}\,\mathrm{Pa\text{-}s}$
Polymer viscosity	μ_p	$1.1111 \times 10^{-4}\,\mathrm{Pa\text{-}s}$
Viscosity ratio	β	0.9
Polymer time scale	λ	$1\,\mathrm{s}$
Pipe diameter	D	$1 \times 10^{-3}\,\mathrm{m}$
Pipe length	L	$20 \times 10^{-3}\,\mathrm{m}$
Added diffusion	Γ	Simulation specific
Reynolds number	Re	$\beta\left(\rho U D/\mu_s\right)$
Weissenberg number	Wi	$\lambda U/D$
Schmidt number	Sc	$\mu_s/(\beta\Gamma)$
Maximum polymer extensibility	L_0^2	$10,000$

It is important to pay attention to the hyperbolic nature of the conformation tensor evolution equation. Because of the absence of the diffusion term, sharp gradients of polymer stress, in theory may be possibly formed. Capturing these gradients can pose a challenge to the stability of the computational techniques employed. In addition to the evolution equations of C_{ij} through out the entire field, there is also a constant artificial diffusion. For the purpose of rendering stability to the solution an additional diffusion is added, modifying the equation (3.5).

3.4 Boundary conditions

Along the entire inlet $\boldsymbol{C} = \boldsymbol{I}$. At the domain outlet, no-flux boundary condition is applied to both velocities as well as $\boldsymbol{C}$. Along the wall of the pipe a no-slip con-

dition is applied for the fluid velocity. In general, the hyperbolic nature of the $\boldsymbol{C}$ evolution equation would require that no boundary condition for $\boldsymbol{C}$ be specified at the wall, however, due to the presence of additional diffusion (including the inherent artificial diffusion of the numerical scheme), a boundary condition needs to be explicitly enforced on $\boldsymbol{C}$. The additional diffusion term transforms the hyperbolic evolution equations to parabolic. A no-flux boundary condition has been imposed on the components of $\boldsymbol{C}$ along the pipe's wall.

3.5 Results and discussions

The optimum value for the number of cells used for the following simulations has been determined by carrying out a series of simulations to perform the grid independence study, the details of which are given in Table 3.2. The Weissenberg number Wi and the Reynolds number Re are varied by changing the inlet velocity U (Refer to Table 3.1). The inlet velocity U has been picked such that the $Re = 1$ and $Wi = 1.1111$. For each simulation the area average value of the $tr(\boldsymbol{C})$ has been calculated at the outlet of the pipe and plotted against the corresponding number of cells used. Fig. 3.2 shows that grid independence is achieved at 52,600 cells for the given set of simulations.

Table 3.2: Different meshes for studying the grid independence

No.	Re	Wi	Sc	Grid nodes	L/D
1	1	1.1111	11	8000	20
2	1	1.1111	11	24480	20
3	1	1.1111	11	52600	20
4	1	1.1111	11	64000	20
5	1	1.1111	11	250000	20
6	1	1.1111	11	512000	20

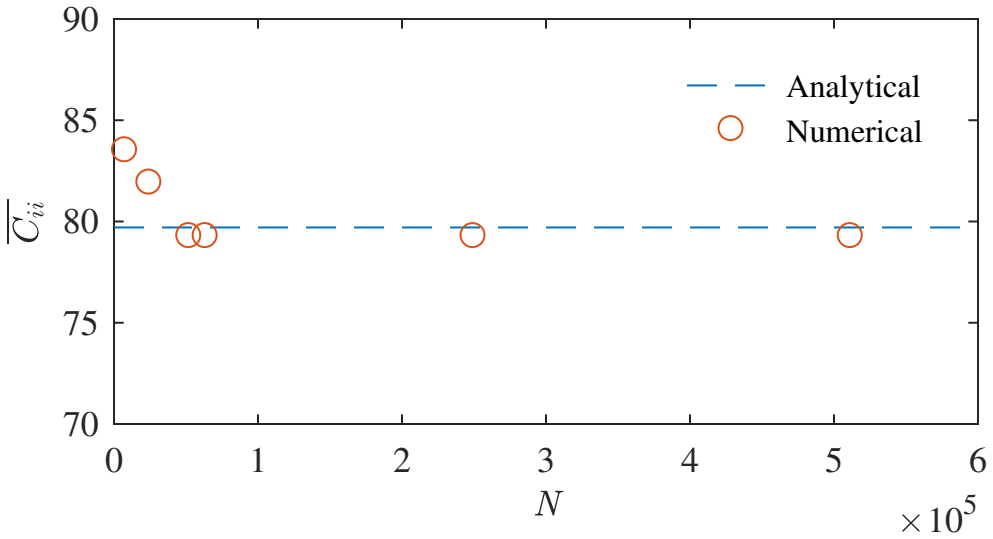

Fig. 3.2: Area weighted average of $(C_{zz} + C_{rr} + C_{\theta\theta})$ at the outlet for Re 1 Wi 1.1111

A series of simulations with varying Re and Wi were conducted to test the validity of the simulation code (Refer to Table 3.3). Fig. 3.3 through Fig. 3.10 show the comparison of C_{rz} and C_{rr} with the exact solution with varying Re and Wi.

Table 3.3: Simulations with varying Wi

No.	Re	Wi	Sc	Grid nodes	L/D	Fig.
1	1	1.1111	11	52600	20	3.3, 3.4
2	2	2.2222	11	52600	20	3.5, 3.6
3	3	3.3333	11	52600	20	3.7, 3.8
4	4	4.4444	1.1	52600	20	3.9, 3.10

It needs to be brought to the reader's attention that the numerical solution digresses from the analytical solution close to the walls because of the no-flux boundary condition that was imposed on the conformation tensor components. This digression

can be minimized by refining the mesh and further decreasing the added diffusion. However, refining the mesh and decreasing the added diffusion directly affects the stability of the numerical scheme. Finding the optimal mesh refinement and added diffusion varies with the Weissenberg number Wi. It is important to note that, with an increase in Wi the value of added diffusion Γ needs to be increased to attain stable, converging solutions. Fig. 3.9 and Fig. 3.10 show the comparison of numerical solution and exact solution at $Wi = 4.4444$ with $\Gamma = 1 \times 10^{-3}\,\mathrm{kgm^{-1}s^{-1}}$. Because of the high value of Γ required for convergence, the numerical results are unable to capture the steep gradients shown by the exact solutions of the same, at the wall.

Fig. 3.11 and Fig. 3.12 show the effect of the added diffusion Γ on the numerical solution. As pointed out earlier, an increase of added diffusion Γ improves the stability of the solution, compromising on the accuracy (Refer to Table 3.4).

Table 3.4: Different Schmidt numbers

No.	Re	Wi	Sc	Grid nodes	L/D
1	1	1.1111	11	52600	20
2	1	1.1111	1.11	52600	20
3	1	1.1111	0.11	52600	20

3.6 Obstacles

There exist several obstacles related to the simulation of viscoelastic fluid flow. The biggest hurdle is dealing with the convergence issues at high Wi. Specifically, numerical breakdown occurs when solving the FENE-P model (or any another model that involves hyperbolic PDEs). For the current study, numerical instabilities and convergence issues start to emerge for $Wi > 4$. However the elastic instabilities

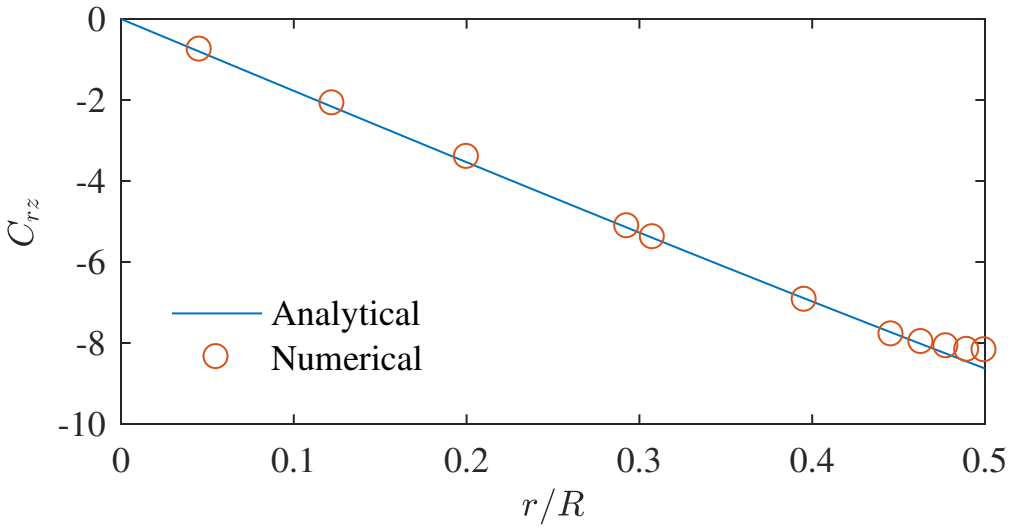

Fig. 3.3: C_{rz} for Re 1 Wi 1.1111

and elastic turbulence are reported to occur only at higher Wi. This numerical break down that occurs at moderately high Weissenberg numbers is called the High Weissenberg Number Problem (HWNP). This breakdown could be attributed to the following reasons:

- The ineptitude of polynomial-based approximations to represent the conformation tensor profiles, which could be exponential in regions of high deformation rate, or near stagnation points [17].
- The loss of symmetric positive definiteness of the conformation tensor.

Therefore, the numerical reconstruction and extensive study of the phenomenon of elastic turbulence could be impeded by the HWNP.

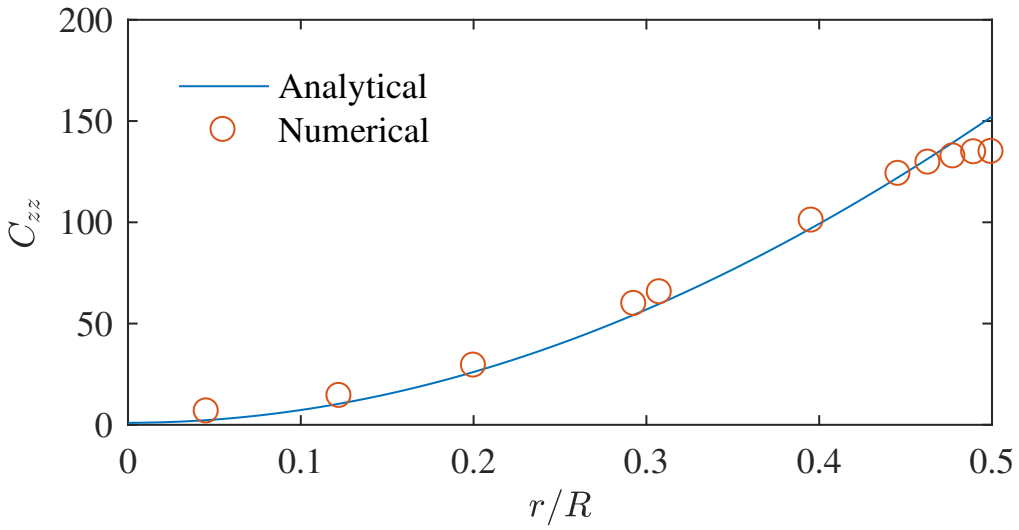

Fig. 3.4: C_{zz} for Re 1 Wi 1.1111

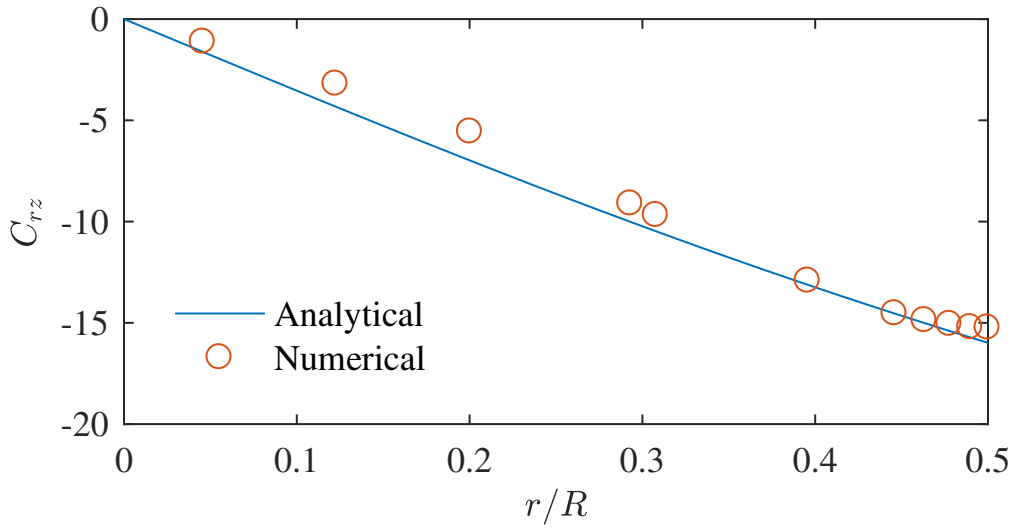

Fig. 3.5: C_{rz} for Re 2 Wi 2.2222

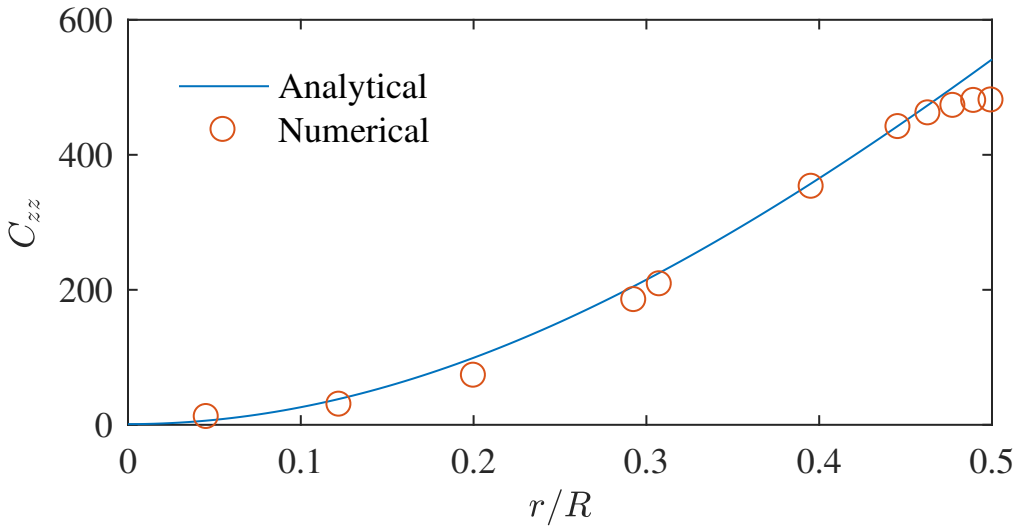

Fig. 3.6: C_{zz} for Re 2 Wi 2.2222

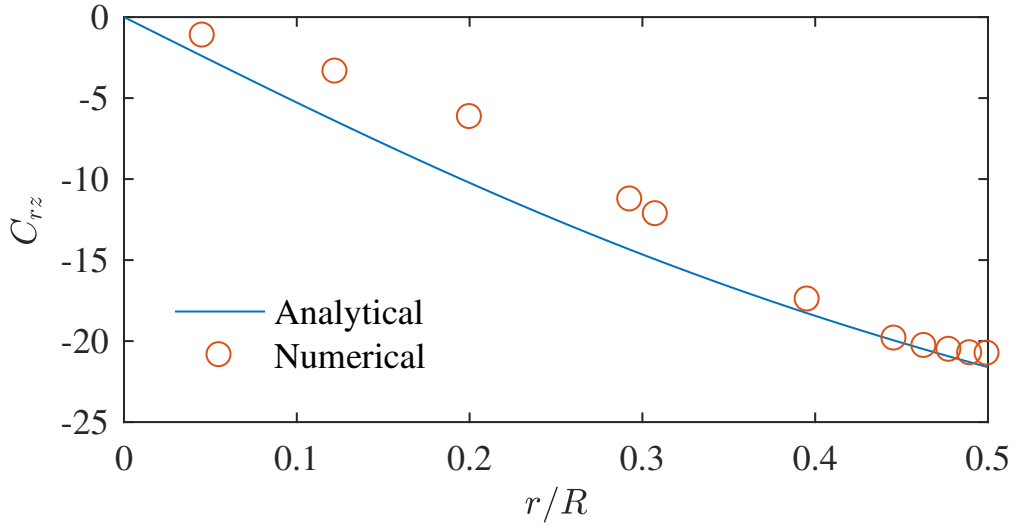

Fig. 3.7: C_{rz} for Re 3 Wi 3.3333

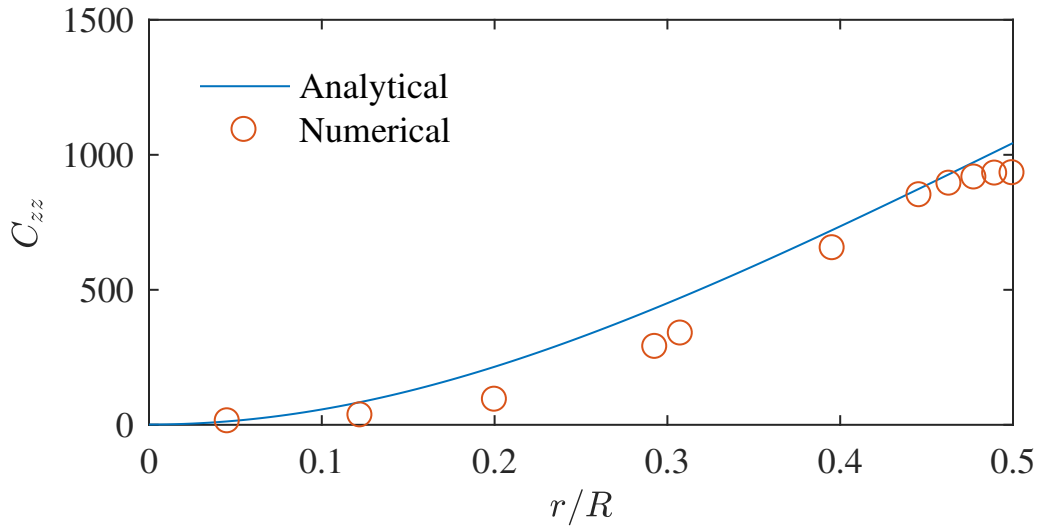

Fig. 3.8: C_{zz} for Re 3 Wi 3.3333

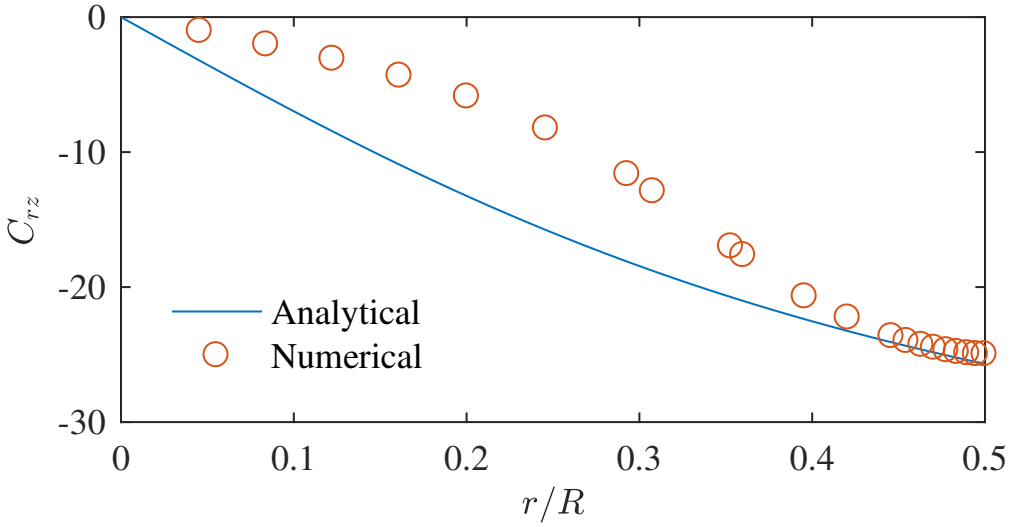

Fig. 3.9: C_{rz} for Re 4 Wi 4.4444

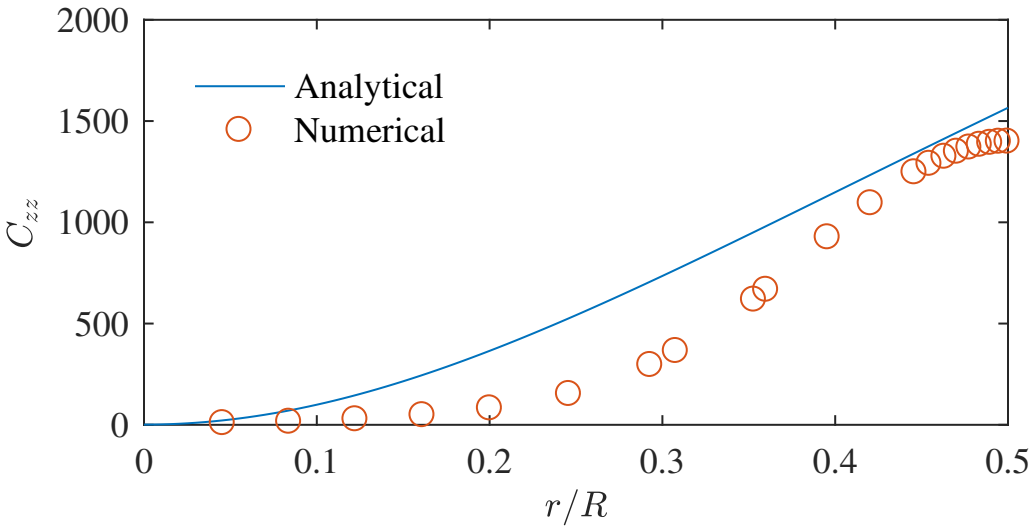

Fig. 3.10: C_{zz} for Re 4 Wi 4.4444

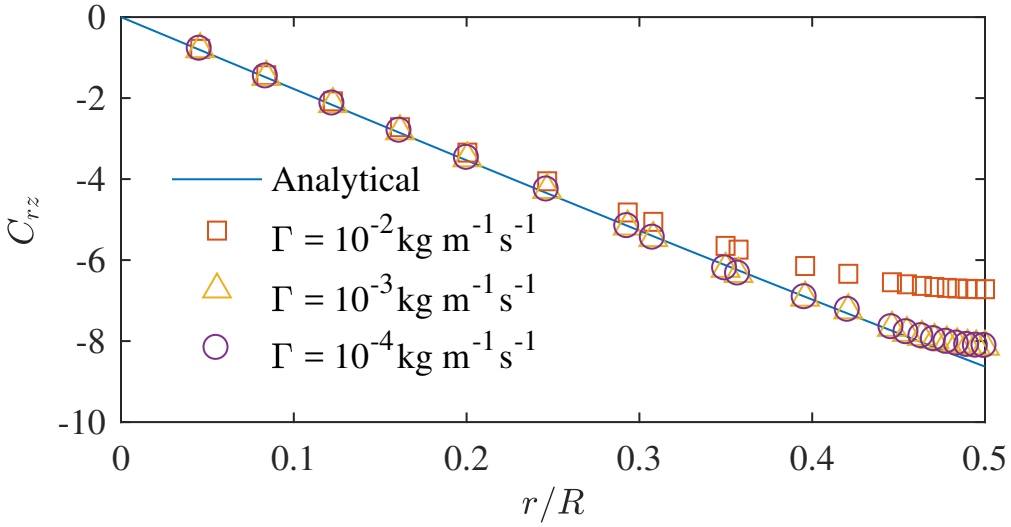

Fig. 3.11: C_{rz} with different added diffusion values for Re 1 Wi 1.1111

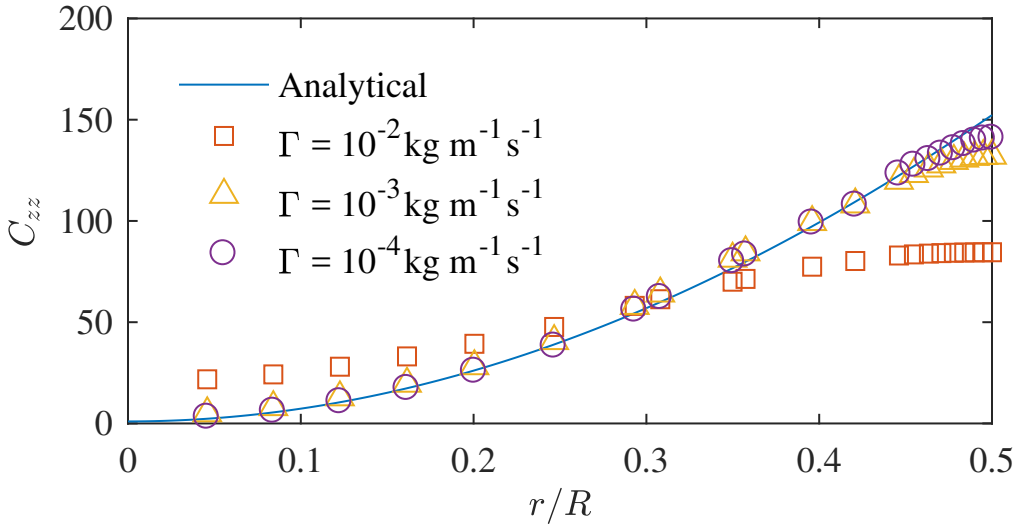

Fig. 3.12: C_{zz} with different added diffusion values for Re 1 Wi 1.1111

4. THE LOG-CONFORMATION REFORMULATION METHOD

The phrase 'High Weissenberg Numerical Problem' (HWNP) was coined to describe the common situation experienced by researchers in which numerical simulations failed beyond some limiting value of the Weissenberg number. The limiting value varies with the flow geometry and the fluid constitutive model of the problem. As it has been mentioned in the previous chapter, it is generally recognized that the HWNP stems from the loss of symmetric positive definiteness property of the conformation tensor and also the inability of a low order polynomial fitting to capture the high gradients of the conformation tensor components.

Many efforts have been paid to deal with the HWNP. Vaithianathan and Collins [47] proposed a decomposition algorithm for the conformation tensor to guarantee symmetric positive definiteness and improve the overall stability of the simulation of viscoelastic fluids at high Weissenberg numbers. Fattal and Kupferman [17] [18] proposed formulating the equations in terms of the logarithm of the conformation tensor, which is called the log-conformation reformulation. This method is a numerical algorithm that preserves the symmetric positive definiteness property of the conformation tensor and also eliminates the deviation that is caused by an improper approximation at a high Weissenberg number. This formulation has been successfully implemented for a flow around a cylinder [1], lid-driven cavity [18], and Poiseuille flow [26] indicating the advantage and validity of using the log-conformation reformulation for solving the HWNP.

4.1 Formulation

Based on the continuum hypothesis and incompressible flow condition, the conservation of mass implies $\boldsymbol{u}$ is divergence free, $div(\boldsymbol{u}) = 0$. When the velocity gradient

is traceless, Fattal and Kupferman [17] showed that $grad(\boldsymbol{u})$ can be decomposed as follows:

$$grad(\boldsymbol{u}) = \boldsymbol{\Omega} + \boldsymbol{B} + \boldsymbol{N}\boldsymbol{C}^{-1}, \tag{4.1}$$

where $\boldsymbol{\Omega}$, $\boldsymbol{N}$ are anti-symmetric matrices, and $\boldsymbol{B}$ is a symmetric and traceless matrix. The are defined as follows:

$$\boldsymbol{\Omega} = \boldsymbol{R} \begin{bmatrix} 0 & \omega_1 & \omega_2 \\ -\omega_1 & 0 & \omega_1 \\ -\omega_2 & -\omega_3 & 0 \end{bmatrix} \boldsymbol{R}^T, \tag{4.2}$$

$$\boldsymbol{B} = \boldsymbol{R} \begin{bmatrix} m_{11} & 0 & 0 \\ 0 & m_{22} & 0 \\ 0 & 0 & m_{33} \end{bmatrix} \boldsymbol{R}^T, \tag{4.3}$$

$$\boldsymbol{N} = \boldsymbol{R} \begin{bmatrix} 0 & n_1 & n_2 \\ -n_1 & 0 & n_3 \\ -n_2 & -n_3 & 0 \end{bmatrix} \boldsymbol{R}^T. \tag{4.4}$$

Using the decomposition from equation (4.1), equation (3.5) can be rewritten as,

$$\frac{D\boldsymbol{C}}{Dt} = \boldsymbol{\Omega}\boldsymbol{C} - \boldsymbol{C}\boldsymbol{\Omega} + 2\boldsymbol{B}\boldsymbol{C} + \frac{1}{\lambda}[\boldsymbol{I} - f(R)\boldsymbol{C}]. \tag{4.5}$$

For the equation (4.5) to be well posed the conformation tensor needs to be a symmetric positive definite matrix, and it is decomposed as,

$$\boldsymbol{C} = \boldsymbol{R}\boldsymbol{\Lambda}\boldsymbol{R}^T. \tag{4.6}$$

where $\boldsymbol{R}$ is an orthogonal matrix composed by the eigen vectors of $\boldsymbol{C}$, and $\boldsymbol{\Lambda}$ is a diagonal matrix in which the diagonal elements are the eigenvalues of $\boldsymbol{C}$ as:

$$\boldsymbol{\Lambda} = \begin{bmatrix} \lambda_1 & 0 & 0 \\ 0 & \lambda_2 & 0 \\ 0 & 0 & \lambda_3 \end{bmatrix}. \tag{4.7}$$

where, λ_1, λ_2 and λ_3 are the three eigenvalues of $\boldsymbol{C}$. A matrix, $\boldsymbol{M}$ is defined for the purpose of calculating $\boldsymbol{\Omega}$, $\boldsymbol{N}$ and $\boldsymbol{B}$ as,

$$\boldsymbol{M} = \boldsymbol{R}^T grad(\boldsymbol{u})\boldsymbol{R} = \begin{bmatrix} m_{11} & m_{12} & m_{13} \\ m_{21} & m_{22} & m_{23} \\ m_{31} & m_{32} & m_{33} \end{bmatrix}. \tag{4.8}$$

Substituting Eqs. (4.1), (4.2), (4.3), (4.4), (4.6), (4.7), it can be determined that $\omega_1 = \frac{\lambda_2 m_{12}+\lambda_1 m_{21}}{\lambda_2-\lambda_1}$, $\omega_2 = \frac{\lambda_3 m_{13}+\lambda_1 m_{31}}{\lambda_3-\lambda_1}$, $\omega_3 = \frac{\lambda_3 m_{23}+\lambda_2 m_{32}}{\lambda_3-\lambda_2}$. Also $n_1 = \frac{m_{12}+m_{21}}{\lambda_2^{-1}-\lambda_1^{-1}}$, $n_2 = \frac{m_{13}+m_{31}}{\lambda_3^{-1}-\lambda_1^{-1}}$, $n_1 = \frac{m_{23}+m_{32}}{\lambda_3^{-1}-\lambda_2^{-1}}$. The logarithm of the dimensionless conformation tensor $\boldsymbol{\phi}$ can be calculated by taking the logarithm of each element in the diagonal matrix [17] as:

$$\boldsymbol{\phi} = log(\boldsymbol{C}) = \boldsymbol{R} log(\boldsymbol{\Lambda})\boldsymbol{R}^T. \tag{4.9}$$

With the definition in the equation (4.9), the decomposed evolution equation (4.5) can be rewritten as follows,

$$\frac{D\boldsymbol{\phi}}{Dt} = \boldsymbol{\Omega\phi} - \boldsymbol{\phi\Omega} + 2\boldsymbol{B} + \boldsymbol{R}[\frac{1}{\lambda}(\boldsymbol{\Lambda}^{-1} - f(R)\boldsymbol{I})]\boldsymbol{R}^T. \tag{4.10}$$

4.2 Calculations

Via LCR approach, the evolution equation in equation (3.5) is replaced by an equivalent evolution equation for the logarithm of the conformation tensor. This is vital in eliminating the deviation between the exponential variation and the polynomial interpolation of the conformation tensor variables. Also, this reformulation ensures SPD property of the conformation tensor. After solving $\boldsymbol{\phi}$ using equation (4.10), the conformation tensor can be updated using equations (4.6), (4.7), (4.8), (4.9). All the equations discussed were implemented in ANSYS-FLUENT using user defined functions. ANSYS-FLUENT is a software written in a C environment and has a limited C compiler. However, this reformulation requires a series of linear algebra operations including the evaluation of eigen values of $\boldsymbol{C}$. In order to achieve this, Visual Studio C compiler has been configured to become accessible from ANSYS-FLUENT and using Linear Algebra PACKage in C called LAPACK, shared libraries were created that could be linked with the rest of the solver. The algorithm is similar to the one shown in Fig. 3.1 except for two intermediate steps involving the conversion of the conformation tensor to its log form and back. The details of the algorithm are given in the flow chart shown in Fig. 4.1.

4.3 Initial and boundary conditions

The natural outflow boundary condition is given at the outlet with the developed boundary condition. No slip velocity boundary conditions and a no-flux boundary condition is imposed on $\boldsymbol{\phi}$, $\frac{\partial \boldsymbol{\phi}}{\partial y} = 0$ are prescribed on the walls. The conformation tensor is initialized to be a unit tensor implying no elastic stress translating to $\boldsymbol{\phi} = \mathbf{0}$. As for the numerical schemes, the conformation tensor equations were descretized by second order accuracy.

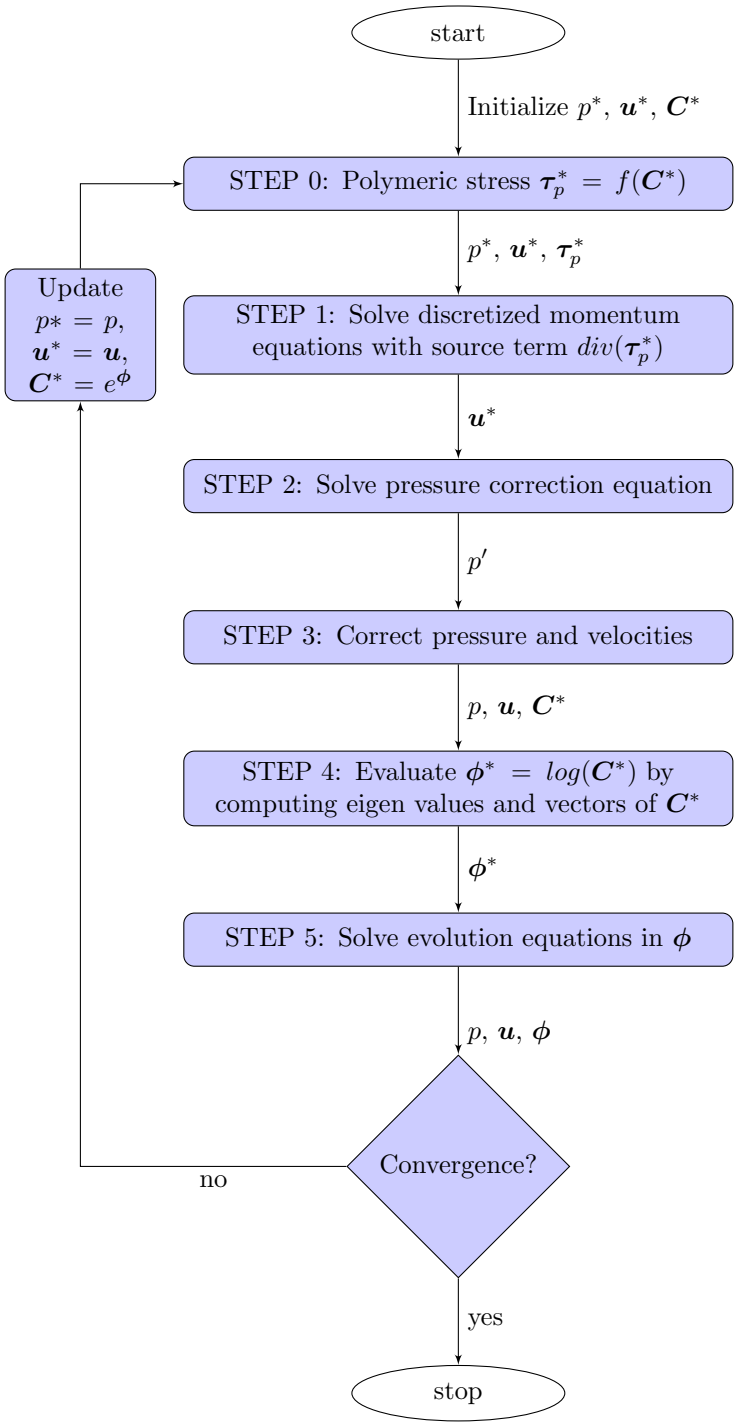

Fig. 4.1: Algorithm with the log-conformation reformulation.

4.4 Results and discussion

The primary task is to validate the LCR solver by simulating flow in a pipe and checking against the analytical solution similar to the procedure discussed in the previous chapter. The momentum conservation equation coupled with the constitutive equation of the log-conformation reformulation are solved to arrive at the solutions. As mentioned previously direct simulation of the evolution equation (3.5) is limited by the fact that cases with $Wi > 4.5$ suffer from convergence issues.

Table 4.1: Simulations with varying Wi with LCR

No.	Re	Wi	Grid nodes	L/D	Fig.
1	1	1.1111	52600	20	4.2, 4.3
2	4	4.4444	52600	20	4.4, 4.5
3	5	5.5555	52600	20	4.6, 4.7
4	8	8.8888	52600	20	4.8, 4.9

Fig. 4.2 and Fig. 4.3 show the comparison of the analytical solution with the numerical results from the log-conformation reformulation of C_{rz} and C_{zz} for the base case of $Wi = 1.1111$ and $Re = 1$. Fig. 4.4 through Fig. 4.9 show the comparison of the analytical solution with the numerical results for different values of Wi and Re, details of which are given in Table 4.1. As one can see, the log-conformation reformulation allows the simulation at higher Wi. It is important to note that without the log-conformation reformulation all simulations with $Wi > 4$ failed to converge. The effect of no-flux boundary condition imposed on $\boldsymbol{\phi}$ manifests in $\boldsymbol{C}$ calculations. An extra diffusion term is added to the evolution equation of $\boldsymbol{\phi}$ to assist convergence. The inclusion of the diffusion term causes much more pronounced

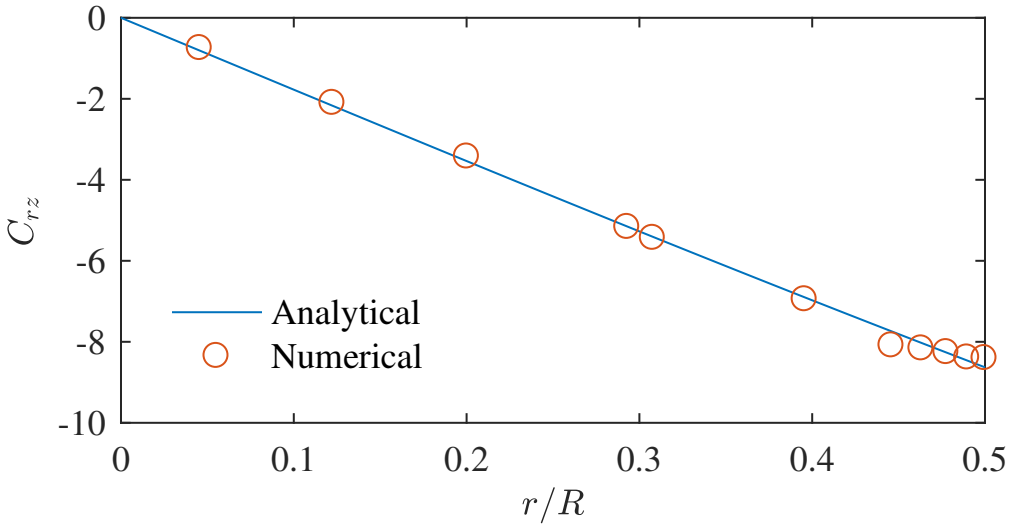

Fig. 4.2: C_{rz} for Re 1 Wi 1.1111 with LCR

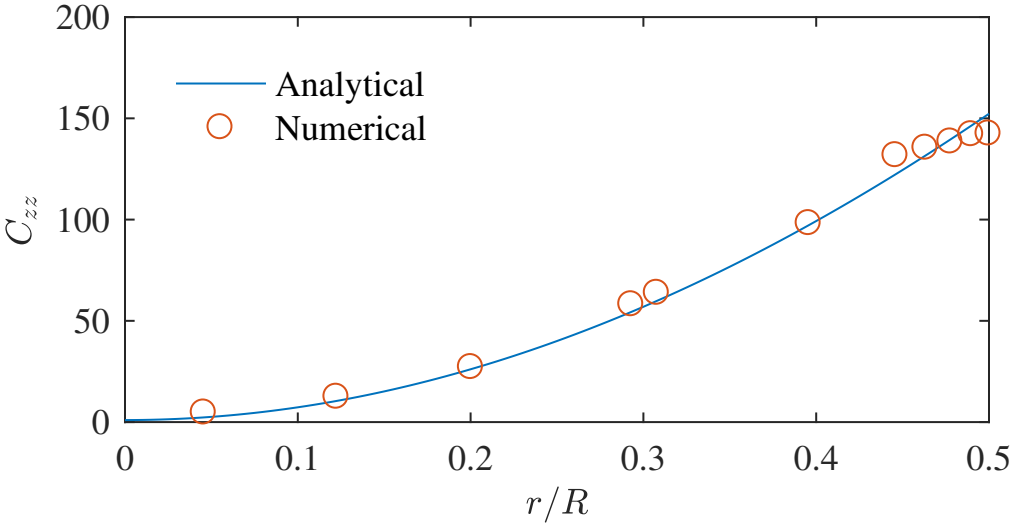

Fig. 4.3: C_{zz} for Re 1 Wi 1.1111 with LCR

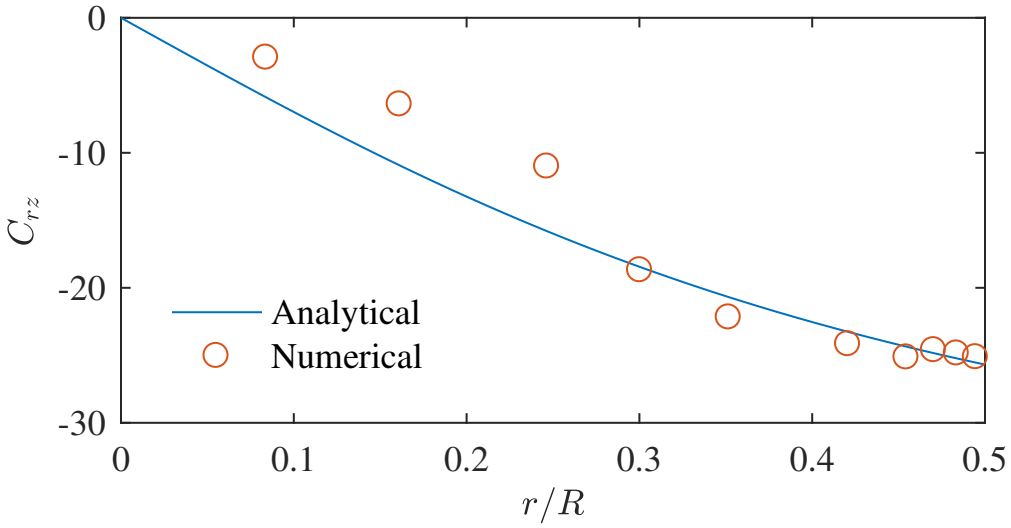

Fig. 4.4: C_{rz} for Re 4 Wi 4.4444 with LCR

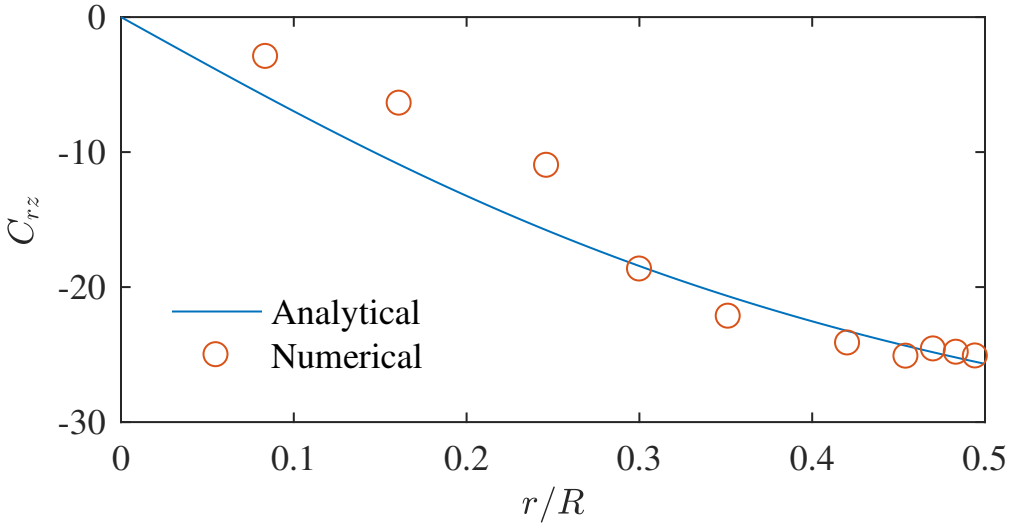

Fig. 4.5: C_{zz} for Re 4 Wi 4.4444 with LCR

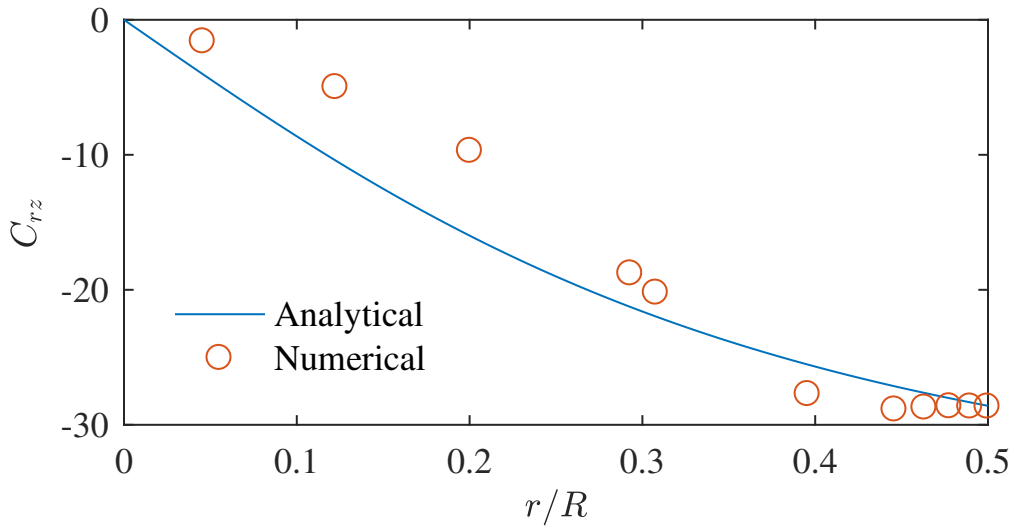

Fig. 4.6: C_{rz} for Re 5 Wi 5.5555 with LCR

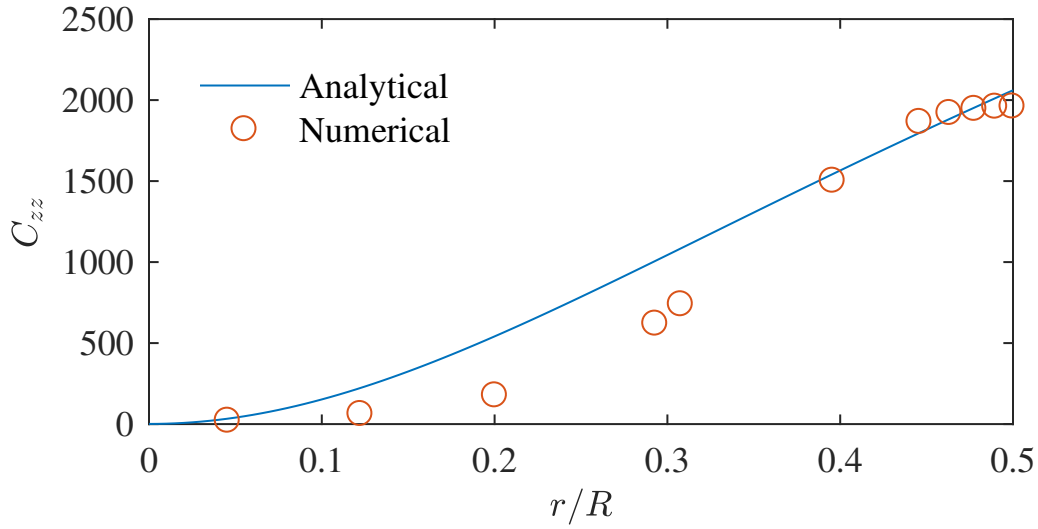

Fig. 4.7: C_{zz} for Re 5 Wi 5.5555 with LCR

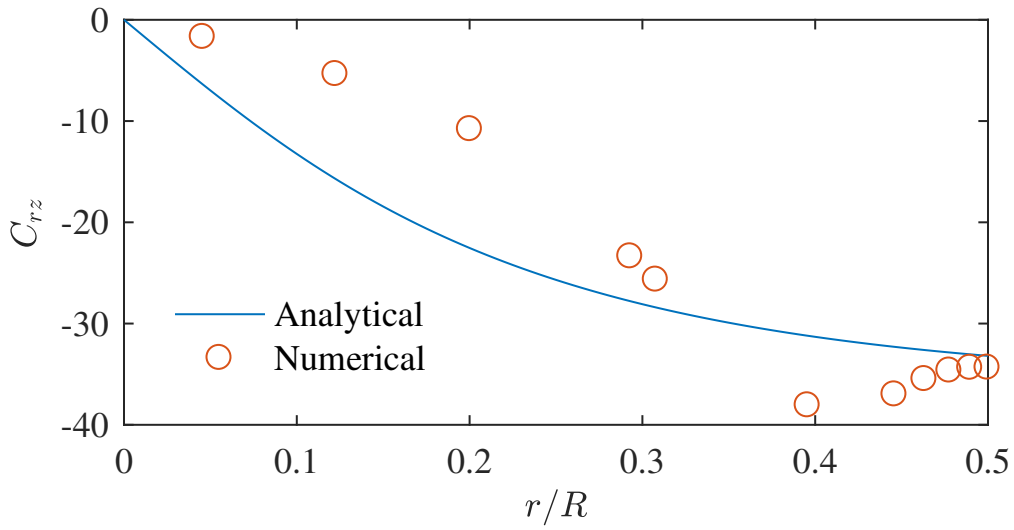

Fig. 4.8: C_{rz} for Re 8 Wi 8.8888 with LCR

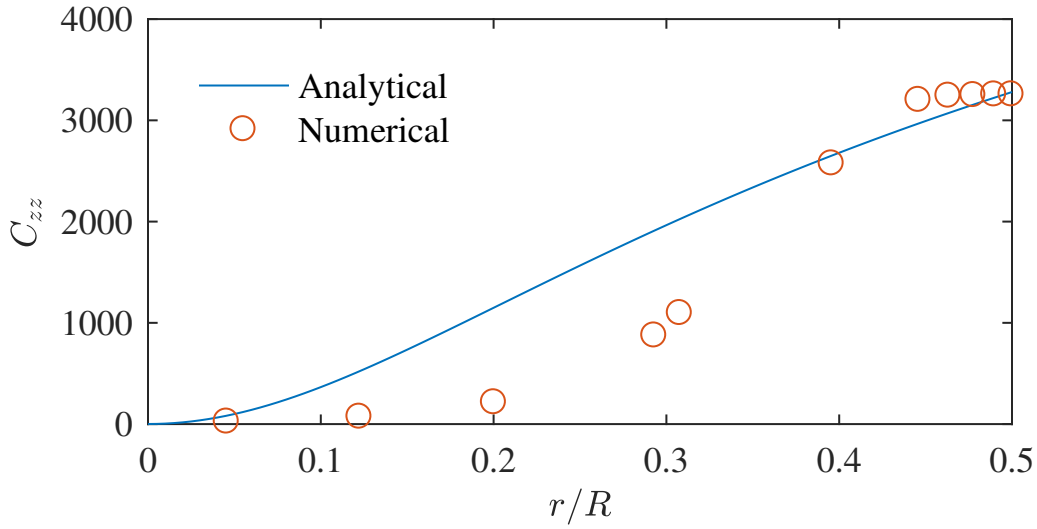

Fig. 4.9: C_{zz} for Re 8 Wi 8.8888 with LCR

disagreement with the analytical solution when compared to the simulations carried out without the log-conformation reformulation. This deviation is caused due to the amplification of the error in $\boldsymbol{\phi}$ via $\boldsymbol{C} = e^{\boldsymbol{\phi}}$.

In conclusion, this work has presented a new, improved solver for the simulation of flows of viscoelastic fluids governed by the FENE-P constitutive model by adoption of the technique proposed by Fattal and Kupferman [17]. The resulting method allows one to obtain globally stable solutions, and has been validated in the benchmark steady state pipe flow problem for relatively higher Weissenberg numbers. The results in this chapter also demonstrate that the LCR method better mitigates against the HWNP and delays its onset.

5. NUMERICAL SIMULATION OF CONFINED SWIRLING FLOW OF FENE-P FLUIDS

Swirling flows are ubiquitous both in nature and technology. Large rotating flows are found both in the atmosphere and the oceans, whereas industrial applications of swirling flows are found in viscometry, in lubrication, turbines, centrifugal pumps, among others. A special case for such a flow is the flow between two coaxial rotating plates or disks.

The flow of an incompressible fluid by an infinite rotating disk in an unbounded fluid domain is a classical problem in fluid mechanics. Von Karman [29] was the first to study this problem for Newtonian fluids by using an elegant similarity transformation, that transformed the Navier-Stokes equations to a set of Ordinary Differential Equations. There is not extensive research available involving a single disk rotating problem for non- Newtonian fluids. Mitschka [36] showed that Von-Karman's similarity solution could be extended to power-law fluids. Ariel [2] showed that a similarity solution does exist for a particular class of viscoelastic fluids. In the case of polymeric fluids that are viscoelastic, rotating disk flows in a confined domain assume much more practical importance.

The first attempt at investigating the effects of viscoelasticity on the flow behavior of confined swirling flows of viscoelastic fluids was made by Stokes et al. [44]. They observed some unsteady flow patterns by using polyacrylamide Borger fluid [9] with relatively high viscosity, which minimized the inertial effects in the flow. By picking a polymer solution with a high viscosity, they inferred that the observed phenomena are caused by the purely elastic nature of the fluid. On the other hand, when the fluid used is a low viscosity dilute polymer solution such that inertial effects could

not be ignored anymore, they observed that the stress hike on the rotating plate that is attributed to turbulent drag is delayed. In some extreme cases, the stress hike is even suppressed due to the presence of the polymer in the solution when compared to a Newtonian solution of comparable viscosity. By observing a different range of fluids, they reported that swirling flows became unstable for both inertia dominated flows [high Re low Wi] and elasticity dominated flows [low Re high Wi]. Thus, they found an extremely strong correlation between the ratio of Wi/Re and the type of instability developed in the flow. This ratio is referred to as the elasticity number El. So, in short, the flow is dominated by elastic effects when $El \geq 1$, and if $El < 1$ the flow becomes inertia dominated. As discussed earlier, the numerical investigation of viscoelastic fluids in a confined swirling flow poses a tall challenge of dealing with high Weissenberg number numerical problem.

The flow between two rotating plates is of considerable importance and forms the basis for rheological measurements of viscosity and normal stresses in both Newtonian and non-Newtonian liquids. Some extrusion processes of polymers also employ such flow geometries. The simplest case of the flow geometry consists of two coaxial disks, separated by a small distance. In a typical rheological measurement, fluid samples are contained in the narrow gap and subjected to the rotation of the upper plate at a constant angular velocity while the bottom plate is kept fixed. This experimental set-up is of particular importance since it was also used by Groisman and Steinberg [21] to discover this anomalous phenomenon of elastic turbulence.

5.1 Groisman and Steinberg's experiment

The focal point of this chapter is the findings of Groisman and Steinberg [21] [23]. They used a dilute solution of a high molecular weight polyacrylamide in viscous sugar syrup. When they conducted the experiment at vanishingly low $Re < 1$

with a gradual increase in Wi, they found a strong tendency for the development of turbulent behavior. They quantitatively analyzed the experiment by measuring the shear stress on the top plate and normalized it with the shear stress in the corresponding Newtonian case that the flow does not have the polymer.

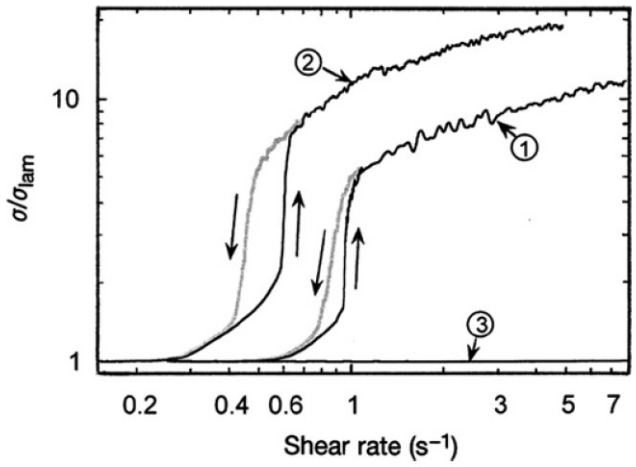

Fig. 5.1: Normalized shear stress on the top plate in the top plate driven swirlflow experiment by Groisman and Steinberg [21] is plotted on the y - axis and shear rate on x - axis. Data from 3 different cases is shown: the curves labeled 1 and 2 are flows with $D/R = .263$ and $D/R = .526$ respectively, curve 3 is the response of the pure solvent without polymers.

In Fig. 5.1 the data sets labeled 1 and 2 correspond to different D/R ratio, where D is the depth and R the radius of the geometry. The data set labeled 3 at the bottom of the plot represents the pure solvent. For the curves labeled 1 and 2, the normalized stress appears to increase with the rotation rate linearly. Upon further increase in shear rate, the curves spike up sharply. This is the regime that is being referred to as elastic turbulence. Arrows indicate that the this transition to turbulence is hysteretic; when the rotation is decreased slowly, the emerged turbulence disappears at a lower

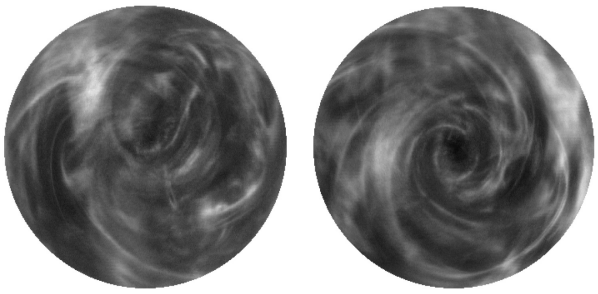

Fig. 5.2: Two snapshots of the turbulent flow in the experiment at $Wi = 13$ and $Re = 0.7$ in the top plate driven swirlflow experiment by Groisman and Steinberg [21].

rotation rate. Visualization for the experiment was carried out by feeding the fluids with a fluorescent dye. Fig 5.2 shows the snapshots suggesting the emergence of chaotic flow that is captured by the spatial and temporal spectra shown in Fig 5.3. This broad range of spatial and temporal frequencies is reflective of fluid motion's spatial and temporal scales. Groisman and Steinberg [21] reported that the power, P of fluctations is fitted by a power law, $P \approx f^{-3.5}$ over about a decade in frequencies, f as shown in Fig. 5.3. Hence, this viscoelastic phenomenon is accompanied by two most common features that are usually associated with turbulence:

- An increase in the flow resistance.
- Excitation of a broad range of spatial and temporal scales.

5.2 Numerical simulation

In an attempt to recreate the experiment that lead to the discovery of elastic turbulence, an exact geometric domain has been created. This flow system consists of a fixed enclosed circular cylinder of Radius $R_o = 43.6\ mm$ and depth $D = 10\ mm$ with a lid whose radius $R_i = 38\ mm$ is smaller than that of the cylinder the liquid is

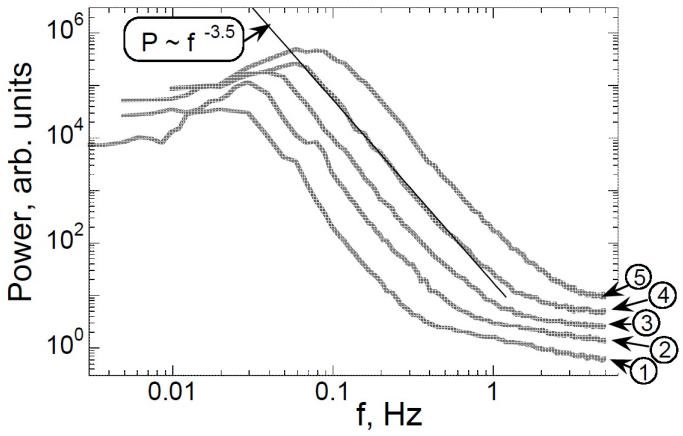

Fig. 5.3: Power spectra of velocity fluctuations taken at different shear rates $\dot{\gamma} = 1.25, 1.85, 2.7, 4.0, \& \ 5.9 \ s^{-1}$ reported by Groisman and Steinberg [21]

contained in. This lid is set to rotate with a constant angular velocity Ω. The liquid properties chosen for the numerical simulation are exactly the same as those in the experiment carried out by Groisman and Steinberg [21]. The density of the fluid is $\rho = 4240 \ kg/m^3$. The dynamic solvent(of the polymer) viscosity is $\mu_s = 0.324 \ Pa\text{-}s$, and the polymer added in the experiment is polyacrylamide at a concentration of 80 *ppm* by weight. The total viscosity of the solution is $\mu = 0.424 \ Pa\text{-}s$. The relaxation time, λ was estimated to be around 3.4 s. The retardation ratio is defined as $\beta = \mu_s/\mu$

Before moving on to the details of the problem formulation, it is necessary to introduce the relevant non dimensional numbers and their definitions with respect to current numerical simulations. The characteristic shear for the given flow is $\Omega R_i/D$, The Weissenberg number which is defined as the ratio between relaxation time scale and shear time scale is given by $Wi = \lambda \Omega R_i/D$. The Reynolds number is defined as $Re = (\rho \Omega R_i D)/\mu$. For a swirling flow such as this, there are two significant shear rates in consideration, $\dot{\gamma}_{\theta r}$ and $\dot{\gamma}_{\theta z}$. Since we have picked a geometry in which the

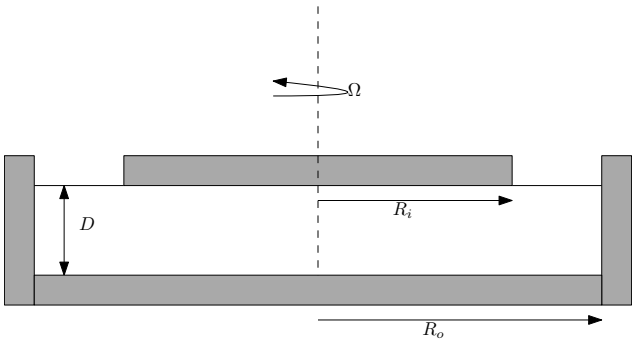

Fig. 5.4: Schematic of the rotating plate experiment

radius R_i is greater than depth D, it is assumed that the characteristic shear rate $\dot{\gamma}_{\theta z} = \Omega R_i/D$ is the larger of the two. The elasticity number which is defined as $El = Wi/Re$ for the current consideration turns out to be $El = \lambda\mu/\rho D^2$.

5.3 Problem formulation

The objective is to simulate the flow of an isothermal, incompressible viscoelastic fluid in a fixed closed cylinder at low Reynolds numbers and high Weissenberg numbers. As mentioned earlier, the purpose behind keep the Reynolds number low is to reduce the inertial effects in the flow. The domain is assumed to be completely filled with fluid and the lid is impulsively set to rotate with a constant angular velocity Ω. The geometry of the flow is sketched in Fig. 5.4.

5.4 Governing equations

Since, the viscoelastic fluid is assumed to be incompressible, the mass conservationimplies equation (5.1).

$$div(\boldsymbol{u}) = 0 \tag{5.1}$$

Like discussed previously, FENE-P model shall remain the choice for modeling viscoelasticity of the polymer solution. The momentum equation is given by equation 5.2.

$$\rho\frac{D\boldsymbol{u}}{Dt} = -\frac{\partial p}{\partial \boldsymbol{x}} + div\left(\mu_s\frac{\partial \boldsymbol{u}}{\partial \boldsymbol{x}}\right) + div(\boldsymbol{\tau}^p) \tag{5.2}$$

The evolution equation of the conformation tensor is given by equation 5.3.

$$\frac{D\boldsymbol{C}}{Dt} = \left(\frac{\partial \boldsymbol{u}}{\partial \boldsymbol{x}}\right)^T\boldsymbol{C} + \boldsymbol{C}\left(\frac{\partial \boldsymbol{u}}{\partial \boldsymbol{x}}\right) - \frac{1}{\lambda}[f(R)\boldsymbol{C} - \boldsymbol{I}] \tag{5.3}$$

Also the polymeric stress $\boldsymbol{\tau}^P$ is given by the following equation:

$$\boldsymbol{\tau}^p = \frac{\mu_p}{\lambda}[f(R)\boldsymbol{C} - \boldsymbol{I}] \tag{5.4}$$

$f(R) = \frac{L_0^2-3}{L_0^2-R^2}$ where R^2 is the trace of $\boldsymbol{C}$

The momentum equation that is given in equation 5.2 follows from the assumption that stress in a viscoelastic fluid can be linearly split into the sum of solvent stress (which is Newtonian) and the additional polymeric stress. The polymeric stress can be obtained from equation (5.4) which is dependent on the conformation tensor $\boldsymbol{C}$. The evolution equations as discussed in section. 3.3 can be solved using the user-defined scalar functionality of ANSYS-FLUENT. Since this simulation of swirling flow is expected to have a high shear resulting in a high Weissenberg number, the simulation is expected to suffer from the so-called 'high Weissenberg number problem.' The 3D version of the log-conformation reformulation has been implemented by writing the appropriate user-defined functions in C-language. Once the conformation tensor is obtained, the polymeric stresses are determined from equation (5.4).

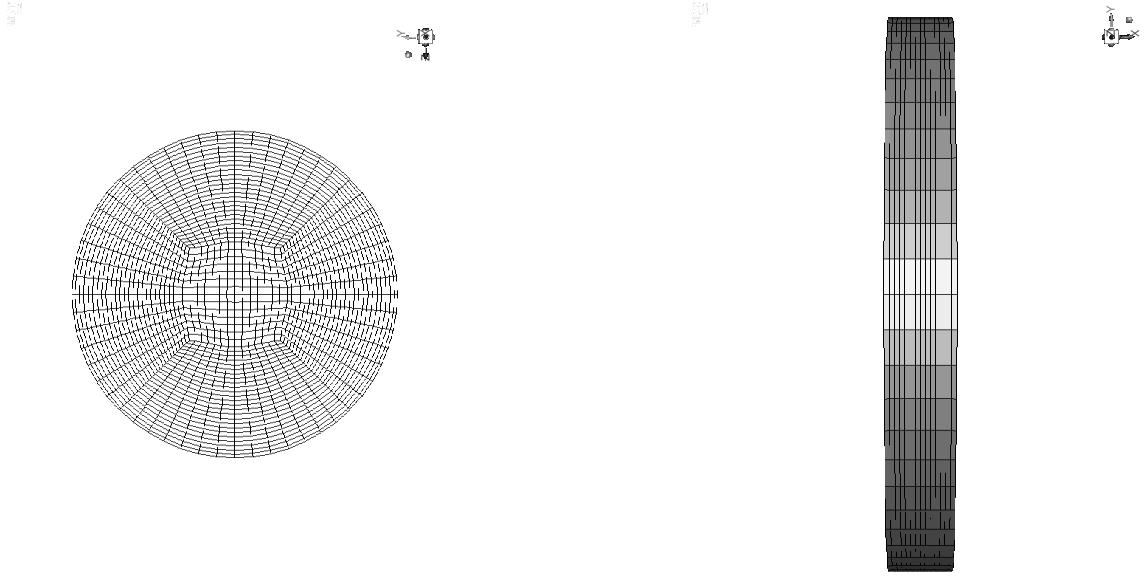

(a) Top view (b) Side view

Fig. 5.5: Mesh used for the simulation

5.5 Boundary conditions and mesh

The mesh was created using an exclusive CFD meshing software called Ansys ICEM. The mesh used for simulation has 1596×14 cells. The domain has been divided into 14 cross sections parallel to the rotating disk. Each such section has 1596 elements, making it a total of 22344 cells. The total volume of the domain is 50240 mm^3. The minimum and maximum volume of the cells are 1.123267 mm^3 and 3.955476 mm^3 respectively. The time step for the simulation was chosen to be $0.01s$. The boundary Conditions of the simulation are as follows:

- Bottom disk: no slip condition and is at rest.
- Side Wall: no slip condition and is at rest.
- The top disk has an inner disk of $R_i = 38\ mm$, which is the lid that is impul-

sively set to rotate at constant angular velocity.

- Initial condition: the fluid is assumed to be at rest at the beginning of the simulation.

Note that a no-flux boundary condition has been imposed on the conformation tensor components.

5.6 Results and analysis

The two most common features that are associated with the chaotic motion of fluid particles are an increase in resistance to the flow and excitation of several time and length scales. The motivation behind the simulation is to capture both the mentioned features qualitatively and numerically. To estimate the increase in flow resistance, the average shear stress has been computed from calculating the torque on the top plate as shown in the equation below.

$$\tau_{avg} \int_0^{R_i} r(2\pi r)dr = \int_0^{R_i} \tau_{z\theta} r(2\pi r)dr \tag{5.5}$$

$\tau_{z\theta}$ is the wall shear stress. Quantifying the excited time scales will constitute the latter part of this chapter.

Since the phenomenon of elastic turbulence occurs at a relatively high Weissenberg number, it is necessary to determine the range that will allow converging solutions before the onset of the high Weissenberg number numerical problem. Although the problem has been tackled to a large extent by the log-conformation tensor reformulation technique, it is important to ascertain the maximum possible Weissenberg number that the developed code can simulate for the target geometry. This is achieved by carrying out a series of simulations with varying Wi, the details of which are listed in the Table 5.1. The Wi is varied by varying the angular velocity

of the upper plate. For every simulation run, a corresponding Newtonian case has been run for comparison. The calculated value of shear stress is expected to reach a steady-state since the lid is set to rotate at a constant angular velocity.

Table 5.1: List of parameters for the simulations performed with a fixed Ω

No.	$\Omega(s^{-1})$	$\dot{\gamma}(s^{-1})$	Re	Wi	$\tau(Pa)$	$\tau_N(Pa)$
1	0.263158	1	1	3.4	0.39968	0.42355
2	0.315789	1.2	1.2	4.08	0.47968	0.52139
3	0.368421	1.4	1.4	4.76	0.55971	0.62455
4	0.421053	1.6	1.6	5.44	0.63978	0.73205
5	0.473684	1.8	1.8	6.12	0.71990	0.84168
6	0.526316	2	2	6.8	0.80007	0.95337
7	0.578947	2.2	2.2	7.48	0.88029	1.06887
8	0.631579	2.4	2.4	8.16	0.96057	1.18803
9	0.684211	2.6	2.6	8.84	1.04092	1.31188
10	0.736842	2.8	2.8	9.52	1.12134	1.43969
11	0.789474	3	3	10.2	1.20183	1.57072
12	0.842105	3.2	3.2	10.88	1.28241	1.69776
13	0.894737	3.4	3.4	11.56	1.36307	1.81277
14	0.947368	3.6	3.6	12.24	1.44388	1.98169
15	1	3.8	3.8	12.92	1.52468	2.12174
16	1.052632	4	4	13.6	1.60563	2.27873
17	1.473684	5.6	5.6	19.04	2.2578	3.68005
18	1.763158	6.7	6.7	22.78	2.7691	4.68401

Fig. 5.6 shows the plot of average shear stress, normalized with the corresponding average Newtonian shear stress plotted against the respective shear rate. It is interesting to note that there is a linear trend to this plot. This linear trend continues to exist till a shear rate value of $\dot{\gamma} \approx 7s^{-1}$. Beyond this range the solution begins to diverge.

Row 17 and row 18 from Table 5.1 correspond to shear rate values of $\dot{\gamma} = 5.6s^{-1}$

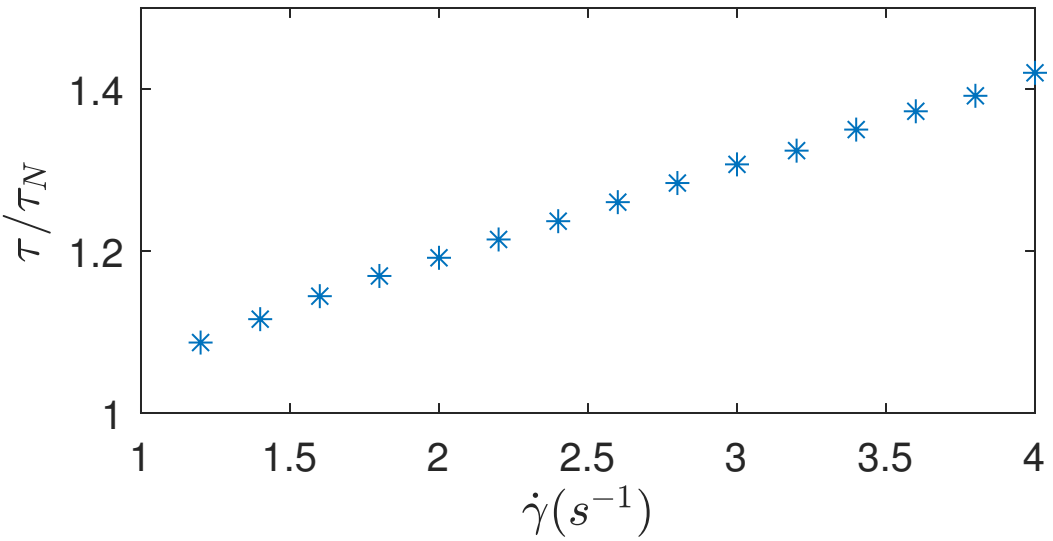

Fig. 5.6: Normalized steady state shear stress values with varying shear rate

and $\dot{\gamma} = 6.7s^{-1}$ respectively. These two shear rates are at the edge of the simulation limit of the solver and have been chosen due to the development of interesting features. Fig. 5.9 shows the comparison of the evolution of the shear stress values between viscoelastic and Newtonian simulation at $\dot{\gamma} = 5.6s^{-1}$. The normalized stress value at this shear rate was found to be 1.63. Fig. 5.7a and Fig. 5.7b show contours of $tr(\boldsymbol{C})$, from top view and side view respectively. This $tr(\boldsymbol{C})$ which represents the measure of average extension of the polymers molecules. An upper limit of $L_0^2 = 10,000$ has been imposed on $tr(\boldsymbol{C})$ in the FENE-P model used for the simulation. Since, the rotating lid is smaller than the fluid containing cylinder, it is reasonable to expect that the maximum $tr(\boldsymbol{C})$ occurs at the edge of the lid, where highest velocity gradients occur. Fig. 5.7a and Fig. 5.7b justify this expectation. The steep gradients of the polymeric stress at the edge of the rotating disk could be resolved with the help of log-conformation reformulation. A closer look at the average shear stress calculated versus time plot suggests the emergence of fluctuations in the flow as shown in Fig. 5.10. These fluctuations appear to have a wide range of

time scales. The average stress is converted to the frequency-domain using the FFT functionality in Matlab to identify the frequency components in the flow, as shown in Fig. 5.11. The frequency-domain plot in Fig. 5.10 appears to suggest a strong periodic behavior due to a dominant frequency, which is reflected in the frequency domain plots made.

Fig. 5.14 shows the comparison of the evolution of the shear stress values between viscoelastic and Newtonian simulation at $\dot{\gamma} = 6.7s^{-1}$. It is important to note that this simulation case is at the edge of the shear rate range in which the simulations can be performed with converging solutions. Fig. 5.14 shows the comparison of the evolution of the shear stress values between viscoelastic and Newtonian simulation at $\dot{\gamma} = 6.7s^{-1}$. Fig. 5.14 shows the emergence of a distinct oscillatory behavior in the flow. This apparent oscillatory behavior continues with time. The time-averaged average shear stress value, however, did not seem to change at 4.68401 Pa, resulting in a normalized average shear stress value of 1.7. Fig. 5.12a and Fig. 5.12b show contours of $tr(\boldsymbol{C})$, from top view and side view respectively. As pointed out in the previous case, steep gradients in the $tr(\boldsymbol{C})$ have been observed. A closer look at the emerged oscillations suggests the existence of fluctuations of a wide range of time scales, as shown in Fig. 5.15. The frequency-domain plot in Fig. 5.15, like in the previous case, suggests a strong periodic behavior with a dominant frequency.

A comparison of frequency-domain spectral density plots of the average shear stress for the two cases is given in Fig. 5.17. The dominant frequency of the flow with $\dot{\gamma} = 5.6s^{-1}$ is close to 0.05 Hz (red line), whereas the dominant frequency of the flow with $\dot{\gamma} = 6.7s^{-1}$ is close to 0.1 Hz (blue line). Both cases show the existence of several low-amplitude, high-frequency time scales that are excited. Fig. 5.17 can be compared to the spectral density plot provided by Groisman and Steinberg [21] given in Fig. 5.3. It is important to note that the y-axis in Fig. 5.3 is the power spectra of

the brightness profiles of the light reflecting particles used in the original experiment conducted by Groisman and Steinberg [21], marked as arbitrary units. A direct comparison can not be made quantitatively; however, the frequency scale seems to be in good agreement with the experimental results. Beyond the dominant frequency, it is observed that there exists a region of a gradual decrease in the amplitude. This observation is consistent with the results reported by Groisman and Steinberg [21].

The oscillatory behavior is most likely caused due to the origin of elastic waves throughout the flow geometry of the viscoelastic fluid. An "elastic wave" is a mechanical disturbance that propagates through a material, causing oscillations of the fluid particles of that material about their equilibrium positions. The wave speed of an elastic wave in an elastic medium can be determined by the relationship $\sqrt{E/\rho}$, where E is the elastic modulus, and ρ is the density of the solution. Fig. 5.17 suggests the existence of elastic waves of different wave speeds throughout the fluid domain. Through the simulations, it has been observed that a strong elastic wave originated at the edge of the rotating top plate. It is suspected that the dominant frequency corresponds to the elastic wave originating at the edge. For linearly elastic materials, the elastic modulus E of the viscoelastic medium depends on the polymer viscosity μ_p and the relaxation time constant λ. However, in reality, the elastic modulus is found to increase with an increase in the magnitude of the stretch of the polymer. The FENE-P model has been employed to capture the non-linear effect of the polymer solution numerically. From the point of view of the FENE-P model, the value of the Peterlin function $f(R)$ increases with an increase of $tr(C)$. $tr(C)$, as discussed in earlier chapters, can be viewed as a measure of the elastic stretch of the elastic component of the fluid. The large velocity gradient at the edge of the rotating plate causes the maximum value of $tr(C)$, and a maximum value of $f(R)$ consequently.

In the FENE-P model, the polymer viscosity μ_p is replaced by $f(R)\mu_p$. So, an increase in the effective elastic modulus and an increase in the wave speed of the elastic waves formed can be attributed to the increase in the value of $f(R)$. As pointed out earlier, the maximum value of $tr(C)$ and, as a consequence, maximum wave-speed is found to occur at the edge of the rotating disk due to the formation of steep gradients of velocity. Similarly, between the two cases that were simulated ($\dot{\gamma} = 5.6\ s^{-1}$ and $\dot{\gamma} = 6.7\ s^{-1}$), a higher shear rate corresponded to a higher wave speed, resulting in an increase in the dominant frequency as shown in Fig. 5.17. This line of thought could also be used to explain the spectral density plot provided by Groisman and Steinberg [21] given in Fig. 5.3.

All the simulation cases performed up to this point have been carried out at a constant rotation rate. In the original experiment, Groisman and Steinberg [21], the rotation rate was gradually increased, leading to a sudden, drastic increase in the measured stress on the top plate. Numerically however, although an increase of calculated average stress on the top plate was observed, it is essential to explore the effect of a gradual increase in the rotation rate. To this cause, a case with the shear rate varying with time t as $\dot{\gamma} = .0210t$ has been performed. Similar to the previous cases, a simulation of the corresponding equivalent Newtonian case has been carried out as well.

A comparison of the shear stress with time has been shown in Fig. 5.18. A plot of the corresponding normalized shear stress is shown in Fig. 5.19. For very low shear rates, the average shear stresses calculated from the viscoelastic and Newtonian simulations tend to be close to each other; this is reflected in Fig. 5.19. For shear rate values of less than 1, the normalized average shear stress tends to be close to 1. In the next range where the shear rate is between 1 s^{-1} and 4 s^{-1}, the normalized average shear stress shows a linear trend. This is consistent with our observation from

Fig. 5.6. Beyond $\dot{\gamma} \approx 7s^{-1}$, an intense oscillatory behavior is observed. A dramatic increase in the normalized average shear stress value begins to develop. The solution suffers from divergence quickly after this transition. A possible solution to the issue of divergence that occurs beyond $\dot{\gamma} \approx 7s^{-1}$ is using a finer grid and decreasing the time step. As it was pointed out earlier, steep gradients of the conformation tensor develop at the edge of the rotating lid, giving rise to steep gradients of polymeric stresses.

In conclusion, the two primary features, namely, an increase in stress and emergence of fluctuations of different time scales, as reported by Groisman and Steinberg [21], have been successfully reproduced through numerical simulations. The flow behavior observed via numerical simulations when the inertial forces are negligibly small, suggests that the above-mentioned features were caused by a mechanism associated only with the elasticity of the fluid. Though an overall increase in normalized average stress was observed numerically, the original experiment reported a much higher growth.

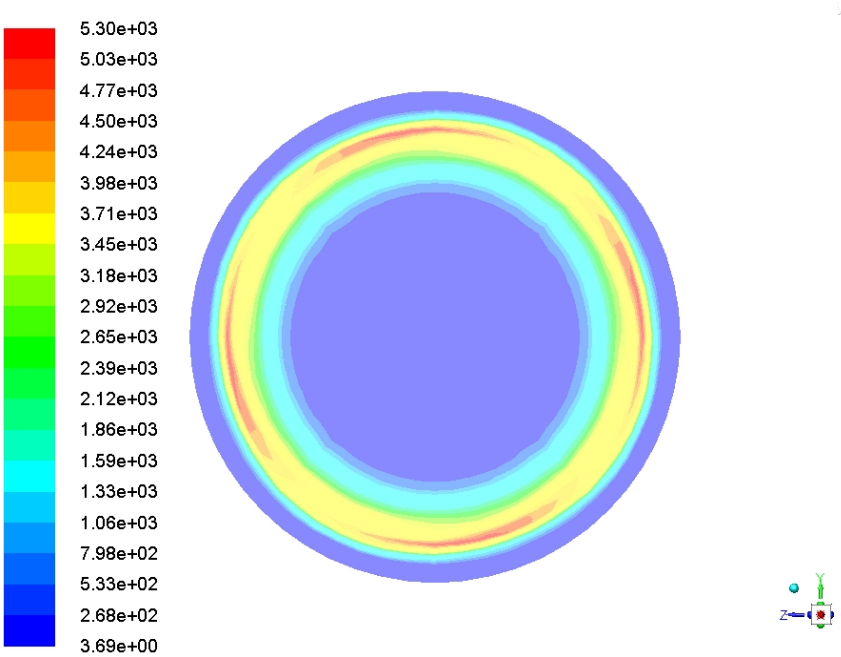

(a) Top view

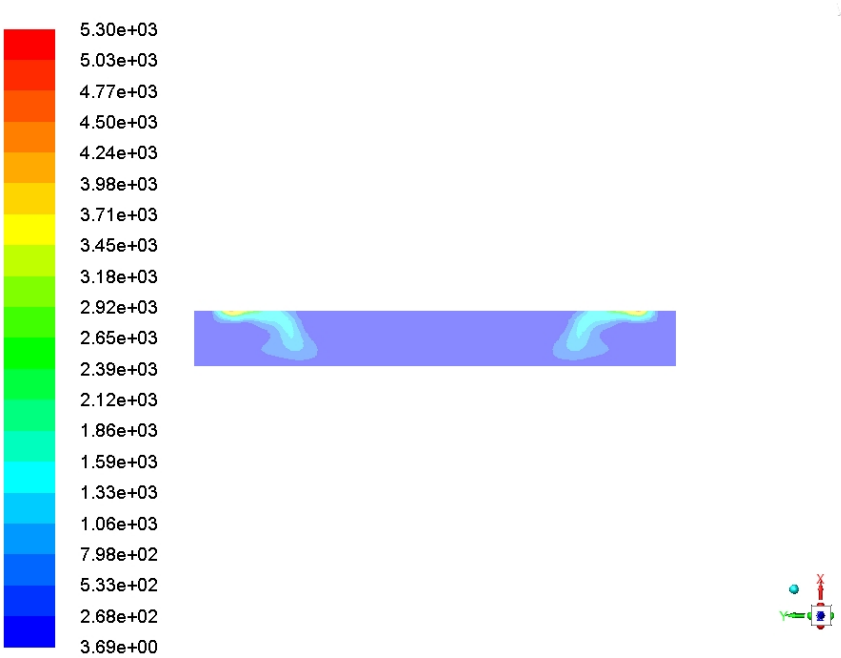

(b) Side view

Fig. 5.7: Contour plot of $tr(\boldsymbol{C})$ at $\dot{\gamma} = 5.6s^{-1}$

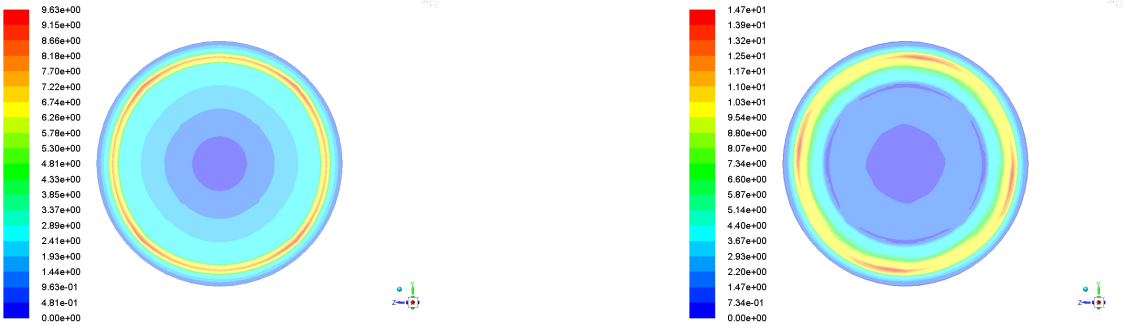

(a) Newtonian (b) Viscoelastic

Fig. 5.8: Contour plot of shear stress at $\dot{\gamma} = 5.6s^{-1}$

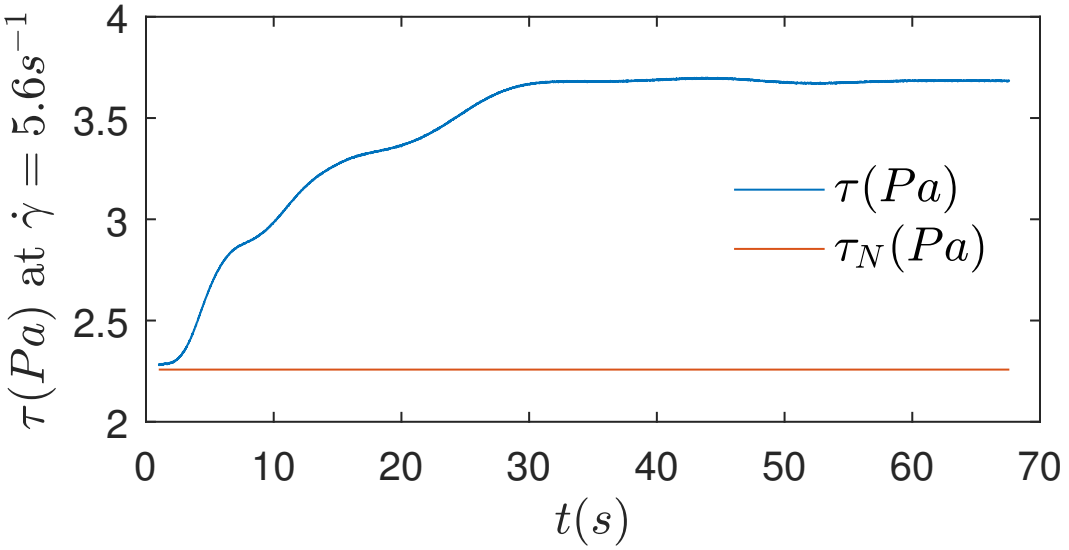

Fig. 5.9: Comparison with the corresponding Newtonian avg stress at $\dot{\gamma} = 5.6s^{-1}$

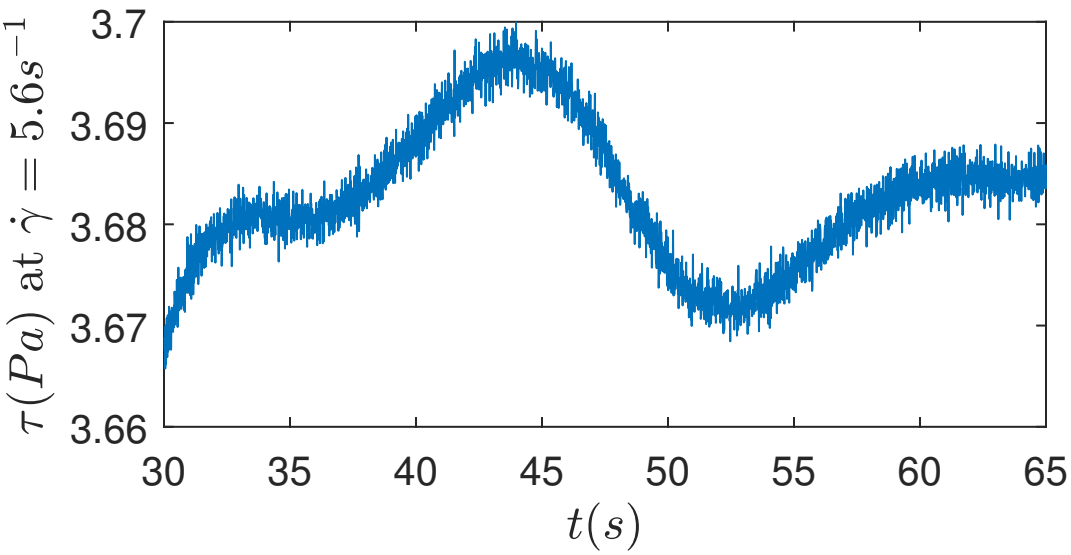

Fig. 5.10: A closer look of τ_{avg} at $\dot{\gamma} = 5.6s^{-1}$

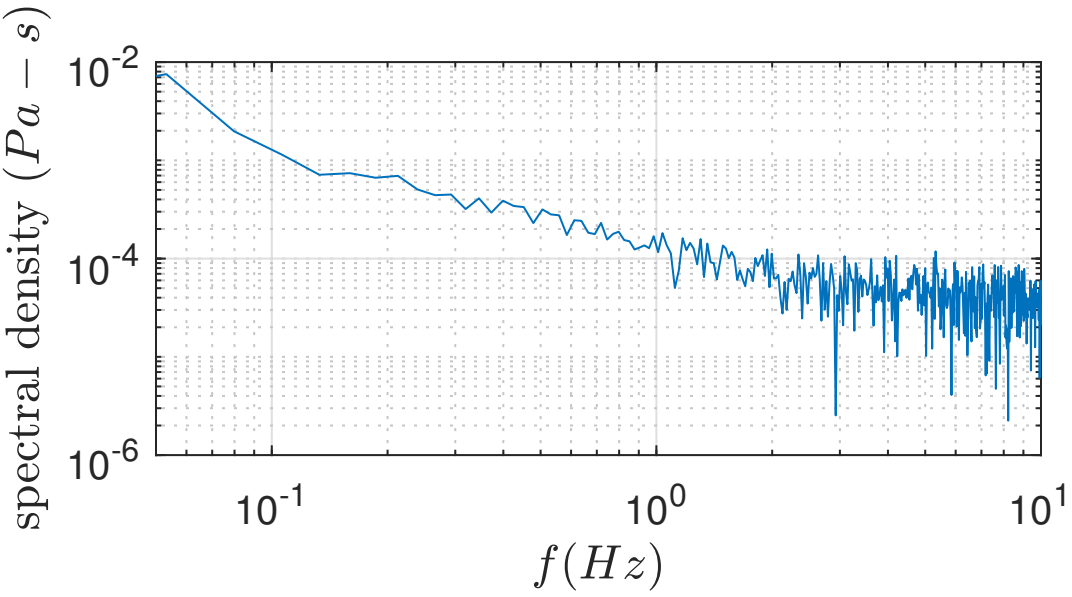

Fig. 5.11: Frequency-domain plot of τ_{avg} at $\dot{\gamma} = 5.6s^{-1}$

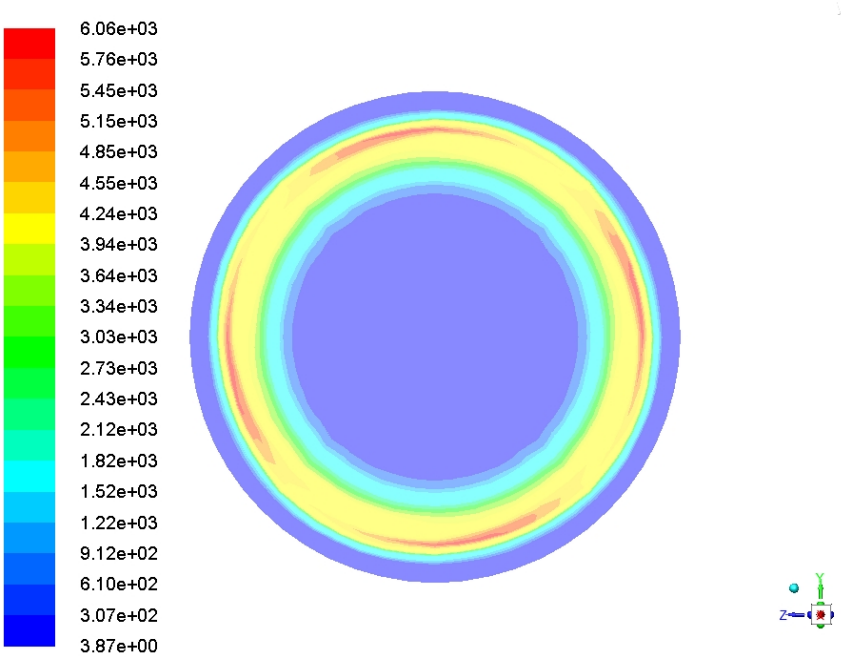

(a) Top view

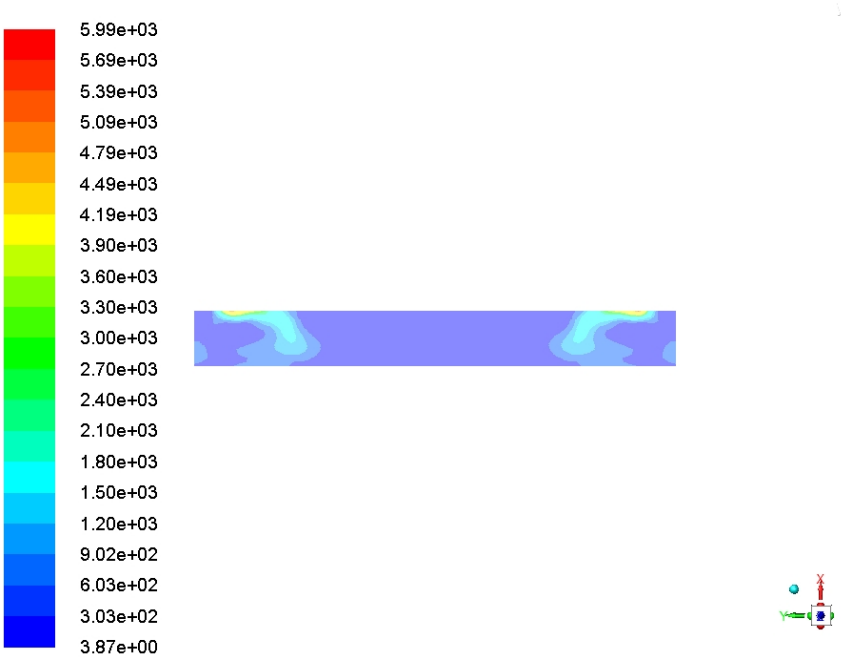

(b) Side view

Fig. 5.12: Contour plot of $tr(\boldsymbol{C})$ at $\dot{\gamma} = 6.7s^{-1}$

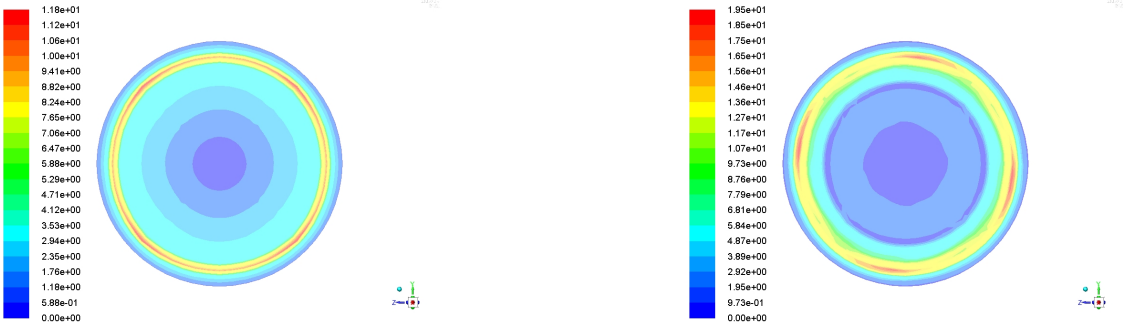

(a) Newtonian (b) Viscoelastic

Fig. 5.13: Contour plot of shear stress at $\dot{\gamma} = 6.7s^{-1}$

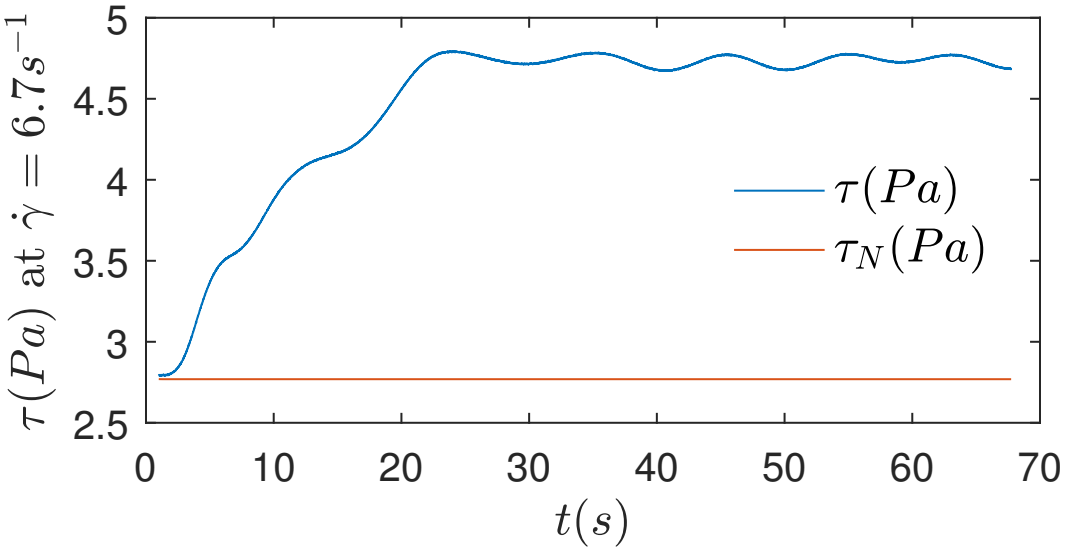

Fig. 5.14: Comparison with the corresponding Newtonian avg stress at $\dot{\gamma} = 6.7s^{-1}$

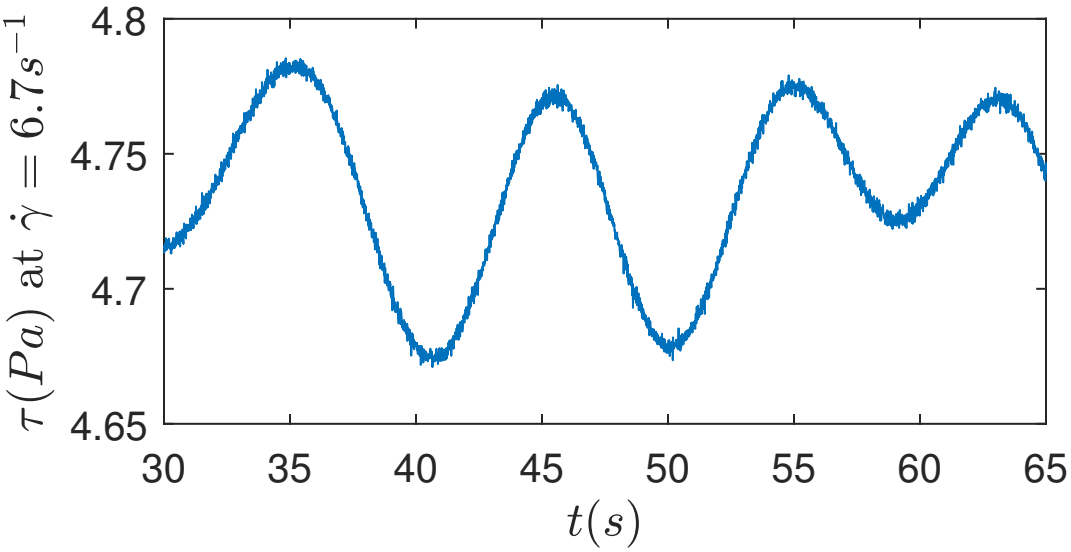

Fig. 5.15: A closer look of τ_{avg} at $\dot{\gamma} = 6.7s^{-1}$

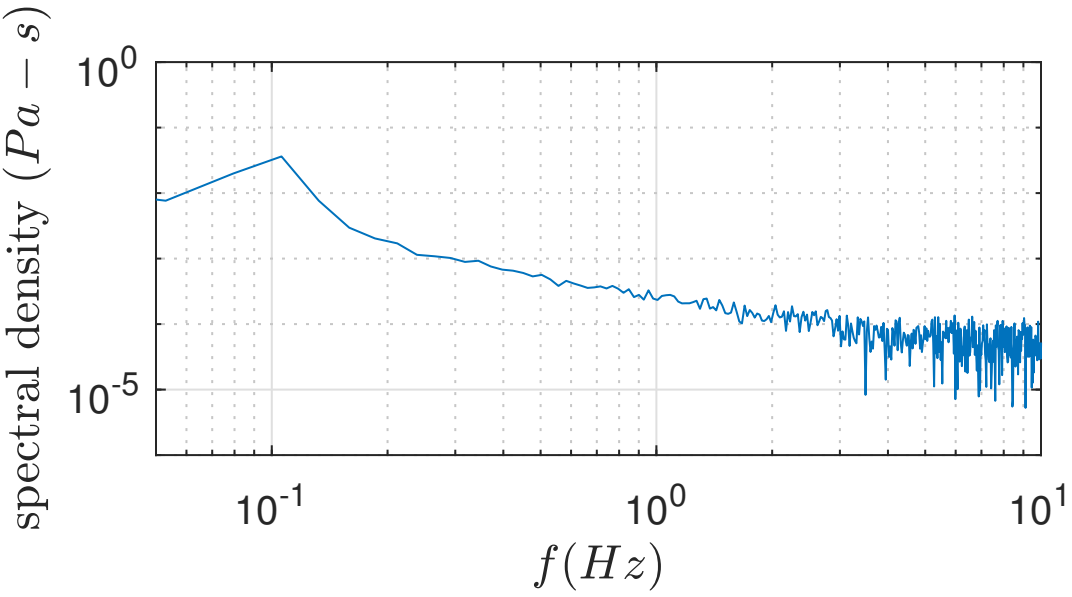

Fig. 5.16: Frequency-domain plot of τ_{avg} at $\dot{\gamma} = 6.7s^{-1}$

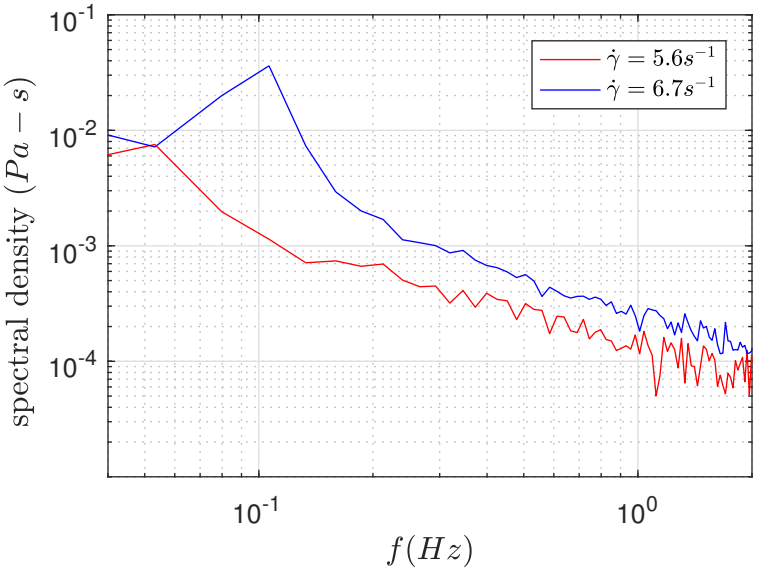

Fig. 5.17: A comparison of the spectral density of τ

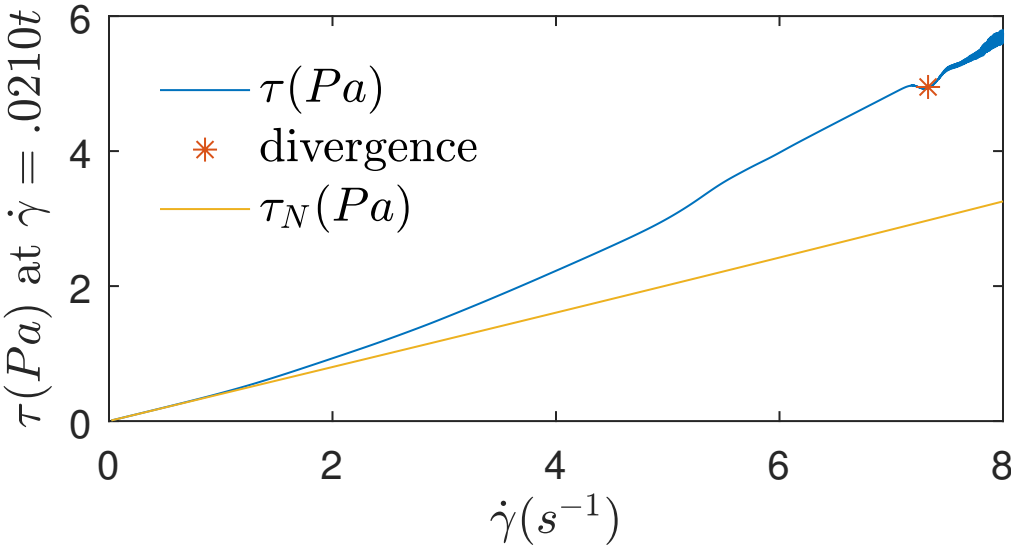

Fig. 5.18: Comparison with corresponding Newtonian avg stress at $\dot{\gamma} = 0.0210t$

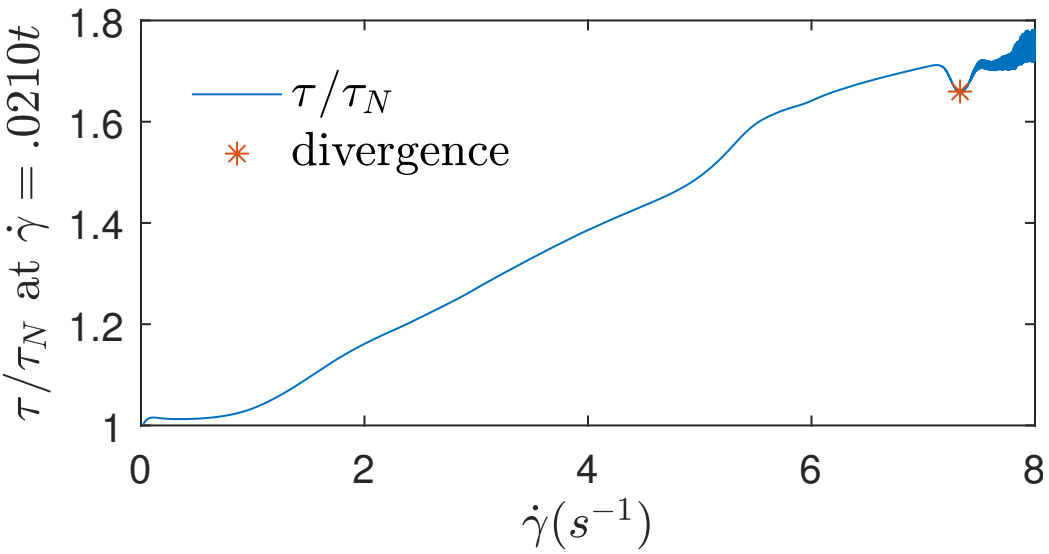

Fig. 5.19: Normalized avg stress at $\dot{\gamma} = 0.0210t$

6. OTHER RELATED WORK*

The focus of this research has been developing a reliable viscoelastic model that can simulate the strange phenomenon called elastic turbulence. The primary strategy has been to use finite volume software called ANSYS-FLUENT and change its constitutive equations to suit our calculations, details of which have been discussed in previous chapters. The biggest asset of this method is the flexibility it provides with respect to the geometries that can be used for simulation. However, this strategy suffers from the following drawbacks:

- The discretization schemes that are based on polynomial approximations can not capture the steep gradients that could arise in the conformation tensor components.
- In general, the hyperbolic nature of the $\boldsymbol{C}$ evolution equation would mandate that no boundary condition be specified at the wall. However, due the presence of diffusion that is inherent to the Finite Volume schemes and also due to added diffusion for stability the accuracy of the solution is compromised.
- It is difficult to handle flows with $Wi > 5$ (which is resolved to some extent with LCR formulation).

6.1 Pseudo-spectral codes

The answer to the difficult problems posed, could lie in employing an alternate strategy, namely the 'pseudo-spectral' method. This method uses Fourier modes in

*Parts of this chapter are reprinted with permission from "Dynamics of a single buoyant plume in a fene-p fluid", Bhaskar Vajipeyajula, Tejasvi Khambampati, and Robert A Handler, 2017, *Physics of Fluids*, 29(9):091701.

x, z direction and Chebychev modes in the vertical y direction. The 'pseudo-spectral' technique addresses the most crucial drawback of diffusion to a large extent. However, this technique can not be used for curvilinear geometries. This is a major hurdle, since all experimental sightings of elastic turbulence were reported only in curvilinear geometries. Instead of curvilinear geometries, one can make the streamlines curvilinear by solving a problem involving a bouyant plume by imposing a Guassian temperature profile at the bottom wall in a channel. Another important merit of this method is that it can be used to capture or resolve much higher gradients in the $\boldsymbol{C}$ components which permits us to work with much higher Wi. This temperature distribution should be expected to cause fluid to rise vertically due to buoyancy forces.

6.2 Boundary condition

The simulated domain lengths are $L_x = \pi h$, $L_y = 2h$, $L_z = \pi h$. The boundary conditions on the bottom wall and the top wall are no slip, no-flux on $\boldsymbol{C}$, $\theta = \theta_{max} e^{-f(x)} e^{-\gamma y}$ and no slip, no-flux on $\boldsymbol{C}$, $\theta = 0$ respectively. Periodic boundary conditions are imposed in the x-direction, z-direction, also gravity g is in the negative y-direction. The model described above gives rise to seven non-dimensional numbers: a Rayleigh number $Ra = (g\alpha\theta_{max}D^3)/(\nu_0\alpha_T)$, a Reynolds number $Re = (UD)/\nu_0$, a Weissenberg number $Wi = (\lambda U)/D$, a Prandtl number $Pr = \nu_0/\alpha_T$, a Schmidt number $Sc = \nu_0/\alpha_p$, the maximum extensional length, L, and β. The time scale $t^* = D/U$. In these definitions the velocity scale is given by $U = \sqrt{g\alpha\theta_{max}D}$ where $D = 2h$. In all simulations to be presented in this chapter, the Weissenberg number was varied from $Wi = 0$ (Newtonian case) to $Wi = 20$, while keeping all other non-dimensional number fixed as follows: $Ra = 2.53 \times 10^6$, $Re = 570$, $Pr = Sc = 7.78$, $L = 100$, and $\beta = 0.9$.

6.3 Results and discussion

In Fig 6.1, vector flow fields superimposed upon the corresponding temperature fields for $Wi = 0$ are shown at a number of time instants in the $x - y$ plane for $z = \pi/2$, which corresponds to the middle of the computational domain. Here and subsequently, time t is made non-dimensional by $t^* = D/u^*$. At time $t = 0$, for which the flow is at rest, the temperature field exhibits a maximum at the bottom boundary at $x = \pi/2$, which shall be referred to as *hotspot*. This temperature distribution should be expected to cause fluid to rise vertically due to buoyancy forces. This is in fact what is observed at $t = 100,\ 200$, and 300, where a *plume* or jet of fluid is seen rising from the center of the domain. Due to the finite size of the domain and the periodic boundary conditions imposed in the x-direction, the flow forms essentially a system of two large counter-rotating vortices as can be seen clearly in the fields in Fig 6.1. It is important to note that this flow is nominally two-dimensional since the temperature field at the bottom wall varies only in the x-direction, resulting in a flow that should depend only on x and y.

This kind of thermal forcing produces a so-called *convergent* flow at the bottom wall ($x = \pi/2$, $y = -h$) in which $\partial v/\partial y > 0$ and a *divergent* flow at the top of the domain ($x = \pi/2$, $y = h$) for which $\partial v/\partial y < 0$. These flows are formed, respectively, as a result of the rising plume at the bottom and the impact of rising fluid upon the top of the domain. It is evident that from the Fig. 6.1 and Fig. 6.2 that the structure of the temperature field is significantly altered at $t = 400$, compared to the thermal field at $t = 20$, by the convergent flow field at bottom wall. This is a direct result of the advection of warmer fluid inward towards the point of maximal convergence at $x = \pi/2$, $y = -h$, leading to a thinning of the thermal layer thickness. The maximum stretching of the polymer molecules is observed at the centre of the

geometry since the *hotspot* induces large velocity gradients close to itself. This can be seen in Fig. 6.3

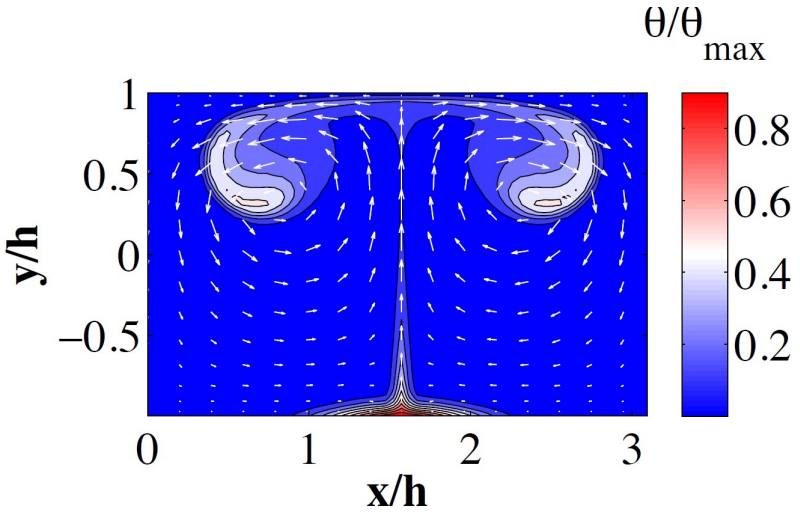

Fig. 6.1: Vector field of velocities, colored by θ/θ_{max} at $t = 20$ for $Wi = 20$

The high Ra number for this flow indicates that the flow is turbulent (inertial). The evolution of the heat flux at the bottom wall of the domain, defined as $q(t) = \overline{q}D/(k\theta_{max})$ where k is the thermal conductivity, $\overline{q} = -k\partial\overline{\theta}/\partial y|_{y=-h}$, $\overline{\theta} = 1/A \int_A \theta dxdz$ is the horizontally averaged temperature, and $A = L_x L_z$. In the transient period $0 \leq t < 10$ the heat flux rises rapidly from its initial value as the thermal boundary layer thins for each Wi. A quasi-steady state is reached in each case, with oscillations evident in the heat flux for $Wi \leq 2$, and an apparent complete elimination of these oscillations for higher Wi. The time averaged heat flux, $q'' = 1/(t_1 - t_0) \int_{t_0}^{t_1} q dt$, shown in Fig 6.4, decreases monotonically for $Wi > 4$, with a maximum reduction of about 28 % percent compared to its Newtonian value. This compares reasonably well with the result of Dubief [15], who found about a 20 % heat transfer reduction for $Wi = 20$ for $L = 100$ (see figure 1 of [15]). It is established

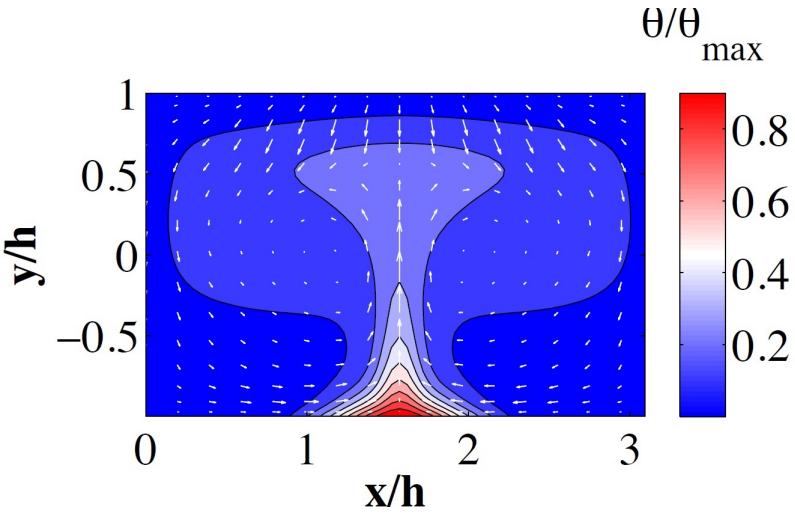

Fig. 6.2: Vector field of velocities, colored by θ/θ_{max} at $t = 400$ for $Wi = 20$

that the presence of polymer additives in turbulent flows tends to reduce the turbulent drag. This reduction of turbulent drag is closely associated with a reduction in mixing that is otherwise enhanced by turbulence [19] [35] [24] [25] [42] [5] [31] [41] [49].

However, in the region corresponding to $2 < Wi < 4$ (Fig 6.4), a dramatic increase in heat flux was observed. This spike in the heat flux calculated was accompanied by strong oscillations through out the flow. These oscillations are suspected to be similar to the elastic waves generated in the swirling flow problem discussed in the previous chapter. The calculated heat flux can be thought of as an index for the amount of mixing in the flow and the sudden surge in its value underlines the emergence of competing elastic stresses. This is an interesting result and could throw some more light on the onset of elastic turbulence. These results are preliminary and need to be investigated with prudence.

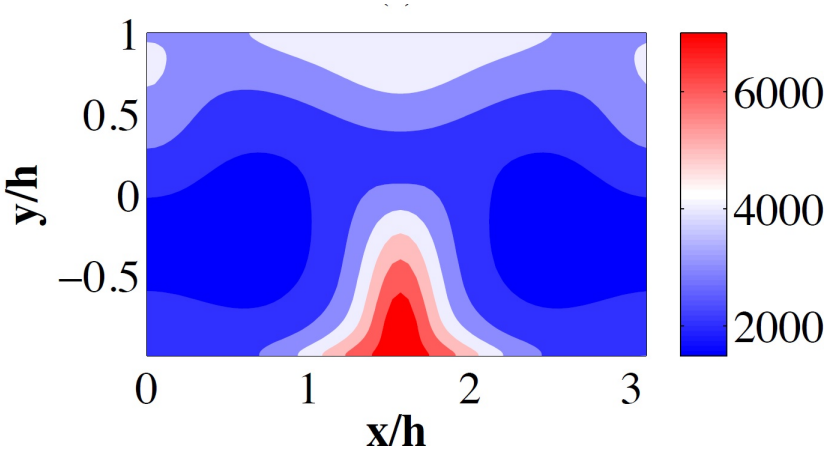

Fig. 6.3: Contours of $tr(\boldsymbol{C})$ at $t = 400$ for $Wi = 20$

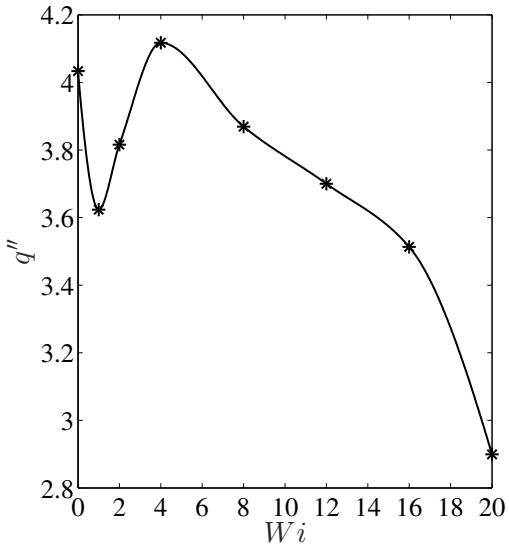

Fig. 6.4: Dimensionless time average heatflux q'' vs Wi

7. CONCLUSION

The primary purpose of this dissertation is to determine whether or not, in three dimensions, elastic turbulence will emerge naturally from the discussed constitutive equations in various geometries. Towards this purpose the following steps have been taken:

The first part of chapter 1 provided a detailed overview of a phenomenon called elastic turbulence and its properties, distinguishing it from the regular inertial turbulence. The non-dimensional number called the Weissenberg number ($Wi = \lambda V/L$) was introduced as a parameter found to have a strong correlation with the emergence of elastic turbulence. An account of the original experiment by Groisman and Steinberg [21], which lead to the discovery of the phenomenon, was provided. Potential advantages and implications in the industry were discussed. The absence of numerical simulations in a 3D domain, replicating the occurrence of elastic turbulence in the real world, is brought to the readers' attention.

Since elastic turbulence is a viscoelastic phenomenon that occurs in the flows of dilute polymer solutions, the second part of chapter 1 focuses on the origin of different types of spring-dashpot viscoelastic models. Here, the FENE-P model was introduced and identified as the model for the numerical simulations of interest for this research. The FENE-P model is based on a positive-definite tensor called the conformation tensor $\boldsymbol{C}$. The definition of $\boldsymbol{C}$ and its physical importance was provided.

In Chapter 2, the details of the derivation of the FENE-P model within the context of a thermodynamic perspective are provided. The derivation is accomplished by maximizing the rate of entropy production for a hyperelastic material. Here an

analogy between the conformation tensor of the FENE-P model and the left Cauchy-Green strain from the evolving natural configuration is established.

Chapter 3 presented the details of the computational technique developed for solving the constitutive equations of the FENE-P model in ANSYS-FLUENT with the aid of user-defined functions. Exact solutions for steady fully developed laminar pipe flow for a FENE-P fluid were derived and compared against the numerical solution for the same and were found to be in good agreement. At higher Wi, the developed technique suffered from the so-called 'high Weissenberg number numerical problem,' causing a numerical breakdown. The divergence is attributed to the inability of the polynomial-based approximations to represent the conformation tensor profiles, which could be exponential in regions of high deformation rate.

In chapter 4, the numerical stabilization scheme called the log-conformation reformulation proposed by Fattal and Kupferman [17] to overcome the challenge posed by the 'high Weissenberg number numerical problem' was discussed in detail. This method involved the transformation of the conformation tensor into the log-domain and solving the equivalent evolution equation in the same. The procedure to employ the log-conformation reformulation technique to model the flow of a FENE-P fluid in ANSYS-FLUENT was detailed. The reformulation was found to solve the 'high Weissenberg number numerical problem' to a large extent, as evidenced by the results provided at the end of the chapter.

Chapter 5 focused on recreating the original swirling flow experiment conducted by Groisman and Steinberg [21] that lead to the discovery of elastic turbulence using the log-conformation technique developed in chapter 4. The two essential features that characterize elastic turbulence, namely an increase in stress and excitation of various time scales were observed and compared to the experimental results. Elastic waves originated throughout the flow domain at sufficiently high shear rates. The

emerged fluctuations span a range of frequencies with one clear dominant frequency.

Chapter 6 explored an alternate strategy, namely the 'pseudo-spectral' method, to model for numerical simulation of viscoelastic fluids. The effects of polymers on heat transfer by investigating the dominant kinematical feature of three-dimensional turbulent Rayleigh-Benard convection, namely, the buoyant plume, were studied using the spectral method.

7.1 Suggestions for future work

In the flow of liquids with polymer additives, one would like to predict all features of elastic turbulence with accuracy. For this purpose, numerical investigation of such processes has the potential to guide the development of augmented thermal transport for a variety of applications at very low Reynolds numbers. Numerical and analytic models of related physical phenomena, especially thermal transport, will then be a natural product of the effort. Such flows, and the devices associated with them, are vital for applications in areas such as pharmaceutics, medicine, heat transfer, biomedical engineering, and electronics cooling.

Using numerical simulation, can elastic turbulence be produced in flows with rectilinear streamlines in realistic geometries? Addressing this question is relevant to the present study because the answers will guide the extent to which elastic turbulence can be used to enhance thermal transport in very simple geometries, which should be relatively inexpensive to manufacture. For example, can such thermal augmentations be achieved with rectilinear streamlines, and if so, what is the maximum size of devices in which this can be achieved? It is only now, with the advent of the log-reformulation method and its successful numerical implementation through finite volume methods, that such questions can be seriously addressed.

This leads to the major goal to be addressed for future work which is to determine:

(a) to what extent elastic turbulence enhances thermal diffusivity and momentum transport, (b) how this enhancement compares to the known enhancement of inertial turbulence, and (c) what kind of influence does the geometry of the flow have? To date, these questions remain unanswered.

REFERENCES

[1] Alexandre Afonso, PJ Oliveira, Fernando Tavares de Pinho, and MA Alves. The log-conformation tensor approach in the finite-volume method framework. *Journal of Non-Newtonian Fluid Mechanics*, 157(1):55–65, 2009.

[2] P Donald Ariel. On the flow of an elastico-viscous fluid near a rotating disk. *Journal of Computational and Applied Mathematics*, 154(1):1–25, 2003.

[3] S Berti and G Boffetta. Elastic waves and transition to elastic turbulence in a two-dimensional viscoelastic kolmogorov flow. *Physical Review E*, 82(3):036314, 2010.

[4] S Berti, A Bistagnino, G Boffetta, A Celani, and S Musacchio. Two-dimensional elastic turbulence. *Physical Review E*, 77(5):055306, 2008.

[5] H. W. Bewersdorff and N. S. Berman. The influence of flow-induced non-newtonian fluid properties on turbulent drag reduction. *Rheol. Acta*, 1988.

[6] RB Bird and HR Warner Jr. Hydrodynamic interaction effects in rigid dumbbell suspensions. i. kinetic theory. *Transactions of the Society of Rheology*, 15(4): 741–750, 1971.

[7] RB Bird, PJ Dotson, and NL Johnson. Polymer solution rheology based on a finitely extensible beadâĂŤspring chain model. *Journal of Non-Newtonian Fluid Mechanics*, 7(2-3):213–235, 1980.

[8] Robert Byron Bird, Robert Calvin Armstrong, and Ole Hassager. Dynamics of polymeric liquids. vol. 1: Fluid mechanics. 1987.

[9] D.V. Boger. A highly elastic constant-viscosity fluid. *Journal of Non-Newtonian Fluid Mechanics*, 3(1):87–91, 1977.

[10] Teodor Burghelea, Enrico Segre, Israel Bar-Joseph, Alex Groisman, and Victor

Steinberg. Chaotic flow and efficient mixing in a microchannel with a polymer solution. *Physical Review E*, 69(6):066305, 2004.

[11] Teodor Burghelea, Enrico Segre, and Victor Steinberg. Role of elastic stress in statistical and scaling properties of elastic turbulence. *Physical Review Letters*, 96(21):214502, 2006.

[12] Teodor Burghelea, Enrico Segre, and Victor Steinberg. Elastic turbulence in von karman swirling flow between two disks. *Physics of Fluids*, 19(5):053104, 2007.

[13] DOA Cruz, Fernando Tavares de Pinho, and PJ Oliveira. Analytical solutions for fully developed laminar flow of some viscoelastic liquids with a newtonian solvent contribution. *Journal of Non-Newtonian Fluid Mechanics*, 132(1):28–35, 2005.

[14] PG De Gennes. Coil-stretch transition of dilute flexible polymers under ultra-high velocity gradients. *The Journal of Chemical Physics*, 60(12):5030–5042, 1974.

[15] Yves Dubief. Heat transfer enhancement and reduction by poylmer additives in turbulent rayleigh benard convection. *arXiv preprint arXiv:1009.0493*, 2010.

[16] Carl Eckart. The thermodynamics of irreversible processes. iv. the theory of elasticity and anelasticity. *Physical Review*, 73(4):373, 1948.

[17] Raanan Fattal and Raz Kupferman. Constitutive laws for the matrix-logarithm of the conformation tensor. *Journal of Non-Newtonian Fluid Mechanics*, 123 (2):281–285, 2004.

[18] Raanan Fattal and Raz Kupferman. Time-dependent simulation of viscoelastic flows at high weissenberg number using the log-conformation representation. *Journal of Non-Newtonian Fluid Mechanics*, 126(1):23–37, 2005.

[19] G. Fortuna and T. J. Hanratty. The influence of drag-reducing polymers on

turbulence in the viscous sublayer. *J. Fluid Mech*, 1972.

[20] AN Gent. A new constitutive relation for rubber. *Rubber Chemistry and Technology*, 69(1):59–61, 1996.

[21] Alexander Groisman and Victor Steinberg. Elastic turbulence in a polymer solution flow. *Nature*, 405(6782):53–55, 2000.

[22] Alexander Groisman and Victor Steinberg. Efficient mixing at low reynolds numbers using polymer additives. *Nature*, 410(6831):905–908, 2001.

[23] Alexander Groisman and Victor Steinberg. Elastic turbulence in curvilinear flows of polymer solutions. *New Journal of Physics*, 6(1):29, 2004.

[24] M. Kodama H. Usui and Y. Sano. Laser-doppler measurements of turbulence structure in a drag-reducing pipe flow with polymer injection. *J. Chem. Eng. Jpn*, 1989.

[25] M. Kodama H. Usui and Y. Sano. Laser-doppler measurements of turbulence structure in a drag-reducing pipe flow with polymer injection. *J. Chem. Eng. Jpn*, 1989.

[26] Florian Habla, Ming Wei Tan, Johannes Haßlberger, and Olaf Hinrichsen. Numerical simulation of the viscoelastic flow in a three-dimensional lid-driven cavity using the log-conformation reformulation in openfoam®. *Journal of Non-Newtonian Fluid Mechanics*, 212:47–62, 2014.

[27] Cornelius O Horgan and Giuseppe Saccomandi. Constitutive models for compressible nonlinearly elastic materials with limiting chain extensibility. *Journal of Elasticity*, 77(2):123–138, 2004.

[28] Yonggun Jun and Victor Steinberg. Elastic turbulence in a curvilinear channel flow. *Physical Review E*, 84(5):056325, 2011.

[29] Th V Karman. Über laminare und turbulente reibung. *ZAMM-Journal of Applied Mathematics and Mechanics/Zeitschrift für Angewandte Mathematik und*

Mechanik, 1(4):233–252, 1921.

[30] Ronald G Larson. Instabilities in viscoelastic flows. *Rheologica Acta*, 31(3): 213–263, 1992.

[31] T. S. Luchik and W. G. Tiederman. Turbulent structure in low concentration drag-reducing channel flows. *J. Fluid Mech*, 1988.

[32] John L Lumley. Drag reduction by additives. *Annual Review of Fluid Mechanics*, 1(1):367–384, 1969.

[33] Josef Málek, Kumbakonam R Rajagopal, and K Tuma. On a variant of the maxwell and oldroyd-b models within the context of a thermodynamic basis. *International Journal of Non-Linear Mechanics*, 76:42–47, 2015.

[34] James Clerk Maxwell. Iv. on the dynamical theory of gases. *Philosophical Transactions of the Royal Society of London*, (157):49–88, 1867.

[35] W. D. McComb and L. H. Rabie. Laser-doppler measurements of turbulent structure. *AIChE J*, 1982.

[36] P Mitschka. Nicht-newtonsche flüssigkeiten ii. drehströmungen ostwald-de waelescher nicht-newtonscher flüssigkeiten. *Collection of Czechoslovak Chemical Communications*, 29(12):2892–2905, 1964.

[37] JG Oldroyd. On the formulation of rheological equations of state. *Proceedings of the Royal Society of London. Series A. Mathematical and Physical Sciences*, 200(1063):523–541, 1950.

[38] KR Rajagopal. Multiple configurations in continuum mechanics. report. *Institute for Computational and Applied Mechanics, University of Pittsburgh*, 1995.

[39] KR Rajagopal and AR Srinivasa. A gibbs-potential-based formulation for obtaining the response functions for a class of viscoelastic materials. *Proceedings of the Royal Society A: Mathematical, Physical and Engineering Sciences*, 467 (2125):39–58, 2010.

[40] Kumbakonam R Rajagopal and Arun R Srinivasa. A thermodynamic frame work for rate type fluid models. *Journal of Non-Newtonian Fluid Mechanics*, 88(3):207–227, 2000.

[41] M. J. Rudd. Velocity measurements made with a laser dopplermeter on the turbulent pipe flow of a dilute polymer solution. *J. Fluid Mech*, 1972.

[42] F. A. Seyer and A. B. Metzner. Turbulence phenomena in drag-reducing systems. *AIChE J*, 1969.

[43] Eric SG Shaqfeh. Purely elastic instabilities in viscometric flows. *Annual Review of Fluid Mechanics*, 28(1):129–185, 1996.

[44] Jason R Stokes, Lachlan J.W. Graham, and D.V. Boger. Vortex breakdown in confined swirling flow of a dilute flexible polymer solution. *Xiith International Congress On Rheology, Proceedings*, pages 359–360, 1996.

[45] Hendrik Tennekes and John Leask Lumley. *A first course in turbulence*. MIT Press, 1972.

[46] Clifford Truesdell and Walter Noll. The non-linear field theories of mechanics. In *The non-linear field theories of mechanics*, pages 1–579. Springer, 2004.

[47] T Vaithianathan and Lance R Collins. Numerical approach to simulating turbulent flow of a viscoelastic polymer solution. *Journal of Computational Physics*, 187(1):1–21, 2003.

[48] Bhaskar Vajipeyajula, Tejsavi Khambampati, and Robert A Handler. Dynamics of a single buoyant plume in a fene-p fluid. *Physics of Fluids*, 29(9):091701, 2017.

[49] PS Virk. An elastic sublayer model for drag reduction by dilute solutions of linear macromolecules. *Journal of Fluid Mechanics*, 45(3):417–440, 1971.

[50] Harold R Warner Jr. Kinetic theory and rheology of dilute suspensions of finitely extendible dumbbells. *Industrial & Engineering Chemistry Fundamentals*, 11(3): 379–387, 1972.